

JOURNAL OF MECHANICAL ENGINEERING

An International Journal

Vol 17 (2)	15 July 2020	ISSN 1823-5514	eISSN 2550-164X
------------	--------------	----------------	-----------------

1	Performance of Hollow Reinforced Concrete Beam in Structural Member <i>Hamidun Mohd Noh[*], Nor Lailatul Izzatil Azwani Mohamad, Rolly Bangau, Nur'Ain Idris</i>	1
2	On the Modelling Aspect of Low-Velocity Impact Composite Laminates <i>M.S. Meon[*], N.H. Mohamad Nor, S. Shawal, J.B. Saedon, M.N. Rao, K.-U. Schröder</i>	13
3	Optimization of Tool Life and Surface Roughness for Hypereutectic Al – Si Alloys in Face Milling <i>Kamal Othman[*], Jaharah Abdul Ghani, Afifah Juri, Mohd Shahfizal Ruslan Mohd, Shahir Kassim, Che Hassan Che Haron</i>	27
4	3D Model of Bone Scaffolds Based on the Mechanical Behaviour for a Hybrid Nano Bio-composites <i>Jenan, S. Kashaan, Saad M. Ali[*]</i>	45
5	Influence of Process Parameters in Wire and Arc Additive Manufacturing (WAAM) Process <i>Nor Ana Rosli, Mohd Rizal Alkahari[*], Faiz Redza Ramli, Mohd Nizam Sudin, Shajahan Maidin</i>	69
6	Vibration Suppression Control of Three Inertial Systems <i>Duong Minh Duc[*], Nguyen Manh Linh, Dao Quy Thinh, Do Trong Hieu</i>	79
7	Heat Transfer of Swirling Multi Jets Impinging System <i>Amar Zerrou[*], Ali Khelil, Larbi Loukarfi</i>	93
8	Study on Drag Coefficient (C_D) Value of Low-Energy Prototype Class Car <i>J. Jodiputra, S. Tobing[*], H. Gunawan, M.G. Andika</i>	109
9	Study on the development of a quaternary layer of B₄C-TiB₂-Al₃Ti-Al in AA7050 / B₄C Ex-Situ composite and influence of heat treatment on mechanical and wear properties <i>Arvind Kumar[*], Ram Naresh Rai</i>	129
10	Design of the MCCIS on the Gas-Fueled Motorcycle to Overcome Detonation in Engine Idling	141

*Didik Nurhadiyanto**, *Mujiyono*, *Angger Gufita*, *Riyadi Prabowo Moecty*,
Fatchurrohman Baihaqi, *Sena Budi Pramana*

- 11 [Effect of Carbon Nanotube-Silane Addition on Mechanical Properties of Chloroprene Rubber-filled Carbon Black](#)
*Kok-Tee Lau**, *Jeefferie Abd Razak*, *Hairul Effendy Ab Maulod*, *Noraiham Muhamad*, *Mohamad Hanif Hashim*, *Nurzallia Mohd Saad*

157

Performance of Hollow Reinforced Concrete Beam in Structural Member

Hamidun Mohd Noh*, Nor Lailatul Izzatil Azwani Mohamad, Rolly Bangau
Department of Construction Management, Faculty of Technology
Management and Business, Universiti Tun Hussein Onn Malaysia,
Johor, Malaysia
*hamidun@uthm.edu.my

Nur'Ain Idris
Department of Civil Engineering, Centre for Diploma Studies (CeDS),
Universiti Tun Hussein Onn Malaysia, Kampus Pagoh,
Johor, Malaysia

ABSTRACT

Recently, the problem faced by the construction industry is a significant shortage of raw materials of concrete. Thus, the main idea of this research is to replace the use of concrete at the middle area of neutral axis of beam with voided system by incorporating PVC pipe. This research aims to reduce the concrete usage; structure's self-weight without neglecting its strength performance. The experimental work consists of casting and testing the 1200 x 160 x 160 mm beams with (Ø40 mm, Ø50 mm, and Ø100 mm) and without void at the neutral axis. The test results indicated that the strength performance of all RC beams with voided section is stronger than the ordinary RC beam where the V50 RC beam is able to withstand loads up to 38.25 kN and has a strength increment of 49.2% compared to the ordinary RC beam. By this material optimization, the reduction of concrete usage and self-weight of the V100 RC beam recorded a reduction of up to 35.14% but in terms of its strength is relatively low compared to the V40 RC beam and V50 RC beam. This findings show a positive result in reducing the dead load without affecting the strength of the structure. Besides aiming to the reduction of concrete usage and structure's self-weight, the idea of this research could be used and implemented in producing a lightweight structure with easy handling and installing, and at the same time focusing to meet the IBS system.

Keywords: concrete, flexural strength, lightweight structure, neutral axis, voided RC beam.

Introduction

The construction industry is one of the industries that contribute to the development of a country. However, the rapid construction development has increased the demand of concrete as the most common construction materials in building constructions. Thus, the reduction of these natural resources availability resulting in increasing the concrete price. Cement is the raw material that shows the most significant increase of prices when it showed an increase of 9.75% in 2011, 3.13% in early 2012 and 5.58% in the third quarter of 2012 [1].

Moreover, the concrete industry is one of the primary producers of carbon dioxide (CO₂), creating up to 5% of worldwide man-made emissions of this gas, of which 50% and 40% is from the chemical process and burning fuel respectively. Hence it should be used as efficiently as possible. If not, the concrete production will affect to the environment condition and can cause global warming by trapping the sun's radiant energy in atmosphere [2].

In Malaysia, the use of lightweight concrete is not very common; this may due to large amount of raw materials still available in the market but in future, the availability of raw materials cannot be guaranteed. In fact, sustainability is essential concern to satisfy the demands of the present generation without compromising the ability the future generations to meet their needs [3]. For example, if the world runs out of limestone, as it is predicted to happen in some places, then the Portland cement cannot be produce, therefore, concrete also cannot be produce. Designing for sustainability which takes into account the design for short-term and long-term consequences of the society impact, so, new generation of admixture or additives are needed to improve the durability of concrete structure.

On the other hand, RC beams is a load-bearing unit that can be used to carry both horizontal and vertical loads which undergoes a variable horizontal loading over time according to the use of the building. Thus, inaccurate in limit state design which the load applied exceeds its ultimate, serviceability and other limit states will encounter damage to the structure of the beam. If an element is exposed to this condition for a long period of time, the creep and fatigue in RC beam will occurs. In most cases for high-rise buildings, the beam structure is affected due to the higher unit weight of concrete. For examples, the New World Hotel, Singapore and Highland Tower, Malaysia are the buildings that have failed during their lifetimes.

In recent years, the ideas to make concrete lighter is by changing the proportion of the concrete mix in order to improvise the concrete structural performance such as by using natural fibre, waste materials and construction waste. Also, lightweight concrete can be prepared either by omitting the finer

sizes of the aggregate or even replacing them by hollow, cellular or voided materials [4]. So, it will reduce the usage of natural-sourced material in concrete and reduce the weight of the structural member by replacing the material in the mixture.

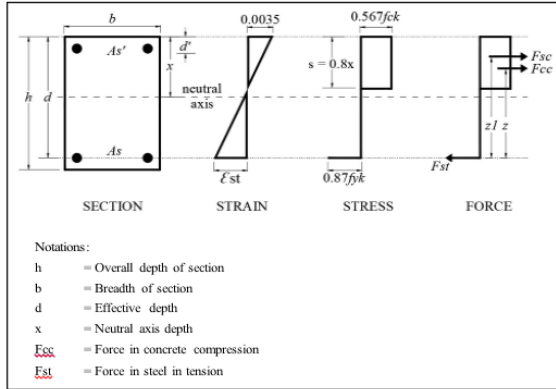


Figure 1: Doubly reinforced section with rectangular stress block [6].

On top of that, various theories have been developed to reduce the self-weight of the structural elements for a given load-carrying capacity. In facts, the dead load can be reduce by the structural material optimization which contribute to the seismic affect in high-rise structures and very good at the vibration dampers, as well as good in heat insulation [5]. As shown in Figure 1, the rectangular stress block illustrates the stress-strain distribution in the section [6]. In RC beam, the stresses on the beams are maximum at the top and bottom area while minimum stresses at the neutral axis. So, the stress acting on the concrete near the neutral axis is not much contribute to the structure. Efficient use of concrete materials can be done by replacing the concrete in and near the neutral axis [7]. An alternate method of replacing the neutral axis zone with inert weightless substances will not greatly affect the strength and stress characteristics of the beam and also it will not affect the geometry and shape [8]. Hence, this research will focus on the technique of creating air voids inside the structural member for reducing its concrete amount by using of PVC pipe as continuous horizontal voided at neutral axis.

In this study, PVC pipe was placed at the middle of structure which classified as ineffective region. By this method, the reduction weight of the beam and efficient use the concrete materials can be done by placing a PVC pipe instead, hence making the beam hollow at the neutral axis to form the voided RC beam system. This is an alternative to reduce the use of concrete and the flexural behaviour of RC beam with hollow core is similar to that of

the conventional RC beam [9]. The beam structure was choosing due to the testing apparatus availability of the study. Therefore, flexural test is generally used to determine the flexural strength of material as it facilitates the preparation and testing of specimens and it is also described as actual practice at construction sites where load is imposed on the structure itself.

Data and Methods

In this part, the preparation of experimental program, test setup and instrumentations is carried out. The preparation of these experiments includes beam specimens with various diameters of voided and without voided with beam dimension of 1200 mm x 160 mm x 160 mm as shown in Figure 2. All reinforced concrete beams designed as under reinforced section according to BS EN 1992-1-1:2004.

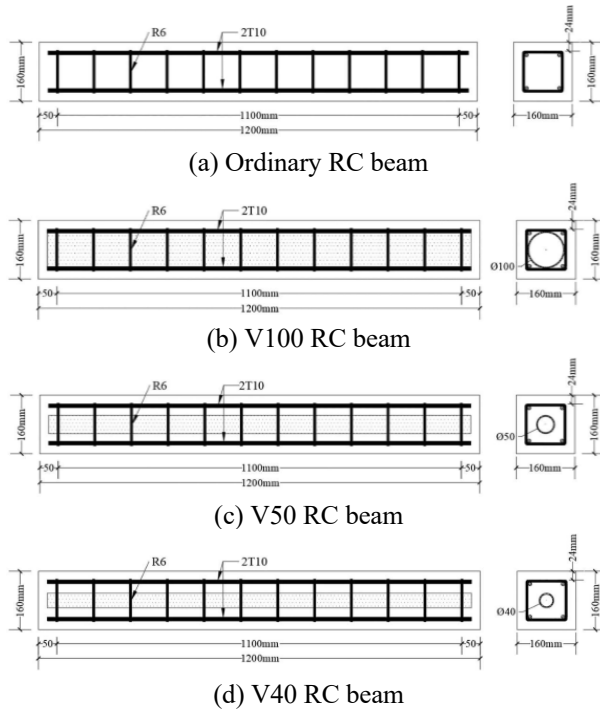


Figure 2: The illustration of RC beam specimens.

The flexural test was carried out in accordance with BS EN 12390-5:2009, testing concrete of method for determination of flexural strength. A flexural testing machine that provides two steel rollers with 38 mm diameter on which the beam specimen will be supported while length from the ends beam to the first steel roller is 100 mm. The load then divided equally between two loading rollers and it is mounted properly where the load applied axially (Figure 3).

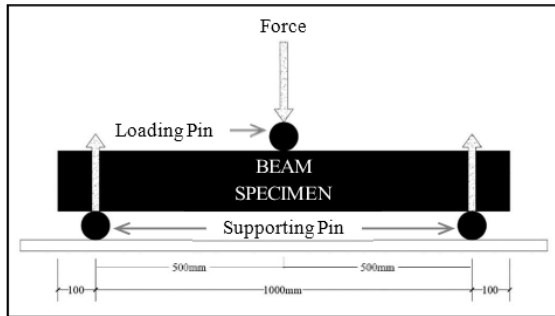


Figure 3: Schematic 3-point loading flexural test setup.

Results

Comparison of Flexural Test for Ordinary RC Beam and Voided RC Beam with Various Diameters

After few tests conducted on the beam specimens, Figure 4 shows the flexural strength of reinforced concrete (RC) beam with voided $\text{\O}100$ mm, $\text{\O}50$ mm and $\text{\O}40$ mm, respectively. The load-displacement distributions were plotted for the initial and final strength.

The results compared the load-displacement relationship of RC beams with embedded PVC pipes and the ordinary RC beam at different load stages. It is clearly shown that voided RC beam that embedded PVC pipes have a better performance and able to withstand the load up to 34.25 kN, 38.25 kN and 32.50 kN for V40 RC beam, V50 RC beam and V100 RC beam respectively. Meanwhile, the ordinary RC beam just withstand the maximum load is 15.35 kN only (Table 1).

Replacing the concrete by PVC pipe at neutral axis exhibits significant changes in the load carrying capacity of the RC beam in term of strength. Varghese and Joy [9] also found that presence of void PVC pipe instead of concrete in the center region of the RC beam caused an increase 21% in strength of voided RC beam due to at the neutral axis is not fully utilized.

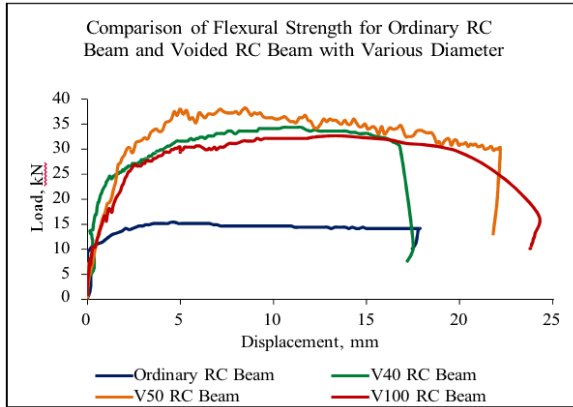


Figure 4: Comparison of flexural strength between ordinary RC beam and voided RC beam with various diameters

Table 1: Summary of load-displacement for RC beam

Type of RC Beam	Ordinary	V100	V50	V40
Maximum Load (kN)	15.35	32.50	38.25	34.25
Displacement (mm)	17.47	23.76	21.79	17.21

Based on the observation, the reason for all voided RC beams able to achieve more strength and durable than the ordinary RC beam, it is most probably due to the positive side shows that the concrete prepared with inserted by PVC pipe at the centre of RC beam was lighter (lower density), more ductile (and reduced modulus of elasticity), had lower drying shrinkage and higher resistance to chloride ion penetration. Although, greater the diameter void of PVC pipe, greater the reading of displacement. As according to Gasham [10] which concluded that when the diameter of PVC pipe exceeded two-third of the RC beam width, the influence of PVC pipe on the recorded displacement was relatively large especially for PVC pipe installed at the centre of RC beam. The result can be improved by taken into account the ratio of cover and bar diameter as suggested by Hamidun and Yoshimi [11].

In facts, small tubular void of PVC pipe can make RC beam more strength but more deformable than counter RC beam has big size tubular void of PVC pipe. While, similarity in structural behaviour between voided RC beam and ordinary RC beam tested specimens is clear even when the values are different. So, the present experimental results are compatible with the previous cited works.

Influence of Void Area to the Concrete Strength

A graph of maximum load for each reinforced concrete (RC) beam specimen with different void sizes were plotted as shown in Figure 5. It is clearly seen that the maximum load increased rapidly from 15.35 kN (ordinary beam) to 38.25 kN for the V50 and then dropped to 32.50 kN for the V100.

This result shows that the concrete strength of the RC beam specimens are affected by changes of different diameter sizes of PVC pipe. Since, the V50 RC beam has about 11% and 15% strength higher than V40 RC beam and V100 RC beam respectively, the effect of longitudinal void with medium size is better than the distributed to small or big size voids. It is because of the optimal void diameter was derived. To derive the optimal void diameter, three aspects of criteria which were safety, strength and deflection were considered [12].

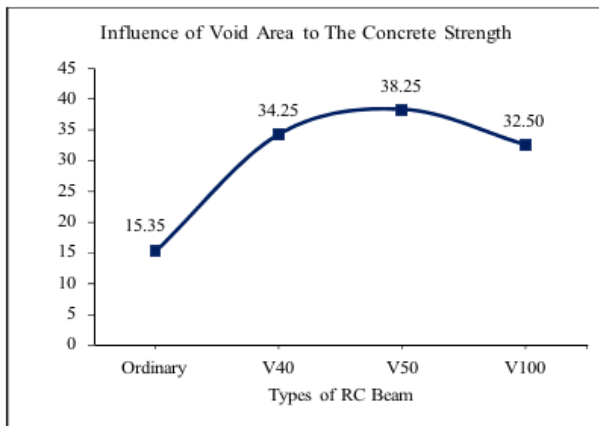


Figure 5: Influence of void area to the concrete strength.

Reduction of Concrete Usage in Reinforced Concrete Beam

Table 2 shows the results obtained from the calculation concrete saving between ordinary RC beam and voided RC beam with various diameter of PVC pipes. For comparison of all types of RC beams, the biggest reduction is from V100 with reduction of 35.14% than ordinary RC beam from the volume of concrete.

Varghese and Joy [13] stated a main component in the total cost of the product varying from 25 to 70% for the construction material cost. Thus, in order to control the cost, it is necessary to pay more attention for controlling material cost especially through abnormal losses. It should be made sure that the right quantities of materials are consumed with less wastage. These issues can be minimized by avoiding concrete in the neutral axis without bearing significant strength.

Table 2: Reduction of concrete usage in RC beam

Total of RC beam	Total concrete remaining (m ³)	Reduction of concrete usage (%)
Ordinary RC Beam	0	0
Voided RC Beam (V40)	0.028703	6.6
Voided RC Beam (V50)	0.027759	9.6
Voided RC Beam (V100)	0.019926	35.1

Reduction of Self-weight in Reinforced Concrete Beam

The self-weight comparison of ordinary RC beam and voided RC beam is given in Table 3. When comparing all self-weight of voided RC beam, the biggest reduction is from V100 specimen with 33.55% self-weight reduction than the ordinary RC beam. Meanwhile, there is 10.5% and 6.2% reduction from V50 and V40 specimen, respectively.

From these results, it is clear that when assumed the smaller the diameter of the PVC pipe is used, the self-weight reduction is also small and vice versa. Joy and Rajeev stated the volume of concrete is reduced then the self-weight of the beam can be reduced also. This can be done by avoiding concrete being placed at the neutral axis.

Table 3: Self-Weight Reduction in RC Beam

Total of RC beam	Difference in weight of concrete (m ³)	Weight of concrete reduction (%)
Ordinary RC Beam	0	0
Voided RC Beam (V40)	4.70	6.2
Voided RC Beam (V50)	7.95	10.5
Voided RC Beam (V100)	25.35	33.6

Comparison of all Factors: Total Reduction for Concrete Usage, Self-weight and Strength Increment in RC Beam

Based on the Figure 6, there are percentage of concrete usage, self-weight reduction and strength increment for four (4) reinforced concrete (RC) beam. The results show that the wider width of void diameter in the RC beam, the greater reduction of concrete volume and self-weight and vice versa. While, strength increment for all voided RC beam compared to ordinary RC beam is higher percentage of strength.

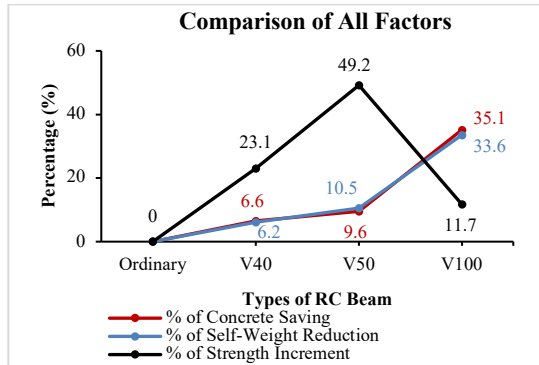


Figure 6: Total reduction of concrete usage, self-weight in RC beam and strength increment to RC beam.

In fact, when compared to all factors such as concrete reduction, self-weight and strength, V50 RC beam is the best. The V50 RC beam has a strength increment of 49.2% as well as the reduction of concrete usage and its self-weight of 9.6% and 10.5% respectively. Although, the V100 RC beam has the highest reduction in concrete usage and self-weight but in terms of its strength is relatively low compared to the V40 RC beam and V50 RC beam. Moreover, the performance of this voided structure could be predicted by using the method proposed by Hamidun et al. [13] in predicting the structural strength and service life of structure by taken into account the chemical and mechanical damage.

Conclusion

In this research, the flexural strength behavior of the ordinary and voided RC beam with various diameters of PVC pipes was studied. It is clearly shown that voided RC beam that embedded PVC pipes have a better performance and able to withstand the load up to 34.25 kN, 38.25 kN and 32.50 kN for V40 RC beam, V50 RC beam and V100 RC beam respectively. Meanwhile, the ordinary RC beam just withstand the maximum load is 15.35 kN only. By replacing the concrete by PVC pipe at neutral axis, it exhibits significant changes in the load carrying capacity of the RC beam, in term of strength.

From the other side, the voided RC beam contributed to the reduction of concrete usage and the total self-weight. From all the specimen, voided RC beam V50 shows an optimum performance with a highest strength increment up to 49.2% with 10.5% self-weight reduction which save 9.6% of concrete usage.

Acknowledgement

Appreciation to MOHE and ORICC, Universiti Tun Hussein Onn Malaysia for supporting this research (vot: K033). Appreciation is also to Construction Management and Innovation (CMI) focus group, Faculty of Technology Management and Business.

References

- [1] Construction Industry Development Board (CIDB) (2013). Harga Bahan Binaan Utama. Retrieved on April 11, 2014 from: <http://www.cidb.gov.my/images/pdf/statistic/bab3%20%20bahan%20binaa%20utama.pdf>
- [2] Imbabi, M. S., Carrigan, C., and McKenna, S., "Trends and Developments in Green Cement and Concrete Technology," *International Journal of Sustainable Built Environment* 1, 194-216 (2012).
- [3] Mokhatar, S. N., Mustafa, M. M., Rouwab, S. S., and Hadipramana, J., "Performance of Reinforced Concrete Beams with Differently Positioned Replacement Zones of Block Infill under Low Impact Loads," *International Symposium on Civil and Environmental Engineering* 103, 1-8 (2017).
- [4] Gaur, A. S., Kumar, V., and Singh, R. P., "Lightweight Concrete," *Engineering and Technology Journal* 2(9), 242-246 (2017).
- [5] Manikandan, S., Dharmar, S., and Robertravi, S., "Experimental Study on Flexural Behavior of Reinforced Concrete Hollow Core Sandwich Beams," *International Journal of Advance Research in Science and Engineering* 4(01), 937-946 (2015).
- [6] Yassin, M. S., & Abdullah, R., *Reinforced Concrete Design: To Eurocode 2. Preliminary Edition February, 2012*. Johor: Universiti Teknologi Malaysia (UTM) Press (2012).
- [7] Dhinesh, N. P., and Satheesh, V. S., "Flexural Behavior of Hollow Square Beam," *International Journal of Scientific Engineering and Applied Science* 3(3), 236- 242 (2017).
- [8] Kumar, A. S., and Joy, A., *Experimental Investigation on Partial Replacement of Concrete Below Neutral Axis of Beam*, *International Journal of Science and Research* 4(8), 1670- 1674 (2013).
- [9] Varghese, N. & Joy, A., "Flexural Behavior of Reinforced Concrete Beam with Hollow Core at Various Depth," *International Journal of Science and Research* 5(5), 741- 746 (2016).
- [10] Al-Gasham, T. S. S., "Reinforced Concrete Moderate Deep Beams with Embedded PVC Pipes," *Wasit Journal of Engineering Science* 3(1), 19-

- 29 (2015).
- [11] Hamidun Mohd Noh and Yoshimi Sonoda, "Impact of Cover/Bar Diameter Ratio To The Structural Performance of Reinforced Concrete Member Due To Corrosion," *Malaysia Construction Research Journal* 5(3), 145-152 (2018).
- [12] Park, J. H., Chung, J. H., Choi, H. K., Lee, S. C. and Choi, C. S., "An Analytical Study on the Impact of Hollow Shapes in Bi-Axial Hollow Slabs," *Proceedings of Fracture Mechanics of Concrete and Concrete Structures*, 1729- 1736 (2010).
- [13] Hamidun Mohd Noh, Yoshimi Sonoda, Hiroki Tamai, Isao Kuwahara, "An analysis of Chemical-Mechanizal Damage in Reinforced Concrete Beam," *International Journal of Integrated Engineering* 10(4), 156-164 (2018).

On the Modelling Aspect of Low-Velocity Impact Composite Laminates

M.S. Meon*, N.H. Mohamad Nor, S. Shawal, J.B. Saedon
Faculty of Mechanical Engineering, Universiti Teknologi MARA (UiTM),
40450 Shah Alam, Selangor, Malaysia
*msuhairil@uitm.edu.my

M.N. Rao, K.-U. Schröder
Institute for Structural Mechanics and Lightweight Design, RWTH Aachen
University, Germany

ABSTRACT

Composites suffer a degradation of structural stiffness due to various types of impact loading resulting in damage which is difficult to observe from the surface of the structure. The paper deals with the finite element model (FEM) to study the possible modelling procedures in low-velocity impact (LVI) and failure mechanism of carbon fiber reinforced polymer (CFRP) composite laminate of CCF300/epoxy and its structural responses. In finite element calculation, a proposed three-dimensional progressive damage model is used to determine the intralaminar damage, whereas the cohesive contact formulation is employed to analyse the interlaminar damage. The failure model performances are validated and verified based on different boundary conditions while maintaining the impact energy. Through simulation, the variation in boundary conditions significantly changes the structural responses and energy absorption of the laminates. It is hoped this study will be a great tool in determining the different composite impact scenarios.

Keywords: *Low-velocity impact (LVI); carbon fiber reinforced polymer (CFRP); finite element model (FEM); intralaminar damage; interlaminar damage*

Introduction

In many engineering applications such as aerospace, marine, defence and automotive, composite structures are highly utilized for many purposes due to its superior quality of lightweight and high strength to weight ratio. Besides having such great advantages, a major drawback that degrades the supremacy of this material is low resistance toward impact loading. A low-velocity impact (LVI) is one of the loading scenarios which can cause a significant reduction in stiffness and strength of the composite structures [1]. The detection of this type of failure is quite intricate because the damage cannot be easily observed from the surface of components by the naked eyes, thus exposing the structures into great danger. For this reason, a high number of researchers focusing on low-velocity impact, and investigated in form of experiment [2,3], simulations [4–6] and a combination of both approaches [7–10].

During the LVI process in composite laminates, most experimental works referred to ASTM D7136 standard [11] for dimensioning and other related information. In most literature, the standard size of the laminates used was 150 mm x 100 mm with a cut-out rectangular support base of 125 mm x 75 mm. However, there also several kinds of literature adopted different geometry of the laminates as well as non-standard support fixture. Liu and Liao [8] used a 100 mm x 100 mm composite plate together with top and bottom cut-out support fixtures. They tested plastic fiber-reinforced polymer matrix laminate.

For the sake of cost-saving, researchers decided to shift to virtual testing using finite element method (FEM). To minimize the computational time, boundary conditions (i.e. clamping zone) and lay-up arrangement, especially at the interface between layers were crucially emphasized in the FE model. Full-scale geometry, including gripping areas, was modelled explicitly as described in the paper [9], [2], and [12]. All paper used cohesive elements to capture the onset and propagation of delamination. Other researchers such as Long et al. [13] simplified the clamping areas so that the calculation can be made faster and also acceptable results. They clamp the areas different between laminate and cut-out regions on both sides.

For the completeness of the modelling strategy in the LVI process, failure initiation and progression need to be predicted in a proper way through the implementation of the progressive damage model for composite laminates, which include damage criteria and evolution law. In previous research works, three dimensional (3D) Hashin failure criteria [14] have extensively used as initiation criteria to detect the failure, especially for uni-directional (UD) composite laminates because of its credibility to isolate different mode of failures. Long et al. [13] and Tie et al. [15] performed the failure analysis of the LVI using Hashin formulation and linear degradation scheme for progression law. Another researcher like Tie et al. [2] predicted the failure in

laminates due to impact loading using Hashin criteria together with continuum damage mechanics (CDM) degradation law. They conclude that this combination agrees well with test results.

Although the above researchers have analysed many aspects of modelling techniques in low-velocity impact through experiment and numerical simulations, the proper process guideline needs to be emphasized especially in establishing the boundary condition and implementation of progressive damage law in impact laminates. In addition, no universal damage initiation criteria that can represent all types of loading and hence leads to many researches that still introduced new approaches including this publication. Since the prior research in this area was inconclusive, this article aims to provide the details of clamping approaches (boundary condition) and failure prediction approach where the performance of the proposed model was compared between experimental data and the simulation. Three boundary conditions were used to study the effect of simplification of clamping areas together with Puck failure criteria to predict the intralaminar damage in the laminates for such type of loading. Prediction of delamination is achieved via the implementation of cohesive contact formulation which also used bilinear traction function as embedded in Abaqus software. It is hoped that the methodology proposed in this article can be a great design tool for more realistic composite parts and structures in the case of LVI.

Methods

Finite Element Modelling

The impact test was simulated using the FE method in Abaqus/Explicit platform. The laminates were produced from CCF300/epoxy composite material. The laminate material properties were summarized in Table 1, while experimental data was obtained from the publication of Han et al. [7]. The laminate consists of $[45/0/-45/90]_4$ stacking sequences with a total thickness of 4 mm. To reduce the computational time, the global-local approach was employed where the layup arrangement was modified and rearranged according to $[45_4/0_4/-45_4/90_8/-45_4/0_4/45_4]$ stacking sequence. For this configuration, only six cohesive interfaces required. The layup modification can be viewed in Figure 1, while the interfacial properties are shown in Table 2. The intralaminar region meshed with eight-node linear brick reduced integration elements (C3D8R). To capture the damage pattern effectively, the region nearby impacted areas was modelled with finer mesh size compare with areas further away from the impacted zone.

Besides that, the impactor (ball) was modelled based on the analytical rigid body using the rigid element type (R3D4) because the stiffness of the steel ball is much higher than CFRP laminate. The diameter of the impactor is

16 mm having a mass of 5.36 kg which was applied to the model using reference point (RP) of the rigid body. The impactor was constrained in the translational degree of freedom x - and y -axes and rotational degree of freedom in all directions. The initial velocity was applied in z -direction through RP of the body and later is used to extract the result for contact force between the impactor and the laminate.

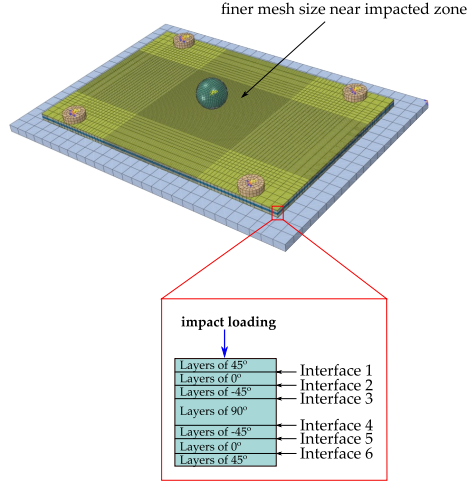


Figure 1: Local-global approach in defining the stacking sequences and meshing strategy for the LVI plate.

Table 1: The Mechanical Properties of CCF300/epoxy [7]

Category	Properties
Elastic	$E_1 = 123.91$ GPa, $E_2 = E_3 = 9.72$ GPa, $G_{12} = G_{13} = 4.53$ GPa, $G_{23} = 2.56$ GPa, $\nu_{12} = \nu_{13} = 0.288$, $\nu_{23} = 0.347$
Strength	$X_t = 1762.3$ MPa, $X_c = 1362.2$ MPa, $Y_t = 71.1$ MPa, $Y_c = 218.3$ MPa, $S_{12} = S_{13} = S_{23} = 83.5$ MPa
Density	$\rho = 1.5 \times 10^{-9}$ tonne/mm ³

Table 2: The Cohesive Properties of CCF300/epoxy [7]

$K_{nn} = K_{ss} = K_{tt}$	$t_n^o = t_s^o = t_t^o$	G_n^c	$G_s^c = G_t^c$
1×10^5 MPa	80 MPa	556 J/m ²	1497 J/m ²

In this article, three different models that emphasizing the boundary condition of gripping/clamping zones were analysed together with the

proposed progressive damage model. The complete description of the boundary condition and the specific model developed is illustrated in Figure 2. The analysis was carried out based on the impact energy of 4.45 J/mm which produced an initial velocity of 2.577 m/s. The contact between the impactor and the laminate was defined using general contact, and “hard contact” was specified in the normal direction. Finally, the contact force-time and load-displacement curves were extracted from the output files, and the quality of the results was compared with experimental data, as well as among the simulation data itself.

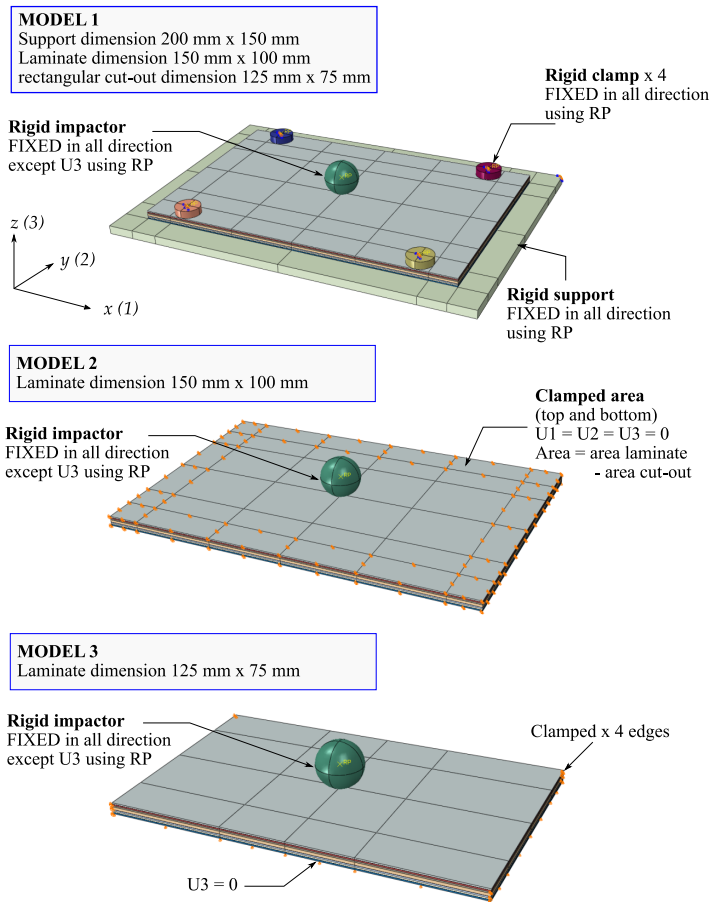


Figure 2: Different geometrical model compared in this article.

Puck’s Intralaminar Damage Model

The identification and evaluation of damage initiation have been evaluated using 3D Puck failure criteria [16,17], which can distinguish fiber failure and inter-fiber failure in tension and compression. The background of this theory was extended from Hashin's failure criteria [14]. The analytical equations represent the fiber failure (FF) in composite laminate is written in the following forms:

Fiber failure in tension:

$$f_t = \frac{1}{X_t} \left[\sigma_1 - \nu_{12} - \nu_{12f} m_{\sigma f} \frac{E_{11}}{E_{11f}} (\sigma_2 + \sigma_3) \right] \text{ for } [\dots] \geq 0 \quad (1)$$

Fiber failure in compression:

$$f_c = \frac{1}{|X_c|} \left[\sigma_1 - \nu_{12} - \nu_{12f} m_{\sigma f} \frac{E_{11}}{E_{11f}} (\sigma_2 + \sigma_3) \right] \text{ for } [\dots] < 0 \quad (2)$$

Where X_t and X_c are the tensile and compressive strengths of a UD layer in the longitudinal direction and ν_{12} and ν_{12f} are the Poisson's ratio for UD lamina and fibre, respectively. The mean stress magnification factor, $m_{\sigma f}$ is assumed to be 1.3 for glass fiber and 1.1 for carbon fiber [18].

For inter-fiber failure (IFF), also referred to as matrix cracking assumes that fracture in the laminate is resulted by the stresses acting on the fracture plane (FP) (σ_n, τ_{nl} and τ_{nt}) inclined θ_{FP} with respect to the material plane. The classical transformation equations are used to obtain the normal and shear stresses previously mentioned. The IFF function relies on the stresses acting on the fracture plane, and formulated as:

Inter-fiber failure in tension:

$$f_t(\theta) = \sqrt{\left(\left(\frac{1}{R_{\perp}} - \frac{P_{\perp\psi}^+}{R_{\perp\psi}} \right) \sigma_n(\theta) \right)^2 + \left(\frac{\tau_{nt}(\theta)}{R_{\perp\perp}} \right)^2 + \left(\frac{\tau_{nl}(\theta)}{R_{\perp\parallel}} \right)^2} + \frac{P_{\perp\psi}^+}{R_{\perp\psi}} \sigma_n(\theta) \text{ for } \sigma_n \geq 0 \quad (3)$$

Inter-fiber failure in compression:

$$f_c(\theta) = \sqrt{\left(\frac{P_{\perp\psi}^-}{R_{\perp\psi}}\sigma_n(\theta)\right)^2 + \left(\frac{\tau_{nt}(\theta)}{R_{\perp\perp}}\right)^2 + \left(\frac{\tau_{nt}(\theta)}{R_{\perp\parallel}}\right)^2} + \frac{P_{\perp\psi}^+}{R_{\perp\psi}}\sigma_n(\theta) \quad \text{for } \sigma_n < 0 \quad (4)$$

The parameter ψ denotes the shear angle in action plane, R_{\perp} is failure resistance normal to fibers direction, and $R_{\perp\psi}$, $R_{\perp\perp}$ and $R_{\perp\parallel}$ are the fracture resistances of the action plane due to the shear stressing.

For the sake of simplification, other parameters required to complete and calculate Equation (3) and Equation (4) were evaluated from the literature [18]. To describe the elastic-brittle behaviour of fiber-reinforced composites, a constitutive model suited for composite material was used, where Lee et al. [19] was successfully performed their numerical model to identify the onset of failure as well as damage progression. A 3D-damaged stiffness matrix is written as:

$$C^d = \begin{bmatrix} \beta C_{11} & \kappa C_{12} & \kappa C_{13} & 0 & 0 & 0 \\ \kappa C_{21} & \kappa C_{22} & \kappa C_{23} & 0 & 0 & 0 \\ \kappa C_{31} & \kappa C_{32} & \kappa C_{33} & 0 & 0 & 0 \\ 0 & 0 & 0 & \beta\omega G_{12} & 0 & 0 \\ 0 & 0 & 0 & 0 & \beta\omega G_{13} & 0 \\ 0 & 0 & 0 & 0 & 0 & \beta\omega G_{23} \end{bmatrix} \quad (5)$$

Where C_{ij} is an undamaged stiffness component, and G_{12} , G_{13} and G_{23} are the in-plane and out-of-plane shear modulus of composite material. The multiplication factors β , κ , and ω were defined as following:

$$\begin{aligned} \beta &= 1 - d_f \\ \kappa &= (1 - d_f)(1 - d_m) \\ \omega &= (1 - S_{mt}d_{mt})(1 - S_{mc}d_{mc}) \end{aligned} \quad (6)$$

Where d_f and d_m are the global damage variables corresponding to fibre and inter-fibre failure, respectively. Individual damage variables based on failure mode are represented by d_{ft} , d_{fc} , d_{mt} and d_{mc} for fibre failure in tension and compression and inter-fibre failure in tension and compression, respectively. The relationship between global and local variables is defined as $d_f = 1 - (1 - d_{ft})(1 - d_{fc})$ and $d_m = 1 - (1 - d_{mt})(1 - d_{mc})$. The control

parameters, S_{mt} and S_{mc} are 0.9 and 0.5, respectively as suggested in the Abaqus manual.

Interlaminar Damage Model

Delamination was simulated by cohesive surface behaviour using a cohesive contact interface. Based on the formulation, the fracture-separation law was employed to control the interaction between traction stress and separation displacement in the model as written in matrix form below:

$$t = \begin{bmatrix} t_n \\ t_s \\ t_t \end{bmatrix} = \begin{bmatrix} K_{nn} & 0 & 0 \\ 0 & K_{ss} & 0 \\ 0 & 0 & K_{tt} \end{bmatrix} \begin{bmatrix} \delta_n \\ \delta_s \\ \delta_t \end{bmatrix} \quad (7)$$

Where t_n , t_s and t_t are the interface strength under the failure mode I, II, and III respectively. The damage initiation and progression based on delamination mode is summarized in Table 3.

Table 3: Failure criteria for delamination

Approach	Cohesive contact interface
Damage initiation	Quadratic nominal stress criterion $\left\{ \frac{t_n}{t_n^0} \right\}^2 + \left\{ \frac{t_s}{t_s^0} \right\}^2 + \left\{ \frac{t_t}{t_t^0} \right\}^2 = 1$
Damage evolution	Power law fracture criterion $\left\{ \frac{G_n}{G_n^c} \right\}^\alpha + \left\{ \frac{G_s}{G_s^c} \right\}^\alpha + \left\{ \frac{G_t}{G_t^c} \right\}^\alpha = 1$

From Table 3, t_i ($i = n, s, t$) is the interface strength parameters, G_i^c ($i = n, s, t$) is the critical fracture energy needed to cause damage in the normal and two shear directions and α is the material parameter (i.e. $\alpha = 1$). The onset of delamination can be identified whenever the quadratic function achieved unity (=1). Once the damage criteria are satisfied, the cohesive stiffness degraded according to the power law.

Numerical Result and Discussion

The numerical simulation is focused on CCF300/epoxy composite with different modelling techniques on the boundary condition of clamped areas based on impact energy of 4.45 J/mm. The contact force and load-displacement

diagram were recorded for determining the performance of the proposed model and the damage model.

Analysis of Modelling Boundary Condition

This sub-section analyses the effect of boundary condition on the LVI specimen in predicting the failure in a composite laminate. The simulated impact force-time curves from 3 models are compared with the experiment curve and result in Figure 3 revealed that the duration of impact force in virtual test curves is slightly shorter than the real curve which is mainly due to the philosophy of applied boundary condition. As a comparison, model 1 and 2 are closely mimicked the test curve because of the boundary condition includes the rubber grips and cut-out support, however, over estimates the ultimate impact force. Model 3 and the proposed model of Han et al. [7] are performed better in predicting the contact force, and the simulated results agreed well with the experiment.

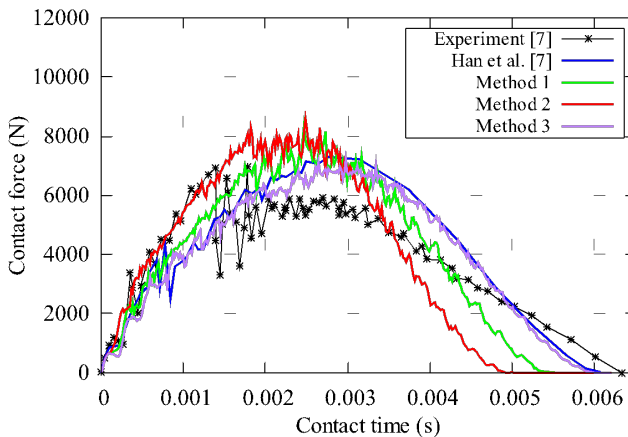


Figure 3: Comparison of simulation and experimental data for contact force vs time of CCF300/epoxy laminate.

Figure 4 shows the force-displacement curve for the models investigated in this paper. Because of no reference on the force-displacement curve from the experiment, the comparison is only made based on these three models. The prediction of the load-displacement curve shows a similar pattern in all cases where model 1 and model 3 gave better results in producing lower energy absorption. Model 3 can be used as an optimized tool to reduce the calculation time and at the same time produced reasonable results. Model 1 used less time to bounce back the impactor and utilized low kinetic energy as compared to other models.

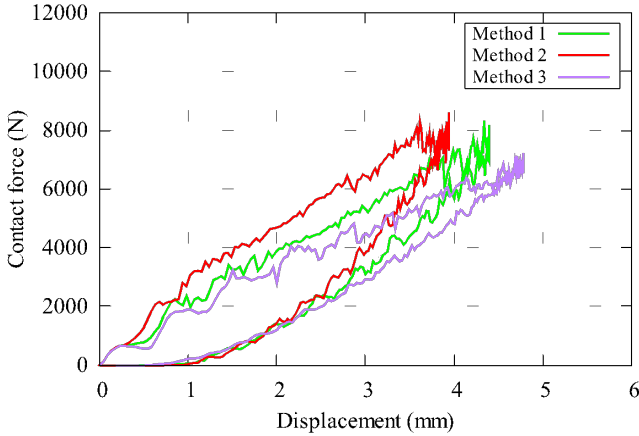


Figure 4: Simulated force-displacement of CCF300/epoxy LVI laminate under model 1, 2 and 3

Table 3 demonstrates the performance of models in absorbing the impact energy. Results indicated that Model 2 absorbed the highest energy compare to the other two models due to the nature of the clamped areas which was bigger than model 1. The structure becomes more rigid and causes higher energy required to bounce back the impactor. Model 3 utilized only an “edge line” for the un-supported laminate, which produced lower energy value.

Table 3: Analysis of energy absorption for proposed models based on impact energy of 4.45 J/mm

Model	Energy absorbed (J)
Model 1	7.883
Model 2	9.276
Model 3	6.535

Analysis of Damage Initiation and Growth

With the impact energy of 4.45 J/mm selected in this analysis, only matrix failure observed as shown in Figure 5. Red/dark color indicates full damage, while other colors exhibit no failure area. Matrix damage radius increases for matrix failure in tension measured from impacted point to the bottom layer of the laminates, while decreases for compressive matrix failure. These trends similarly observed in the original publication [7]. The failure in fiber modes is not observed here due to the inadequate impact energy applied to the composite plate that can break the fiber inside it.

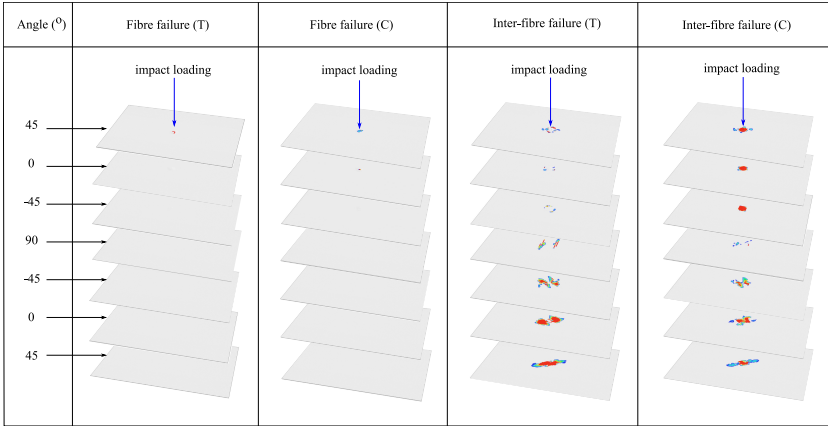


Figure 5: Intralaminar morphology for the impact energy of 4.45 J/mm (for Model 1)

Delamination or debonding is another area of interest in predicting total failure due to impact loading. As can be seen in Figure 6, the damage morphology indicates the area of delamination getting bigger towards the 90° layups, and slowly decreases approaching the last bottom layers. The existence of delamination boosts the process of damage accumulation by degrading the stiffness of the laminate.

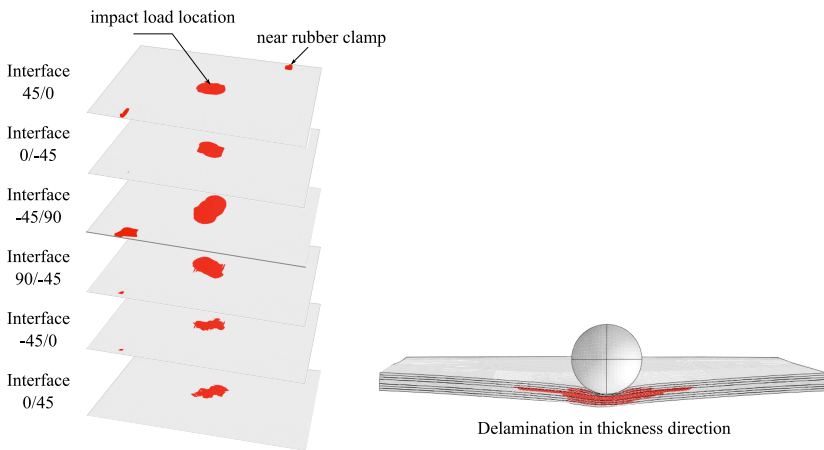


Figure 6: Delamination morphology for the impact energy of 4.45 J/mm (Model 1) (red/dark color defines the failure area)

Conclusions

In this paper, Puck damage criteria incorporated with a gradual degradation scheme and cohesive damage formulation were proposed to study the failure mechanism of fiber and matrix components as well as the structural response of CCF300/epoxy composite laminate subjected to low-velocity impact loading. The damage model is used to study the damage morphology, as well as the force-displacement response of the impactor. The cohesive theory is applied to the FE model to detect and trace the phenomena of delamination. Based on the simulations conducted, it has been concluded that:

- In general, the proposed damage model can predict the contact force and damage failure modes consistently with the test result.
- The full-scale FE model (model 1) has performed excellently in capturing the structural response, while satisfactorily predict the peak force. Since no information obtained from the experiment, further comparison cannot be made regarding on efficiency of the load-displacement curve.
- Due to the inadequate magnitude of impact energy, no trace of fiber failure (FF) can be viewed in the analysis of results. Matrix failures are the main contributor to the total failure in the laminate for LVI structure.
- The low-velocity impact results in the delamination in all sub-laminate, which varies in terms of areas based on the location from the impacted point.

References

- [1] Yang L, Wu Z, Gao D, Liu X., “Microscopic damage mechanisms of fibre reinforced composite laminates subjected to low velocity impact,” *Computational Materials Science* 111, 148–156 (2016).
- [2] Tie Y, Hou Y, Li C, Zhou X, Sapanathan T, Rachik M., “An insight into the low-velocity impact behavior of patch-repaired CFRP laminates using numerical and experimental approaches,” *Composite Structures* 190, 179–188 (2018).
- [3] Gliszczynski A., “Numerical and experimental investigations of the low velocity impact in GFRP plates,” *Composites Part B: Engineering* 138, 181–193 (2018).
- [4] Perillo G, Vedvik NP, Echtermeyer AT., “Numerical analyses of low velocity impacts on composite. Advanced modelling techniques,” In: *Proceedings of the Simulia customer conference* (2012).
- [5] Zhang J, Zhang X. “An efficient approach for predicting low-velocity impact force and damage in composite laminates,” *Composite Structures*.130, 85–94 (2015).

- [6] Maio L, Monaco E, Ricci F, Lecce L., “Simulation of low velocity impact on composite laminates with progressive failure analysis,” *Composite Structures* 103, 75–85 (2013).
- [7] Han G, Guan Z, Li X, Du S., “Failure analysis of carbon fiber reinforced composite subjected to low velocity impact and compression after impact.,” *Journal of Reinforced Plastics and Composites* 35(9), 727-746 (2016).
- [8] Liu PF, Liao BB, Jia LY, Peng XQ, “Finite element analysis of dynamic progressive failure of carbon fiber composite laminates under low velocity impact,” *Composite Structures* 149, 408–422 (2016).
- [9] Lou X, Cai H, Yu P, Jiao F, Han X., “Failure analysis of composite laminate under low-velocity impact based on micromechanics of failure,” *Composite Structures* 163 (2017).
- [10] Singh H, Namala KK, Mahajan P., “A damage evolution study of E-glass/epoxy composite under low velocity impact,” *Composites Part B: Engineering* (2015).
- [11] D7136 A., “Standard Test Method for Measuring the Damage Resistance of a Fiber-Reinforced-Polymer Matrix Composites to a Drop-Weight Impact event,” *Book of Standards* 15 (2005).
- [12] Riccio A, De Luca A, Di Felice G, Caputo F., “Modelling the simulation of impact induced damage onset and evolution in composites,” *Composites Part B: Engineering* 66, 340–347 (2014).
- [13] Long S, Yao X, Zhang X., “Delamination prediction in composite laminates under low-velocity impact,” *Composite Structures* 132, 290–298 (2015).
- [14] Hashin Z., “Fatigue Failure Criteria for Unidirectional Fiber Composites,” *Journal of Applied Mechanics* 48(4), 846 (2009).
- [15] Du J, Tie Y, Li C, Zhou X., “Numerical and experimental study for damage characterization of composite laminates subjected to low-velocity impact,” *Materials Physics and Mechanics* 27(2), 195–204 (2016).
- [16] Puck A., “Failure Analysis of FRP Laminates By Means of Physically Based Phenomenological Models,” *Composites Science and Technology* 58(7), 1045–1067 (1998).
- [17] Puck A, Deuschle HM., “Progress in the Puck Failure Theory for Fibre Reinforced Composites : Analytical solutions for 3D-stress,” *Composites Science and Technology* 62, 371–378 (2002).
- [18] Puck A, Kopp J, Knops M., “Errata to ‘Guidelines for the determination of the parameters in Puck’s action plane strength criterion,’” *Composites Science and Technology* 62(9), 1275 (2002).
- [19] Lee CS, Kim JH, Kim SK, Ryu DM, Lee JM., “Initial and progressive failure analyses for composite laminates using Puck failure criterion and damage-coupled finite element method,” *Composite Structures* 121(0), 406–419 (2015).

Optimization of Tool Life and Surface Roughness for Hypereutectic Al – Si Alloys in Face Milling

Kamal Othman^{1, 2*}, Jaharah Abdul Ghani¹, Afifah Juri¹, Mohd Shahfizal Ruslan Mohd², Shahir Kassim³, Che Hassan Che Haron¹

¹Department of Mechanical and Material Engineering,
Faculty of Engineering and Built Environment,
Universiti Kebangsaan Malaysia, 43600, Bangi, Selangor, Malaysia

²Department of Mechanical Engineering, German Malaysian Institute,
43000 Kajang, Selangor, Malaysia

*Corresponding author E-mail: kamal@gmi.edu.my

³Faculty of Manufacturing Engineering, Universiti Teknikal Malaysia Melaka (UTeM), Hang Tuah Jaya, 76100 Durian Tunggal, Melaka, Malaysia

ABSTRACT

The automotive industry is looking to adopt environmentally-friendly machining processes for automotive components. This study intends to investigate the machining parameters affecting the machinability of hypereutectic Al-Si alloys in the context of surface roughness and tool life via a DLC coated face milling cutter inserted under dry cutting conditions. The machining parameters used in this study were cutting speeds of 250 m/min and 350 m/min, feed rates of 0.02 mm/tooth and 0.04 mm/tooth, and a constant depth of cut of 0.3 mm. The orthogonal full factorial (2³) method was used for the experimental trials. A commercial software called Minitab 17 was used to generate the analysis of variance (ANOVA) and the mathematical prediction model for each machining response. The experimental results confirmed that an excellent surface finish was achieved with a value of as low as 0.140 µm, while the highest value for tool life of 105.47 minute was realized with face milled aluminium alloy A390. From the analyses, it was confirmed that the feed rate is the most significant machining factor affecting surface roughness, while in the case of tool life; cutting speed is the most influential machining factor. The main effect plot showed that the optimum cutting condition for

realizing low surface roughness and longer tool life is at 250 m/min, a feed rate of 0.02 mm/tooth, and radial depth of cut 12.5 mm. The prediction model for surface roughness and tool life was developed and reported low percentage errors.

Keywords: *Face milling; Dry cutting; diamond like carbon (DLC); Hypereutectic Al-Si alloys; Tool life; Surface roughness.*

Introduction

Aluminum Silicon (Al-Si) alloys with a silicon content of more than 13% are called hypereutectic alloys. It is widespread in many light-weight and high-strength applications, especially in the automotive industry. A390 is a form of hypereutectic Al–Si alloys which has excellent properties such as high resistance to wear, good mechanical and physical properties, good corrosion resistance and high thermal conductivity, which is therefore suitable for automobile applications. These types of properties are of increasingly high interest to the automotive industry especially in the fabrication of light-weight components such as connecting rods, cylinder liners, and engine blocks [1]. Some companies such as BMW, Mercedes, Volkswagen and Porsche are using hypereutectic Al–Si alloys to produce engine blocks [2].

Among traditional machining processes, the milling process is one of the most commonly used techniques, second only to the turning process, particularly for finishing machined components. Concurrently, the manufacturing sector strives for an efficient manufacturing process which is less costly while producing high quality products quickly [3]. The face milling process is one of the most economical material removal strategies that is frequently used in the automotive industry for cutting metal to an acceptable surface quality. Surface finish is a vital parameter in the assurance of part quality [4]. Also, a high-quality machined surface essentially enhances fatigue strength, corrosion resistance and creep life [5]. The behind-the-metal cutting process is very important towards producing components which possess consistent dimensional accuracy and excellent surface integrity. During the machining process, friction and heat generation occurs due to the tool's face contact with the workpiece which influences the machining quality of the machined surface because of the relationship between the roughness of the machine surface and tool life [6]. Over the years, attention on workpiece surface quality produced by faced milling process is increasing widely. Moreover, the roughness of a machined surface dictates the tolerances, which is a critical constraint in selecting suitable machine and cutting parameters [7]. Another machining response which has commanded the attention of manufacturers is tool life, which is expressed as the amount of time or excellent

performance the tool can provided prior to failure. The tool is deemed to fail when it reaches a certain wear criteria. The tool wear process occurs over time, and it grows slowly in tandem with machining time. Thus, it can be said that tool life is the length of period of actual machining time, where the fresh sharp tool can work before reaching the specified wear criteria [8].

According to Kelly and Cotterell [9], machining aluminum alloys results in low cutting forces and low temperatures. Despite these advantages, aluminum alloy is also known to be difficult to machine, due to its low melting point and high thermal expansion characteristics. This makes the alloy absorb a considerable amount of heat when machining under dry conditions, which results in the chip adhering to the cutting tool, worse workpiece surface roughness, and geometrically formed errors for finished products.

Among the various types of aluminum alloys, hypereutectic Al-Si alloy is one of the hardest to machine. The presence of silicon at ~17-18% increases its strength at the expense of ductility [10] while significantly impacting its machinability [11]. During the machining of the hypereutectic Al-Si alloys, the insert tips make direct contact of soft aluminium phase and hard silicon particles, which increases the abrasive wear due to the resistance of hard silicon particles while increasing the silicon particles size [12]. This will inevitably affect the workpiece surface roughness and tool's life time.

The types of cutting tools suitable for machining of Al-Si alloys are usually cemented carbide and PCD (polycrystalline diamond). Applying cemented carbide facilitates the adhering of aluminum chips on the cutting tool due to the low melting point of aluminum silicon alloys. This reduces the tool life as cutting tool failure occurs due to fracture of the cutting edges [13]. This problem can be circumvented by using DLC (diamond-like carbon) coated cutting tools [14]. The properties of DLC coating offer a very low friction coefficient and excellent hardness relative to the uncoated carbide. It is also less costly than polycrystalline coating (PCD). Yokota et al. [15] reported a significant decrease in the coefficient of friction, from 0.8% to 0.3%, relative to uncoated cutting tools when carrying out dry intermittent cutting of an aluminum alloy 5052 with DLC coated carbide cutting tools.

Recently, manufacturers and researchers have been paying great attention to the concept of sustainability in manufacturing processes. To prevent the use of hazardous liquid cutting fluids in the material removal strategies, experimentalists have been machining components without the use of cutting fluids, a condition known as "Dry Machining" [16]. Dry cutting is one of the "greener" environmentally-friendly alternatives, and has been growing in demand in the automotive industry [17]. The advantages of dry machining are that it is non-polluting to the atmosphere, is not dangerous to health, has reduced disposal costs, has reduced cleaning costs and is harmless to the skin [18] – [19].

Previous research has determined the surface finish and tool life when dry cutting during machining of aluminum alloy. Torres et al. [20] investigated the influence of different machining parameters, such as depth of cut, feed rate, cutting speed, and tool radius when machining A2030-T4 aluminum alloy. The experimental outcomes revealed that the collaboration between the machining parameter feed rate and depth of cut resulted in the huge impact in dry cutting of the Al-Cu alloy. Kuram and Ozcelik [21] reported similar results, where the ANOVA analysis confirmed that on account of surface finish, the feed per tooth was the most significant machining factor.

Pattnaik et al. [22] found that undesirable continuous types of chips were formed when cutting rolled aluminum alloy due to its ductility. They stated that the chip destruction and wear effect which occurred during machining of aluminum significantly affected tool life. The chip destruction took place due to the friction generated between the rake face near to the nose and the chip. When the level of destruction increases during cutting, it means that the level of rubbing between chip and tool increases, which culminates in poor tool life. Therefore, lower level of chip destruction is preferred during machining. However, dry cutting also has some positive effects, such as reduction in thermal shock, and hence, improved tool life in an interrupted-cutting environment.

Ariff et al. [23] determined the optimal cutting conditions when machining aluminum alloy utilizing TiCN and TiN coated tools under dry conditions. It was confirmed that superior results were obtained using a TiCN coated tool, due to the fact that it increases the tool life by 74% under dry machining. Consequently, the ideal cutting speed for dry cutting of T6061 aluminum alloy utilizing TiCN coated cutting tools is a cutting speed of 394 m/min, a feed rate of 0.6 mm/rev and a depth of cut of 0.4 mm.

Based on literature on machining aluminum alloy, there has not been any research on the impact of machining on surface finish and tool life during dry milling of A390 Al-Si alloy. This paper details the study on the machining parameters affecting the machinability of hypereutectic Al-Si alloys in the context of surface roughness and tool life using a face milling cutter with diamond like carbon (DLC) coated inserted under dry cutting conditions.

Experimental Work

Dry cutting procedures were conducted using a CNC milling machine (VC SPINNER 450). This vertical milling machine has the capability to achieve a maximum speed of 15,000 RPM. The workpiece material used for this experiment was A390 Al-Si alloy with dimensions of 50x50x125 mm. Prior to the machining test, the surfaces of the workpiece materials were pre-milled to ensure the removal of the original layer of the workpiece, due to difference of

hardness at the skin layer and inner workpiece, which could affect the machining responses. The chemical compositions of the A390 Al-Si alloy were as displayed in Table 1. A Sumitomo face mill cutter diameter 50 mm with indictable inserts was used for the experiments. The insert was DLC (diamond like carbon) coated carbide cutting tool. Figure 1 shows the dimensions of the DLC coated cutting tool.

Table 1: The Composition of A390 Al-Si alloy [24]

Element percentage (%)						
Al	Si	Cu	Mg	Fe	Ti	P
balance	17.51	4.12	0.43	0.28	0.06	0.06

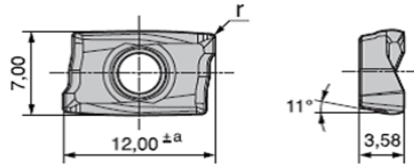


Figure 1: DLC coated cutting tool dimensions in mm

Surface roughness (Ra) was measured by using a Mitutoyo roughness tester (model SJ-310). The measurements were recorded at the starting of the cutting process to avoid the effects of tool wear which could change the Ra value. The measurements were carried out three times for each machine surface, and the average values were calculated for further analysis. The tool wear measurements on the flank face were taken for each run using an Olympus SZ61 stereo measuring microscope. The experiment was stopped at the average wear of 0.3 mm (tool life criterion), as per ISO-8688. A Hitachi Tabletop scanning electron microscope (SEM) was utilized to examine the types of wear mechanisms.

Table 2 shows the range of the cutting parameters used in this study. They were selected based on the manufacturer’s recommended cutting conditions and also based on previous studies. Table 3 shows the full factorial design of experiment used to perform the experimental trials.

Table 2: Cutting parameter

Cutting Parameter	Level 1	Level 2
Cutting speed (m/min)	250	350
Feed rate (mm/tooth)	0.02	0.04

Radial depth of cut (mm)	12.5	25
Axial depth of cut (mm)	0.3	0.3

Table 3: Details of experimental design

Exp. no.	Cutting speed (m/min)	Feed rate (mm/tooth)	Radial depth of cut (mm)	Axial depth of cut (mm)
1	250	0.02	12.5	0.3
2	250	0.02	25.0	0.3
3	250	0.04	25.0	0.3
4	350	0.02	12.5	0.3
5	350	0.02	25.0	0.3
6	350	0.04	12.5	0.3
7	350	0.04	25.0	0.3
8	250	0.04	12.5	0.3

Results and Discussion

The analysis of variance was employed to determine the machining factor most affecting the machining responses. The main effect plot analysis was utilized to study how one or more machining factors influenced the machining response, and also to determine the optimum cutting parameters following each machining responses characteristic. The interaction effects were not taken into account due to the absence of the interaction effects of process parameters. Interaction effects are unimportant for improving surface roughness and for maximizing tool life.

Analysis of Surface Roughness

Surface roughness is one of the most important machining responses studied by most researchers and is also usually a requirement of customers. The value of surface roughness largely depends on the cutting conditions used during the machining process. Figure 2 shows the measurements of surface roughness achieved from 8 experimental trials. Generally, the surface value obtained was 0.140 - 0.212 μm . Based on Figure 2, it can be seen that experiment 1 resulted in the smoothest surface roughness value, while experiment 7 generated the roughest value. It would seem that when comparing both tests, the cutting speeds were similar when there were high values of feed rate and radial depth of cut from experiment 3 – experiment 8. It can therefore be surmised that increase of feed rate and radial depth will result in an increase of the surface roughness value.

It can be seen that a most extreme enhancement of 34% in surface roughness is possible using experiment 1 cutting conditions relative to experiment 7. By comparing cutting parameters of both experiments, it can be confirmed that decreasing the cutting speed, feed rate, and radial depth positively influences the surface finish value.

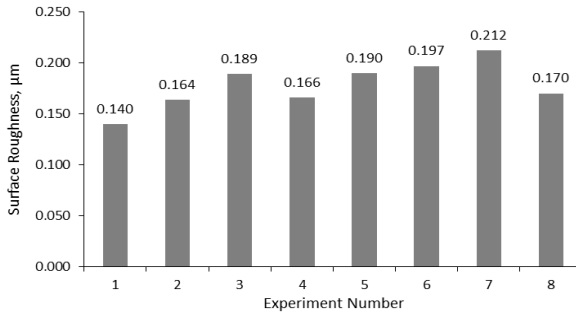


Figure 2: Measurement of surface roughness

ANOVA and Prediction Modelling for Surface Roughness

ANOVA analysis at confidence level of 95%, and 5% significance level were used to analyze the experimental data and determine the most significant machining factor which could greatly influence the machining responses. The ANOVA table consists of the sum of square (SS), degree of freedom (DF), mean square (MS), P-value and F-value. In ANOVA analysis, P-value and F-value can be used to compare and determine the significant machining factor. The significant machining factor can be dictated by the lower P-value or larger of F-value. The lower the P-value or the larger the F-value, the larger the influence that factor will have on the machining response. Ross [25] also stated that a bigger F-value demonstrates a more prominent effect on the machining execution characteristics.

Table 4 shows the resulted ANOVA response table of Ra. Based from the results, it can be seen that the most significant machining parameter affecting Ra is feed rate followed by cutting speed and radial depth. It was proven with the generated lowest P-value at 0.000 and the largest F-value at 201.10. Previous researchers reported similar results. They claimed that the surface roughness is essentially influenced by the feed rate [26]-[27]. According to Bouacha et al. [28], this could be due to the theoretical geometrical surface finish, where Ra is basically an element of the feed for a given nose radius and this changes with the square of the feed rate value.

Table 4: ANOVA response table of Ra

Source	Seq. SS	DF	Adj. SS	Adj. MS	F-Value	P-value
Regression	0.003599	3	0.003599	0.001200	165.47	0.000
Cutting Speed	0.001301	1	0.001301	0.001301	179.38	0.000
Feed rate	0.001458	1	0.001458	0.001458	201.10	0.000
Radial Depth	0.000840	1	0.000840	0.000840	115.93	0.000
Error	0.000029	4	0.000029	0.000007		
Total	0.003628	7				

It can be seen in Table 4 that there was no interaction between cutting speed, feed rate and radial depth on the surface roughness. A prediction model of surface roughness was generated by adapting multiple regression analysis to the experimental data. Equation 1 represents the empirical relation in the context of actual factors:

$$Ra = 0.03075 + 0.000255 \text{ Cutting Speed} + 1.3500 \text{ Feed} + 0.001640 \text{ Radial depth of cut} \quad (1)$$

A graphical comparison between the actual experimental data and predicted Ra was constructed as shown in Figure 3. The relative percentage errors recorded for the relationship between the predicted and actual values were from 0.53% to 1.42%. It was an acceptable percentage error, as it was below 20% [29]. Hence, the general pattern in surface roughness variation appears to be well described by the prediction models.

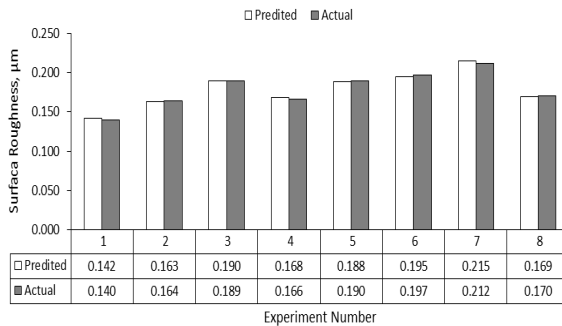


Figure 3: Comparison between actual and predicted Ra

Main Effect Plot Surface Roughness

To understand the impact of a single machining factor, the main effect plot is shown in Figure 4. According to Simao et al. [30], by using the main effect plot, where there is the steepest slope and the longest line, it suggests that the

respective factor has a huge effect of the yield measure, while when the lines are comparable in slant and length, the components would for the most part similarly affect the yield measure, thus, no one factor has a more huge impact than another. From Figure 4, it shows that the feed rate factor has the steepest slope and longest line compared to the others, thus confirming the conclusion where the most significant machining factor influencing the surface finish response is feed rate.

The lowest of surface roughness value signifies the lowest values of mean surface roughness for each machining parameter such as cutting speed, feed rates, and radial depth. Based on the data in Figure 4, it can be seen that the most preferable machining parameter for Ra is at 250 m/min cutting speed, 0.02 mm/tooth feed rate and 12.5 mm radial depth.

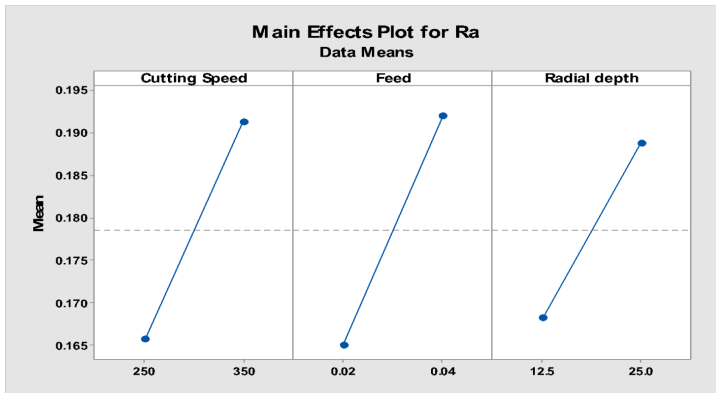


Figure 4: Main effect plot for Ra

Tool Life Analysis

Tool life is an important machining response which acts as an indicator for milling processes in the manufacturing sector. Increasing tool life can improve process efficiencies and enhance part quality. Figure 5 shows the graphic representation of tool life measured during the machining process. Generally, the range of tool life achieved was between 11.24 - 105.47 min. The highest tool life was achieved in experiment 1 with tool life of 105.47 min, with a cutting speed of 250 m/min, a feed rate of 0.02 mm/tooth and a radial depth of cut of 12.5. The lowest tool life of 11.24 min was obtained in experiment 7, with a cutting speed of 350 m/min, a feed rate of 0.04 mm/tooth and a radial depth of cut of 25 mm.

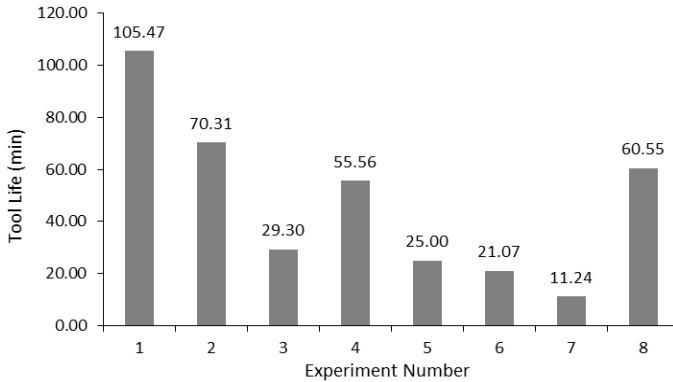


Figure 5: Measured value of tool life

ANOVA and Prediction Modelling for Tool Life

ANOVA analysis at a confidence level of 95% was conducted to analyze the experimental data and determine the most significant machining factor that can significantly influence tool life. Table 5 shows the resulting ANOVA analysis of tool life. It can be seen that the most significant machining factor affecting tool life is cutting speed with the generated lowest P-value of 0.005 and the largest F-value of 31.25. K ok [31] and Ojolo and Ogunkomaiya [32] also obtained similar results, where cutting speed was the most influential factor when machining 2024 Al alloy and medium carbon. In the machining process, as cutting speed increases, the temperature also increases and this heat is generated even by the very small contact area of tool. This result in higher tool wear rate, which significantly affects the tool life [33].

Table 5: ANOVA analysis of tool life

Source	Seq. SS	DF	Adj. SS	Adj. MS	F-value	P-value
Regression	6593.3	3	6593.3	2197.76	23.55	0.005
Cutting Speed	2917.0	1	2917.0	916.95	31.25	0.005
Feed rate	2250.5	1	2250.5	2250.53	24.11	0.008
Radial Depth	1425.8	1	1425.8	1425.78	15.28	0.017
Error	373.4	4	373.4	93.34		
Total	6966.6	7				

Based on Table 5, there is no interaction between cutting speed, feed rate and radial depth towards generating the tool life machining response. The prediction model of tool life was generated by adapting multiple regression analyses to the experimental data. Equation 2 represents the empirical relation in the context of actual factors:

$$\text{Tool life} = 252.3 - 0.3819 \text{ Cutting Speed} - 1677 \text{ Feed} - 2.136 \text{ Radial depth of cut} \quad (2)$$

A graphical comparison between the actual experimental data and predicted tool life model was constructed, as shown in Figure 6. The error percentages between the predicted and actual values are between 0.68% and 116.99%. These were unacceptable percentage errors, as they were above 20%. There may have been one or two outliers. These will complicate the description of the error. Thus, to detect the outlying data the residual vs fitted value graph in Minitab17 software was analyzed as shown in Figure 7.

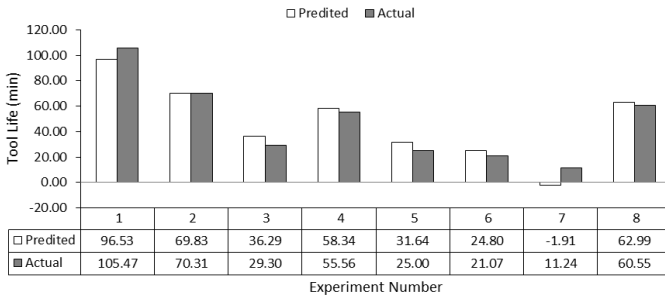


Figure 6: Comparison of actual vs predicted tool life

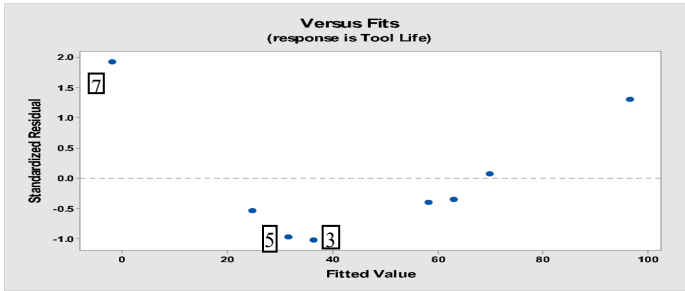


Figure 7: Residual vs fitted value graph before omitting outlier observation 7

Figure 7 shows the observation number 7 which appears to be an outlier in the fitted value graph. Its possible impact is directed by the realities of different perceptions at neighboring X-value. Observation number 3 and 5 then again, could well be the most impacted jointly. Being as one in its domain, it

may have real impact on the position of fitted model. It may have a major residual, contingent upon the fitted model and other remaining information. In any data set where the estimation of at least one parameter depends intensely on a little quantity of the observations, issues of interpretation can emerge. One approach to anticipate such issues is to check whether the cancellations of observations are extraordinarily influenced by the fit of the model and the resulting conclusion by Draper and Smith [34]. Thus, Figure 8 shows the residual vs fitted value graph tool life after omitting outlier observation 7.

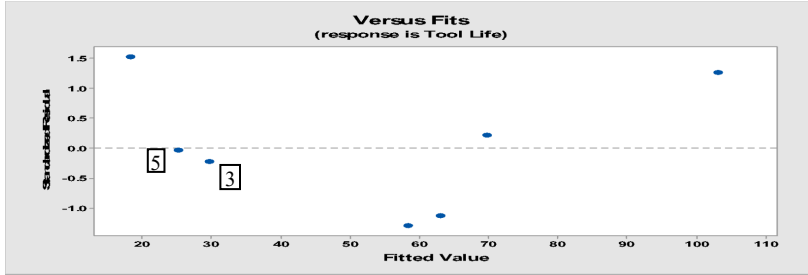


Figure 8: Residual vs fitted value graph tool life after omitting outlier observation 7

Based on the graph of Figure 8, it can be clearly shown by omitting the observation 7 that the line moves largely from 0 to 20, whereas for observations 3 and 5 the lines move from approximately 39 to 32 and 30 to 25 respectively. Therefore, after omitting observation 7, the graph fitted fairly. Table 6 shows the ANOVA table for tool life after omitting outlier observation 7 and the interpretation of the model is as follows:

Table 6: ANOVA table for tool life after omitting outlier observation 7

Source	Seq SS	DF	Adj SS	Adj MS	F-value	P-value
Regression	5451.73	3	5451.73	1817.24	196.27	0.001
Cutting speed	1814.15	1	3205.89	3205.89	346.26	0.000
Feed rate	1866.29	1	2575.06	2575.06	278.12	0.000
Radial Depth	1771.29	1	1771.29	771.29	191.31	0.001
Error	27.78	3	27.78926			
Total	5479.51	6				

Based on Table 6, it can be seen that without observation 7, the resulting ANOVA analysis of tool life showed no interaction among cutting speed, feed rate and radial depth towards generating the tool life machining response. The cutting speed is the most significant machining factor affecting tool life followed by feed rate and radial depth of cut. It was proven with the generated

lowest P-value of 0.000 and the largest F-value of 346.26. Thus, it was shown that the model was perfectly fair.

The outlier occurred due to the application of the higher cutting parameters for this experiment, which were cutting speed at 350 m/min, feed rate at 0.04 mm/tooth and radial depth at 25 mm. Thus, the movement of the cutting tool became faster and increased the temperature in the cutting area, which caused an increment in wear rate and plastic deformation at the edge of the cutting tool [35]. Therefore flank wear was the main issue in the face milling of A390 Al-Si alloy with DLC coated cutting tool insert. Figure 9 shows the SEM images of a worn out view on the flank face for DLC coated carbide insert.

It can be seen that chipping was the main cause of tool failure when the VB value reached 0.3 mm. This type of failure is caused by variable shock loads of intermittent cut and built up edge which welded to the worn area of the insert. Furthermore, high temperature and extreme force during the cutting process can cause stress that leads to the development of plastic deformation around the rake face and nose radius. This finding indicates that for machining of A390 Al-Si alloy, the DLC cutting tool had the least abrasive resistance when machining under dry conditions, thus resulting in rapid tool failure.

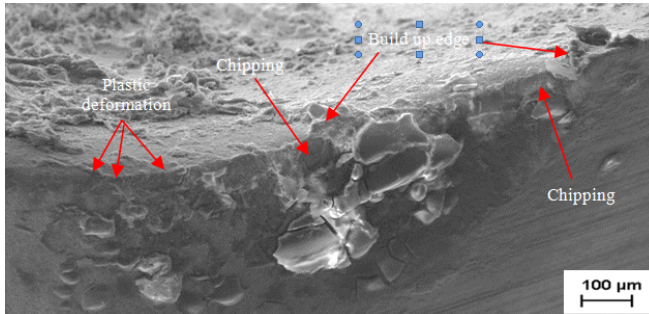


Figure 9: SEM images of a worn out view on the flank face for DLC coated carbide insert at cutting speed 350 m/min, feed rate 0.04 mm/tooth and radial depth 25 mm in dry cutting condition.

A prediction modelling of tool life, after reanalyzing, was generated by adapting multiple regression analyses on the experimental data. Equation 3 represents the empirical relationship in the context of actual factors:

$$\text{Tool life} = 288.40 - 0.4476 \text{ Cutting Speed} - 2006 \text{ Feed} 2.662 \text{ Radial depth of cut} \quad (3)$$

A graphical comparison between the actual experimental data and predicted tool life after omission of outlier observation 7 was constructed as shown in Figure 10. This relative percentage rate errors recorded for the connection between the actual and predicted values were from 0.27% to 13.53%. It was an acceptable percentage error as it was below 20% [36]. Hence, the general trend in tool life variation appears to be well described by the prediction models.

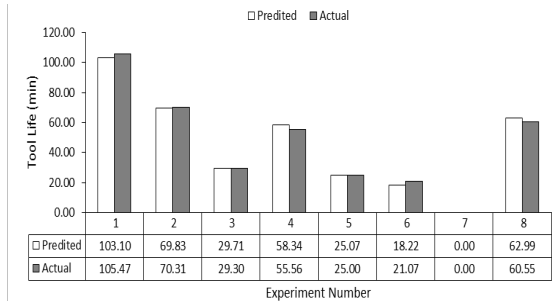


Figure 10: Actual vs predicted tool life after omitting outlier observation 7

Main Effect Plot Tool Life

Figure 11 shows the main effect plot values obtained after omitting outlier data. It can be observed that by decreasing the cutting speed, feed rate, and radial depth, the mean tool life value increases.



Figure 11: Main Effect Plot of tool life after omitting outlier data

According to the theory of the main effect plot, tool life is significantly affected by the cutting speed and feed rate. Also, the cutting speed slope and line exceeds the feed rate, confirming that cutting speed has the strongest effect as the machining factor most influencing tool life. Furthermore, the interpretation of generating tool life is made on the maximum value of mean tool life at each cutting factor. Therefore, the selected machining parameters

for achieving longer tool life are at 250 m/min cutting speed, 0.02 mm/tooth feed rate and 12.5 mm radial depth.

Conclusion

This study was conducted to determine the optimized machining parameters and to find the most significant machining factor influencing the machining response under dry cutting condition for milling of Aluminum Alloy A390. Surface roughness and tool life under dry milling condition were evaluated and analyzed. Based on the experimental data and analysis of results, conclusions can be drawn as follows:

- By applying the selected machining parameters used in this study, the lowest surface roughness of 0.140 μm and the longest tool life of 105.47 minutes could be realized when milling A390 Al-Si alloy.
- ANOVA analyses revealed that the most significant machining factor affecting Ra is the feed rate, proven with at F-value of 201.10, while the machining factor that is most influential towards tool life is the cutting speed at F-value of 346.26 after omitting outlier data.
- By using the main effect plot, the optimum machining parameters for achieving lower Ra and longer tool life is at 250 m/min cutting speed, 0.02 mm/tooth feed rate and 12.5 mm radial depth.
- There are no interaction effects on machining parameters for both of surface roughness and tool life results. The interaction effects are negligible for minimizing surface roughness and maximizing tool life.
- The predicted model reported results which were almost similar to its experimental counterpart, with percentage errors of between 0.53% to 1.42% and 0.68% to 13.53% for surface roughness and tool life respectively, after omitting outlier data from design analysis. The percentage errors were deemed acceptable as they were below 20%.

Future Research

Analysis of the results obtained from the current work suggests several feasible extensions to the research. Some of these have been listed below:

- Different coated cutting tools can be used on A390 Al-Si alloys for dry cutting. Additionally, the cutting parameters can be optimized.
- Material removal rate and tool flank wear can also be taken as responses in addition to tool life and surface roughness.
- The used of cryogenic machining may further enhance the tool life and surface roughness.

References

- [1] L.Lasa, J.M. Rodriguez-Ibab, *Mater Sci. Eng. A.*, 363-193, 2003.
- [2] M. Javidani and D. Larouche, "Application of cast Al-Si alloys in internal combustion engine components," Article in *International material reviews* (2014).
- [3] A.M. Khorasani, M.R.S. Yazdi & M.S. Safizadeh, "Tool Life Prediction in Face Milling Machining of 7075 Al by Using Artificial Neural Networks (ANN) and Taguchi Design of Experiment (DOE)," *International Journal of Engineering and Technology* 3(1), 30 (2011).
- [4] B. Dhanasekar and B. Ramamoorthy, "Restoration of blurred images for surface roughness evaluation using machine vision," *Tribology International* 4, 3268–276 (2010).
- [5] A. Hamdan & A.D. Ahmed, Sarhan & M. Hamdi, "An optimization method of the machining parameters in high-speed machining of stainless steel using coated carbide tool for best surface finish," *International Journal Advanced Manufacturing Technology* 58, 81–91 (2012).
- [6] N. Qehaja, K. Jakupi, A. Bunjaku, M. Bruçi, & H. Osmani, "Effect of machining parameters and machining time on surface roughness in dry turning process," *Procedia Engineering* 100, 135-140 (2015).
- [7] G.C. Onwubolu, "A note on surface roughness prediction model in machining of carbon steel by PVD coated cutting tools," *American Journal of Applied Sciences* 2(6), 1109-1112 (2005).
- [8] C. J. Rao, D. Sreeramulu & A.T. Mathew, "Analysis of tool life during turning operation by determining optimal process parameters," *Procedia Engineering* 97, 241-250 (2014).
- [9] J.F. Kelly & M.G. Cotterell, "Minimal lubrication machining of aluminium alloys," *Journal of Materials Processing Technology* 120(1–3), 327–334 (2002).
- [10] G. Chirita, "Influence of vibration on the solidification behavior and tensile properties of an Al–Si 18% alloy," *Materials and Design*, 1575–1580 (2009).
- [11] T. Erry Yulian & Adesta, "Tool Wear and Surface Finish Investigation in High Speed Turning Using Cermet Insert by Applying Negative Rake Angles," *European Journal of Scientific Research* 38, 180-188 (2009).
- [12] V. Petzoldt, "Drehen und Fräsen SiC-partikelverstärkter Al-Legierungen, In *Spanende Fertigung*," Prozesse, Innovationen, Werkstoffe Hrsg., Weinert K. Essen: Vulkan Verl., 383-391 (2000).
- [13] M.S. Carrilero, R. Bienvenido, J.M. Sanchez, M. Alvarez, A. Gonzalez, M. Marcos," *Int. J. Mach. Tools Manuf.* 42, 215 (2002).
- [14] T.C.S. Vandervelde, K. Vandirondonck, M. Van Stappen, W. Du Mong, P. Perremans, *Surf., Coat., Technol.* 113, 80 (1999).

- [15] T. Yokota, T. Sawa, M. Yokouchi, K. Tozawa, M. Anzai & T. Aizawa, "Frictional properties of diamond-like carbon coated tool in dry intermittent machining of aluminum alloy 5052," *Precis. Eng.* 38, 365–370 (2014).
- [16] G.S. Goindi & P. Sarkar, "Dry machining: A step towards sustainable machining—Challenges and future directions," *Journal of Cleaner Production* 165, 1557-1571 (2017).
- [17] F. Rabinovich, G. Dasch, J.M. Wagg, T. Yamamoto, K. Veldhuis, S.G.K. Dosbaeva, M. Tauhiduzzaman, "Cutting performance of different coatings during minimum quantity lubrication drilling of aluminum silicon B319 cast alloy," *Surf. Coat. Technol.* 205, 4107–4116 (2011).
- [18] P.S. Sreejith & B.K.A. Ngoi, "Dry machining: machining of the future," *J. Mater. Process. Technology* 101, 287–291 (2000).
- [19] H. Ni, M. Elmadagli, A.T. Alpas, "Mechanical properties and microstructures of 1100 aluminum subjected to dry machining," *Material science & Engineering* 385, 267-278 (2004).
- [20] A. Torres, I. Puertas & C.J. Luis, "Surface roughness analysis on the dry turning of an Al-Cu alloy," *Procedia Engineering* 132, 537-544 (2015).
- [21] E. Kuram & B. Ozelik, "Multi-objective optimization using Taguchi based grey relational analysis for micro-milling of Al 7075 material with ball nose end mill," *Measurement* 46(6), 1849-1864 (2013).
- [22] S. K. Pattnaik, N. K. Bhoi, S. Padhi, & S. K. Sarangi, "Dry machining of aluminum for proper selection of cutting tool: tool performance and tool wear," *The International Journal of Advanced Manufacturing Technology*, 1-11 (2017).
- [23] T. F. Ariff, M. F. Paimin & A. Hassan, "Dry machining of T6061 aluminium alloy using titanium nitride (TiN) and titanium carbonitride (TiCN) coated tools," *In Applied Mechanics and Materials* 284, 291-295 (2013).
- [24] G. Cha, J. Li, S. Xiong & Z. Han, "Fracture behaviors of A390 aluminum cylinder liner alloys under static loading," *Journal of Alloys and Compounds* 550, 370-379 (2013).
- [25] P. J. Ross, "Taguchi Techniques for Quality Engineering," New York: McGraw-Hill Book Company, 1996.
- [26] A. H. Suhail, N. Ismail, S.V. Wong & N. A. Jalil, "Optimization of cutting parameters based on surface roughness and assistance of workpiece surface temperature in turning process," *American journal of engineering and applied sciences* 3(1), 102-108 (2010).
- [27] Z. Hessainia, A. Belbah, M.A. Yallese, T. Mabrouki & J.F. Rigal, "On the prediction of surface roughness in the hard turning based on cutting parameters and tool vibrations," *Measurement* 46(5), 1671-1681 (2013).
- [28] K. Bouacha, M. A. Yallese, T. Mabrouki, & J. F. Rigal, "Statistical analysis of surface roughness and cutting forces using response surface

- methodology in hard turning of AISI 52100 bearing steel with CBN tool,” *International Journal of Refractory Metals and Hard Materials* 28(3), 349-361 (2010).
- [29] M. Ramanathan, P. Thanish & R. R. Raja, “Performance Evaluation of PCD Insert 1600 Grade on Turning of Al 6061 Reinforced with 7.5% ZrB₂ Metal Matrix Composite,” *EDP Science* (2016).
- [30] J. Simao, H. G. Lee, D. K. Aspinwall, R. C. Dewes, & E. M. Aspinwall, “Workpiece surface modification using electrical discharge machining,” *International Journal of Machine Tools and Manufacture* 43(2), 121-128 (2003).
- [31] M. Kök, “Tool life modeling for evaluating the effects of cutting speed and reinforcements on the machining of particle reinforced metal matrix composites,” *International Journal of Minerals, Metallurgy, and Materials* 17(3), 353-362 (2010).
- [32] S. J. Ojolo & O. Ogunkomaiya, “A study of effects of machining parameters on tool life,” *International Journal of Materials Science and Applications* 3(5), 183-199 (2014).
- [33] A. Li, J. Zhao, D. Wang, J. Zhao & Y. Dong, “Failure mechanisms of a PCD tool in high-speed face milling of Ti–6Al–4V alloy,” *The International Journal of Advanced Manufacturing Technology*, 1-8 (2013).
- [34] N. R. Draper & H. Smith, “*Applied Regression Analysis*,” Third Edition, John Wiley & Sons (1998).
- [35] S. Thamizhmanii, S. Hasan & E. Natarajan, “Performance of Tool Wear Using Cryogenic Treated CBN Inserts,” *Proceedings of the World Congress on Engineering, Vol II, July 5-7, London, U.K.* (2017).
- [36] E.O. Ezugwu, S.J. Arthur, E.L. Hines, “Tool-wear prediction using artificial neural networks,” *Journal of Materials Processing Technology* 49, 255-264 (1995).

3D Model of Bone Scaffolds Based on the Mechanical Behaviour for a Hybrid Nano Bio-composites

Jenan, S. Kashan, Saad M. Ali*

University of Technology – Iraq, Biomedical Engineering Department

*30249@uotechnology.edu.iq

ABSTRACT

Ceramic/polymer Nano composites in the view of possessing design uniqueness and property combinations have gained a great attention and reported to be the materials of the 21st century that are not found in conventional composites. In the present work, an attempt has been made to study, develop and improve the bio-mechanic for a designed and fabricated Ceramic/polymer bio-composite for a human natural bone repair and replacement in the case of complex fracture and bone diseases by adding the Nano fillers ceramic particles to the Polymer Matrix Nano composites (PMNC) for fabricated a hybrid Titanium dioxide and yttria stabilized zirconia reinforced high density polyethylene (HDPE) matrix bio-composites properties. These bioactive composites have been investigated by using hot pressing technique at different compression pressures of (30, 60, and 90 MPa) at a compounding temperature of (180, 190, and 200 °C). The SOLIDWORKS 17.0 and the finite element ANSYS 15.7 software programs were used to the simulation, modelling and analysing of femur bone biomechanics that can withstand the highest stresses and strains. The response surface methodology (RSM) technique was used to improve and verify the results. For all the fabricated Nano bio-composites systems, the results showed that the obtained output parameters values were increased with increasing the process input parameters, also the vice versa for the strain energy and equivalent elastic strain values, also the Nano ceramic compositions represented the main factor influenced the results. The main investigates results of the current research deduced that for the increase of the Nano ceramic powder (TiO_2) contain from 1% to 10%, the compression fracture strength and the micro-Vickers hardness values increased by 50% and by 8.45%, respectively, and when adding 2% of zirconia (ZrO_2), an additional increase in the compression fracture strength and micro hardness by 28.21% and 40.19% achieved, respectively. When using 10% TiO_2 + 2% ZrO_2 /HDPE bio-composite at highest compact

temperature of 200 °C and compounding pressure of 90 MPa, the strain energy and the equivalent elastic strain reduced by 82.69% and 14.53% when compared with using of 1% TiO₂ content. While when increasing the nano ceramic content from 1% to 10% without adding the ZrO₂ nano filler, they reduced by 142.25% and 67.81%, respectively. The maximum equivalent von Misses stress obtained is equal to 39.957MPa and when increasing the nano ceramic content from 1% to 10%, the stress safety factors and fatigue live values increased by 58.38% and by 46.28%, respectively and when adding 2% of zirconia (ZrO₂), the stress safety factor reached its maximum values, with an additional increase in its values by 21.42% and 69.40%, respectively. These results give great choices to use successful in vivo tests and for a better life performance with any age, patient status and degree of injury.

Keywords: Nano ceramic Bio-composites; ANSYS Femur bone modelling; Fatigue life; Finite element analysis; Bone biomechanics;

Introduction

Bone is a living material with a complex hierarchical structure [1]. Bone fracture is a multi-scale susceptibility problem related to musculoskeletal loading, tissue properties, bone metabolism and other factors, such as material properties variations, bone loss and microstructure changes etc. [2-3]. Bone, as a composite, has a complex micro structural feature which has been a major challenge in mimicking its load-bearing performance [4]. For the future of osseous defects therapies, the Scaffold-based bone tissue engineering holds great promise.

Bone tissue engineering applies scientific principles to regenerate, repair, and restore the functions of defected hard tissues [5]. Four classes scaffolds materials can be categorized: polymeric, ceramic, composite, and metallic scaffolds [6-7]. The development and use of polymeric nano composites advanced materials in recent years have been expanded exponentially. In order to design polymeric nano composites in an efficient and safe manner, a substantial amount of research has been done [8].

In the past few years, the finite element analysis (FEA) has been increasingly adopted to study the mechanical behaviour of biological structures and the comparisons between the experimental testing results and those obtained from FEA and reveal a close correlation [9]. A number of researchers are interested in using the 3D finite element analysis (FEA) to investigate the effect of loading conditions on the stress and strain distribution within the osteoporotic human femur bone tissue, i.e. the mechanical strength in human bone [10-15].

Polymer nano composites have attracted increasing attentions in recent years because of their significant improvement in mechanical performance, thermal stability and electrical properties. They are materials of a new class, incorporating an ultrafine dispersion of nano materials in a polymeric matrix [16]. Inorganic nano particles such as Zirconium dioxide (ZrO_2), titanium dioxide (TiO_2) and synthesized hydroxyapatite (HAP) have been used as Nano fillers in composites to improve the polymer properties [17-18].

In the latest past, TiO_2 -filled polymers fabricated by melt compounding have been reported to improve the properties over a micron-sized particle-filled polymer composite. It was found that the addition of TiO_2 increased the impact and tensile strength of the polyethylene [8, 16]. High density polyethylene (HDPE) is a thermoplastic material, as a matrix component of bone implants, and has shown a great promise. Its structure consists of long chains of carbon and hydrogen atoms bonded with a variable branching, which determines its mechanical properties [8]. HDPE polymer has been proposed by Bonfield et. al, since the early 1980s as a matrix in HA/HDPE composite for bone repair application because of its optimum combination of mechanical, considerable bioactivity and biological performance which is closed to the bone structure [19-21]. It is used to obtain a high strength-to-density ratio. It is converted into ethylene from methane gas and then into polyethylene with the application of heat and pressure. It should be processed into porous scaffolds with high moldability and exhibits mechanical properties similar to those of the native bone and does not produce any toxins that hinder osteogenesis integration [22].

By adding small percentages of Yttrium oxide, also known as yttria (Y_2O_3), which is an air-stable and a very hard ceramic, the phase changes are eliminated, and the resulting material has superior thermal, mechanical, and electrical properties to produce yttria-stabilized zirconia (YSZ) or partially stabilized zirconia (PSZ). These oxides are commonly called "zirconia" (ZrO_2) and "yttria" (Y_2O_3), with a stable structure at the room temperature. YSZ has a number of applications for its hardness and chemical inertness, like tooth crowns, refractories, insulation, abrasives, electro-ceramics, jewellery, etc. [22].

The main aim of this work is to investigate the influence of adding titanium dioxide and partial stabilized zirconia (PSZ) nano ceramic fillers powders with different concentrations at different compression pressures and temperatures using the hot pressing fabricating technique on the mechanical properties for TiO_2 / HDPE and Y_2O_3 - partial stabilized zirconia (Y-PSZ)/ TiO_2 / HDPE nano composites polymer matrices systems and to investigate the longest fabricated biomaterials fatigue lives and the highest stress factors of safety to withstand the loads of the daily human activities. The femur bone 3D geometry was created by using the SOLIDWORKS 17.0, analysed and modelled by using finite element ANSYS 15.0 software program. For improving and verifying the results, reaching and evaluating the optimal

thermal and mechanical properties, the response surface methodology (RSM) technique and the Design Expert software program were used.

Materials and Methods

Nano composites Preparation method

Six nano composites systems; TiO₂/ HDPE and Y₂O₃- partial stabilized zirconia (Y-PSZ)/ TiO₂/ HDPE were prepared, fabricated and used in this study as bioactive material to be used as bone grafting bio-composite materials. The two types of ceramic filler were used; the titanium dioxide (TiO₂) of 99% purity with an average particle size of 40 nm and a particle density of 4.23 g/cm³ supplied by M.K Nano (Canada, Toronto) and the partially-stabilized zirconia (ZrO₂-PSZ) which was doped with 3 mol. % of yttria (Y₂O₃). The Y-PSZ nano powder of 99.9% purity with an average particle size of 40 nm and density of 5.91 g/cm³ was supplied by M.K. Nano (Canada, Toronto). The used biomaterial powder matrix was the high-density polyethylene (HDPE) with particle size of 5 μm and a density of 0.95 gm/cm³, supplied by Right Fortune Industrial Limited (China, Shanghai).

In this work, three groups of experiments were prepared using concentration contents of titanium dioxide ceramic filler as 1, 5 and 10% TiO₂, without use of Y₂O₃- partial stabilized zirconia (Y-PSZ). Other three groups of experiments were also prepared using the same concentration contents of titanium dioxide ceramic filler as 1, 5 and 10% TiO₂, but with the use of 2 % PSZ.

The prepared powders were first dry mixed with the each desired composition in a ball mill machine for 12 hr and then hot pressed at 180, 190, and 200 °C at a compounding pressure of 30, 60, and 90 MPa, respectively to obtain cylindrical shaped test samples with 10 mm diameter and a height varying between 3 and 5 mm. Figure 1 shows the fabricated hot-pressed system installed on the Instron testing machine, where the diametrical compression test was used to measure the fracture strength. This test is used for simple geometry and loading conditions like “dog bone” shaped specimens, which are too difficult to process or machine into the ASTM standard [23].



Figure 1: The fabricated hot pressed systems (1), installed on the Instron testing machine (2); thermostats (3) connected to the digital temperature control system (4)

Modelling and Analysis of Femur bone

It is difficult to assign the material properties along each direction of human bone model as it is solid, inflexible and highly heterogeneous and nonlinear in nature [10]. The human femur bone 3D geometry was modeled as a static problem by using the 3D Solid works 17.0 software and analyzed using the finite element module ANSYS WORKBENCH® 15.7 Multiphysics software, as shown in Figure 2a.

The bone material was assumed as homogeneous, isotropic and perfectly elastic [11]. The femur bone model was implemented by two components, namely the spongy cancellous (trabecular) covered by a thin layer of compact trabecular bone as illustrated in Figure 2b.

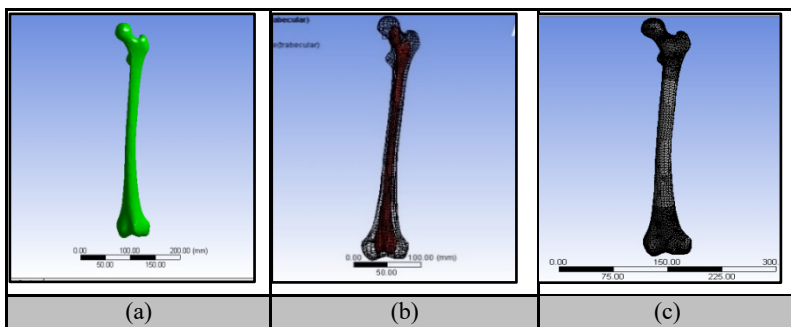


Figure 2: Modeling of femur bone; (a) human femur bone 3D geometry; (b) the natural inner trabecular and outer cortical bone parts; (c) the FEA meshing refinement of the natural bone

Boundary Conditions

The 3D Finite element method (FEM) was used to find the numerical solution and to simulate the stress distribution for a different loading conditions model of the implant femur bone [24-26]. Finite element modelling is an important tool for stress analysis of bones as a key to assessment of fracture risk, understand bone remodelling, and to the designing of fracture fixation [27-28].

The meshing process was imported in ANSYS with triangle surface, 3 degrees of freedom meshed elements as presented in Figure 2c. The number of nodes and elements for the model was about 39893 and 19419, respectively. The boundary conditions with the field equations govern the deformation and stress fields for the femur bone.

To simulate the stress and strain fields corresponding to the patient activities, two types of boundary conditions imposed. The elastic modulus of trabecular bone is 20–30% lower than the modulus of elasticity cortical bone [2, 11, 26]. The natural femur bone composed of two components of tissues: cortical (compact dense and hard tissue) and cancellous (trabecular) bone (cellular spongy tissue), which differ in their apparent density threshold and behavior [9, 15, 25-26, 30]. The femur bone material properties for an adult human are given in Table 1 [1, 10-12, 26, 30-33].

Table 1: The femur bone material properties for an adult human

It. no.	Material property	Value
1.	Density (gm/cm ³)	1.75
2.	Young's modulus (Gpa):	
	for cortical bone	17.0
	for trabecular bone	0.8
	for total femur bone	16.7
3.	Ultimate tensile strength (Mpa)	43.5
4.	Ultimate compressive strength (Mpa)	115.3
5.	Poisson's ratio for both bone layers	0.3

The concentrated and eccentric external loads (due to influence of eccentricity between the stem and femur head) were applied at the head of the bone to simulate the static and dynamic forces acting corresponding to periodic cycles of patient's activities with 70 kg body patient weight. The femur bone head-implant systems were loaded with 700 N axial, 100 N lateral loads and a torsional moment of 10.0 Nm. At the lower medial condyle and patellar surface, a fixed support is provided and the displacement is restricted in the all direction [11-13, 26].

During the walking and running conditions, the biomechanical characteristics of femur bone have an associated laterality movement and the

horizontal load components had a significant effect on the lubrication film of the head bone joint [10-12]. The boundary conditions model for the femur bone in ANSYS 15.0 is shown in Figure 3.

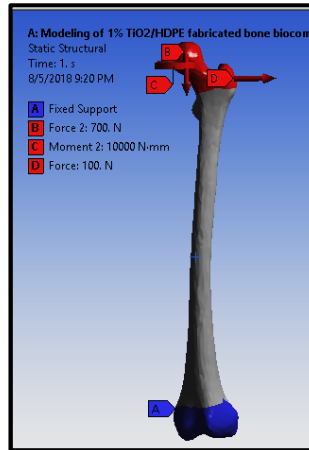


Figure 3: The boundary conditions model for the femur bone in ANSYS 15.0

Mathematical Modeling

The determination of the mechanical stresses in human bones that induce physiological activities is of great importance in both clinical and research practice [9]. Stress distribution is the important tool to indicate the crack or failure of the total femur bone arthroplasty which is affected by static and dynamic loads. Both the static load analysis applied due to the weight of the body and the dynamic load analysis applied due to walking cycle have been described in this study [32].

The effects of different biomechanical loading are investigated using a system of nonlinear differential equations [12]. The 3D mathematical model due to the loading caused by patient activities is constructed to analyze the stress field in the artificial bone component. From the continuum mechanics principles, the field equations governing the stress fields in the bone include the stress equilibrium equations, the geometric equation and constitutive equations [12, 33]. To solve the problem boundary value, the finite element analysis (FEA) is used.

High Cycle's Fatigue Analysis

Fracture and fatigue behavior is a time-related scenario may form and grow in the femur bone as a result of daily loading activities. The bone fatigue eventually reduces the load-carrying capability from the bone, leading to increase the stress redistribution within the bone structure [34]. To avoid and

localized progressive damage caused by daily cyclic loading as a result of walking, the femoral implant bone prosthesis was designed against the high cycles infinite fatigue fracture using the Soderberg's criterion as fatigue failure theory [14]. By using finite element analysis (as a cost efficient and computing time saving method in the biomedical engineering), the mean and alternative stresses are obtained to determine the design fatigue safety factor (SF) and to estimate the fatigue life until the failure of the prosthesis, i.e. the useful life of the prosthesis [32].

During its lifetime, bone is able to adapt its internal microstructure and varying physiological and mechanical environments in bone remodeling process. To predict such remodeling process, a number of biomechanical theories and algorithms have been proposed. On its mixed mode, bones withstand the repeated loadings (tensile, compression and shear) in daily activities [33].

The human body bones, as a structure, gradually turn into engineering material fatigue. In the past decades, the researchers reported that the bone damage caused by bone fractures and related diseases. In the modern bone biomechanics, fatigue and fracture form and grow due to that the accumulation of the bone damage is superior to the bone repairing ability. As a result, the study of the bone damage and fatigue became an important branch in clinical medicine and biomechanics [33].

Results and Discussions

This study attempted to create a bone simulation model that can withstand the highest stresses and strains producing during daily activities for prepared and fabricated nano composites for bones repairs. The maximum equivalent von-Mises stress obtained from the experimental tests, which have been introduced in the engineering date of the ANSYS 15.7 and the application of FEA, is equal to 39.957, which represent the stresses resulting from the boundary conditions and the application of loads resulting from daily activities on the human femur bone.

The location of these maximum equivalent von -Mises stresses, as expected, is in the middle portion where the bone has the less cross-sectional area where the fractures are confirmed by most cases in various incidents. The distribution of these stresses was shown in Figure 4. The obtained maximum equivalent von-Mises stress value was higher than the withstand values of daily human activity loads in a previous study by 53.68% [15].

The experiments in the present work were designed by using the full factorial method (FFM) and the response surface methodology (RSM). The analysis of variance (ANOVA) technique was used to analyze the results.

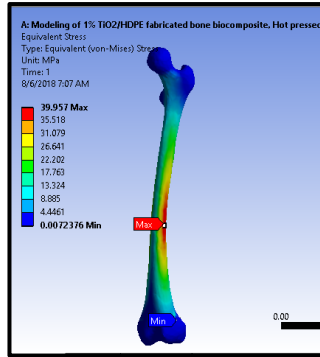


Figure 4: The Equivalent von–Misses Stress distribution

The three level factorial ANOVA analysis using the quadratic design model was implemented for analyzing the effect of input parameters on the compression fracture strength resulting for all the fabricated nano biocomposites systems. The model F-value of 143.38 and the P-values less than 0.0500 implies that the model is significant.

The 3D graphs of the effect of input parameters on the compression fracture strength obtained values for all the fabricated nanobiocomposites systems are shown in Figure 5. These graphs depict that the compression fracture strengths values increased with increasing the process parameters, i.e. the nano ceramic powder (TiO_2), the compounding pressure and the hot pressed temperature. The nano ceramic powder compositions represented the main factor influencing the results. With the increase of the TiO_2 content from 1% to 10%, the compression fracture strength value increased from 26 to 39 MPa, i.e. by 50%.

The maximum compression fracture strength reached 50 MPa when using 10% titanium oxide nano ceramic powder (TiO_2) with 2% partial stabilized zirconia (Y-PSZ), a compounding pressure of 90 MPa and a hot pressed temperature of 200 °C. This value is higher than the case of using the same content ratio of titanium oxide but without adding of zirconia (ZrO_2) by 28.21%. These results are higher than those in the previous studies using 5% TiO_2 /HDPE nano composites for maximum ultimate strength by 90.11% [8] and by 51.52% for other previous study used 1% Mn filler/ TiO_2 dispersion in PE matrix [16].

The most important reasons for this increase in the compression fracture strength values of the produced nano composites are the high values of the ceramic nano filler materials added, and the most important properties that are density, elastic and shear modulus, tensile and compression strengths, hardness and fracture toughness.

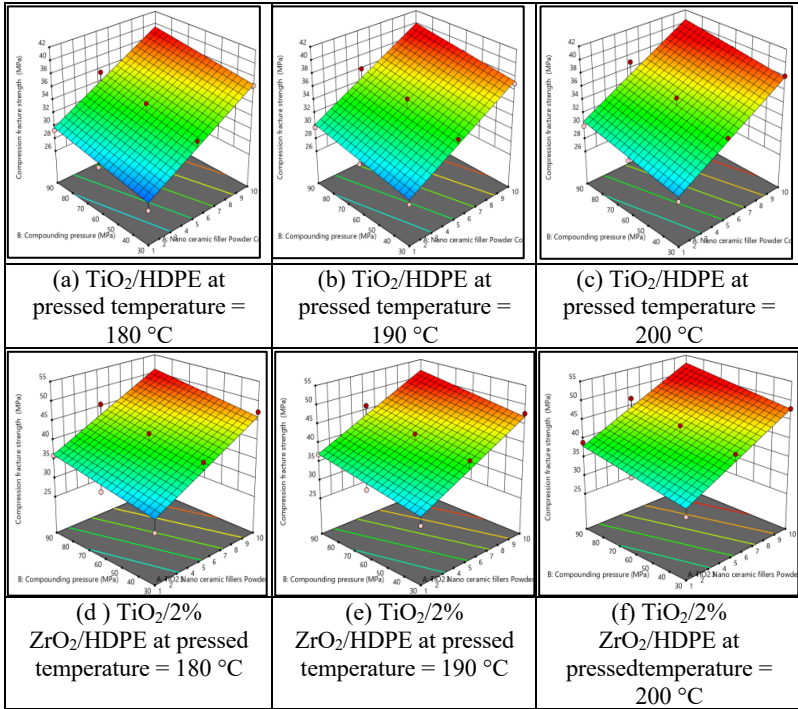
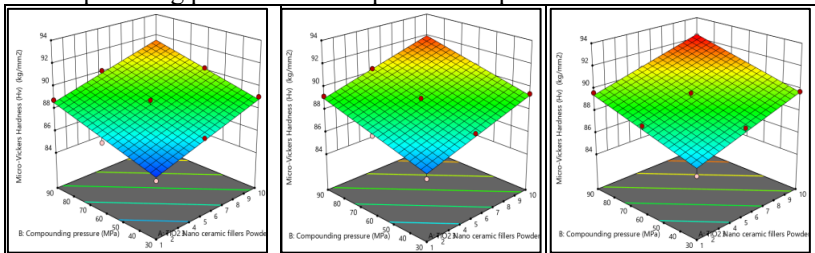


Figure 5: The 3D graphs for the effect of input parameters on the compression fracture strength for the fabricated nano bio-composites systems

The reasons of the enhancement in strength could be attributed to the excellent bonding between the nano ceramic particles with HDPE polymer matrix interface. The effect of input parameters on the micro-Vickers hardness (H_v) for all the fabricated nano biocomposites systems are shown in the 3D graphs in Figure 6. These graphs manifest that the micro-Vickers hardness values were increased with increasing the ceramic powders contents as well as the compounding pressure and hot pressed temperature.



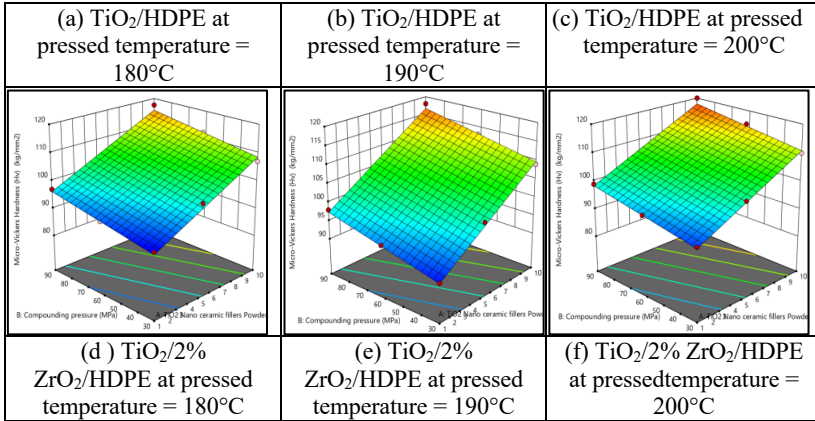


Figure 6: The 3D graphs for the effect of input parameters on micro Vickers hardness (H_v) for all the fabricated nano bio-composites systems

When increasing the nano ceramic content from 1% to 10%, the micro-Vickers hardness increased by 8.45% and when adding 2% of zirconia (ZrO₂), the micro-Vickers hardness reached its maximum values, i.e. an additional increase in microhardness by 40.19% was achieved. These hardness values are higher than the values obtained in a prior study using LDPE + 20% Al₂O₃ + 10% TiO₂ nano composites by 118.18% [35]. The increase in the micro hardness values of the fabricated nano composites hard tissues is attributing to the high physical and mechanical properties of the added ceramic nano filler materials and their high molecules cohesion with the HDPE matrix.

The daily human activities movements, i.e. the external mechanical work done, cause a femur bone structure elastic deformation that is transformed into internal strain energy. Figure 7 elucidates the effect of the input parameters for all the six fabricated nano composites systems on the strain energy, for different TiO₂ nano ceramic fillers powders compositions and best experimental results (90 MPa compounding pressure and 200°C hot pressed temperature) from each fabricated system, while the 3D graph in Figure 8 evinces the effect of these parameters on the strain energy values for all the fabricated nano composites systems.

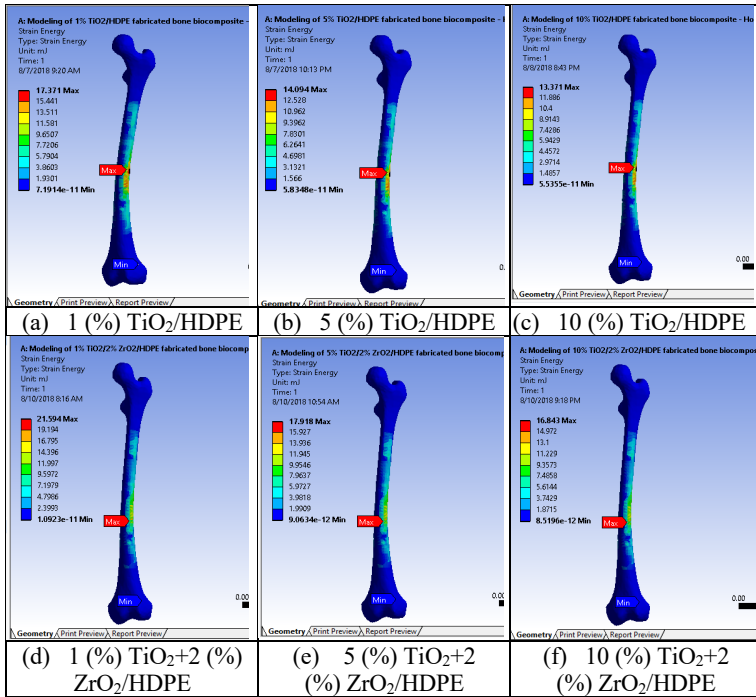


Figure 7: The effect of the input parameters on the strain energy values at 90 MPa compounding pressure and 200 °C hot pressed temperature

Figure 8 illustrates the 3D graphs for the effect of the input parameters on the strain energy values. It shows that the lower strain energy values obtained for these complex states of stress systems due to external loadings for the modeled femur bone with the best fabricated parameters using 10% TiO₂ + 2% ZrO₂/HDPE bio composite at highest compact temperature of 200 °C and compounding pressure of 90 MPa is equal to 16.843 m.J., i.e., the strain energy reduced by 82.69% when compared with the use of 1% TiO₂ + 2% ZrO₂/HDPE bio composite. While when increasing the nano ceramic content from 1% to 10% without adding the ZrO₂ nano filler, it reduced by 142.25%.

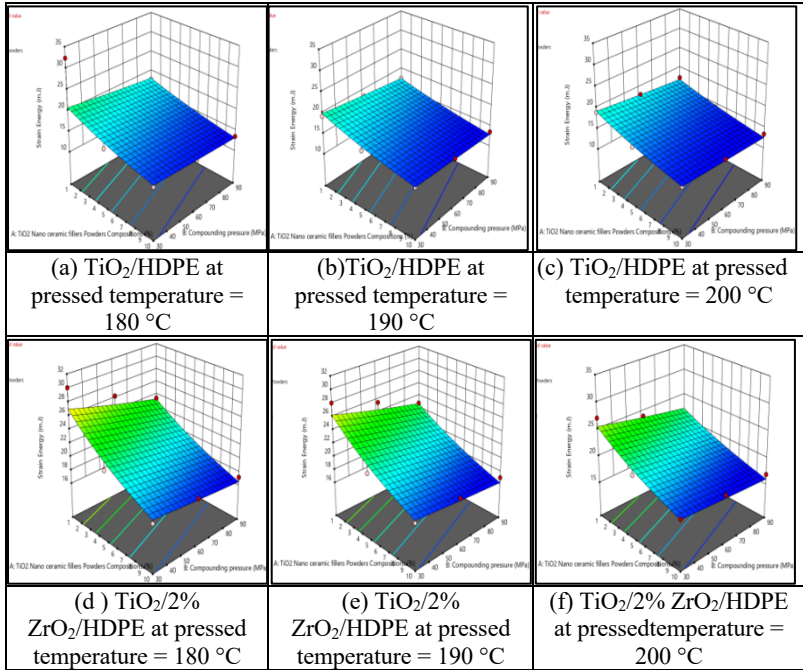


Figure 8: The 3D graphs for the effect of the input parameters on the strain energy values

In a previous study, the strain energy was found for the natural human femur bone equal to 15,61 m.J and for a fabricated bio composite material (20% vol. TiO₂/5% vol. Al₂O₃/PEEK) as 13,01 m. J. [36]. The results obtained for the all fabricated nano composites systems allow the designers to choose the appropriate biomaterial according to the clinical situation, age of the patient and the resulting static and dynamic loads dynamic when designing the material to repair the fractured bones due to the different types of accidents.

The effect of input parameters on the equivalent elastic strain values for all the fabricated nanobiocomposites systems are show in the Figure 9 and Figure 10. These graphs exhibit that the lowest equivalent elastic strain value was obtained with increasing the ceramic powders content as well as the compounding pressure and hot pressed temperature. When increasing the nano TiO₂ ceramic content to 10%, this value reached 0.0205 mm/mm, which is lower than when use the TiO₂ ceramic content of 1% by 67.81%.

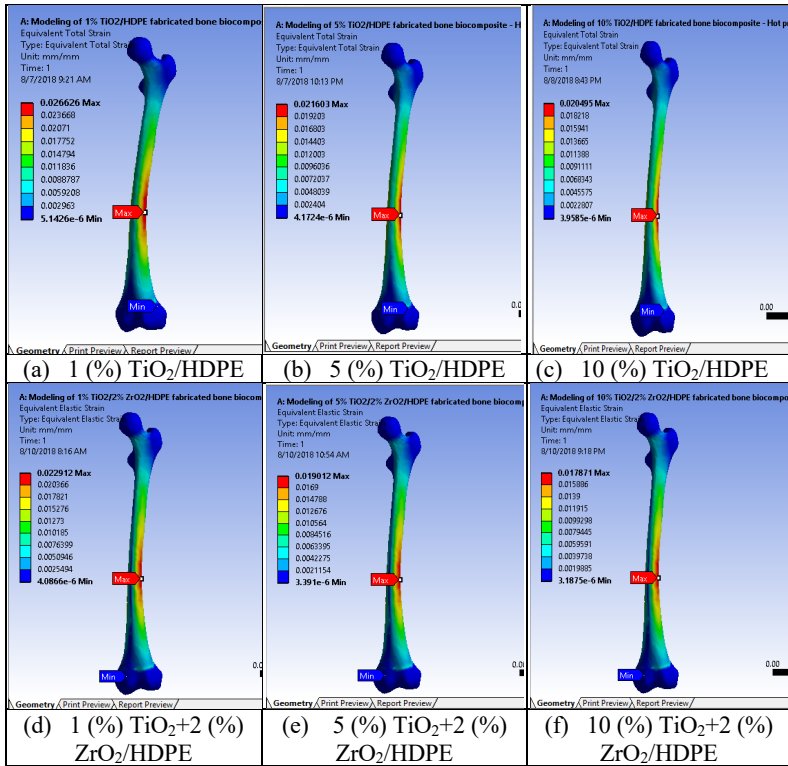
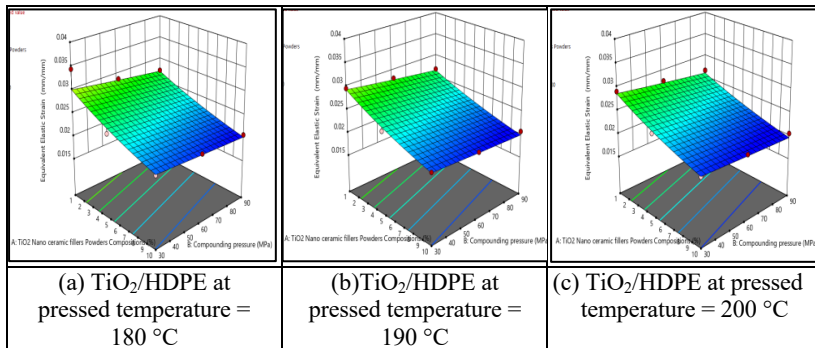


Figure 9: The effect of the input parameters on the equivalent elastic strain values for different TiO₂ nano ceramic fillers compositions at 90 MPa compounding pressure and 200 °C hot pressed temperature



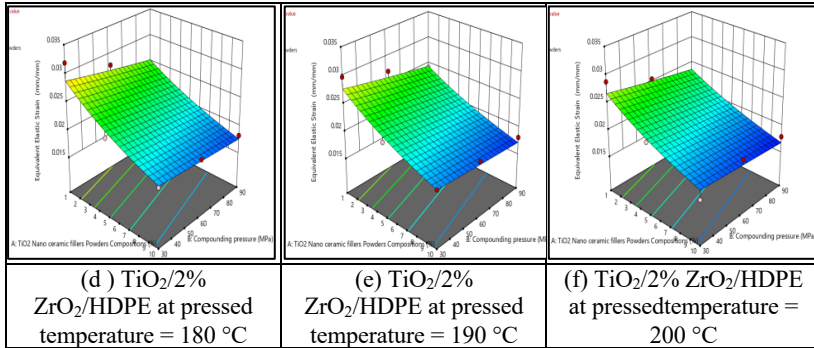


Figure 10: The 3D graphs for the effect of the input parameters on the equivalent elastic strain values

The equivalent elastic strain value reached reduced further in its value by 14.53% when adding 2% of zirconia (ZrO₂), the micro-Vickers hardness reached its maximum values, i.e. an additional increase in microhardness by 40.19% was achieved. These results are lower than those in the previous studies using 5% TiO₂/HDPE nano composites for equivalent elastic strain by 169.22% [8] and by more than 300% for another previous study [37].

This means that the nano particles fabricated in this study are the closest to the natural bone properties and therefore they excluded the new fractures because of the variation in the elongation rates due to different dynamic and static loads and this is one of the most important characteristics required in the replacement or bone grafting designs. The reduction in the equivalent elastic strain values of the fabricated nanocomposites is ascribed to the hard and brittle ceramic nano filler materials. That means these fabricated nano composites have the properties of lowest elongation and as those of the natural bones, and this achieves the objectives of using them in the clinical repair of bones operations. These low equivalent elastic strain values are of great importance in helping the patient to withstand higher external loads.

The 3D graphs in Figure 11 and Figure 12 display the effect of fabrication process input parameters on the stress safety factors for all the produced nano biocomposites systems. As demonstrated in these figures, the stress safety factors values were increased by increasing the ceramic filler content as well as the hot pressed temperature and the compounding pressure. Experimental results revealed that when increasing the nano ceramic content from 1% to 10%, the stress safety factors increased by 58.38% and when adding 2% of zirconia (ZrO₂), the stress safety factors reached its maximum value, with an additional increase in its value by 21.42%. The increase in the stress safety factor values can be returned to the addition of the high mechanical properties of the ceramic nano filler materials.

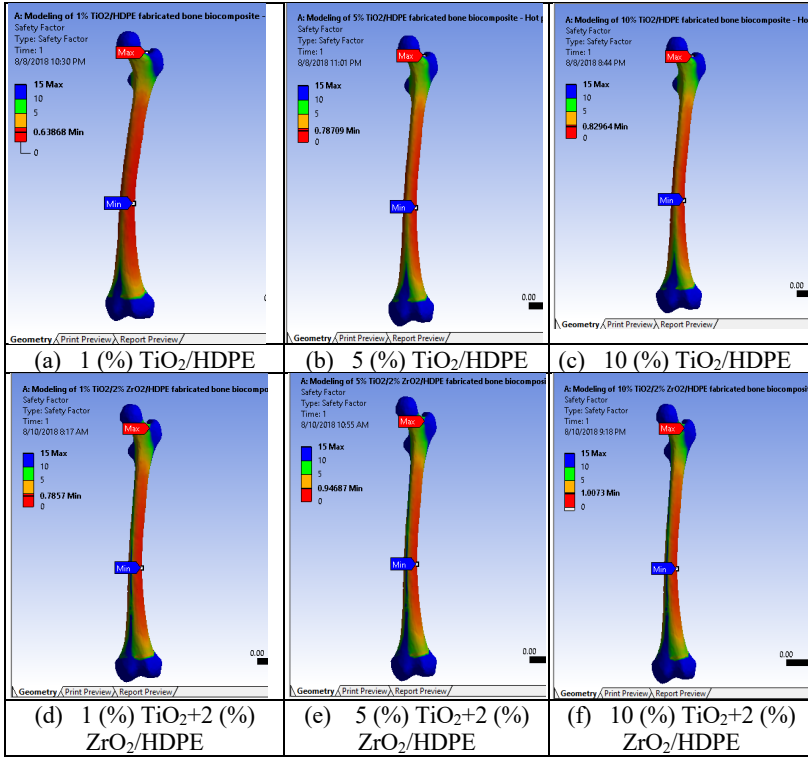
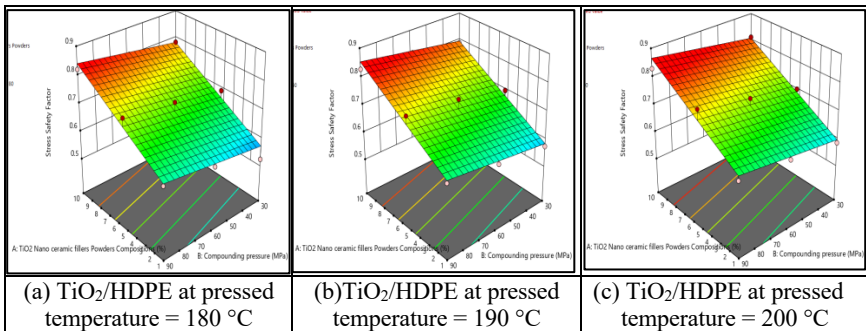


Figure 11: The effect of input parameters on the stress safety factors values at 90 MPa compounding pressure and 200 °C hot pressed temperature



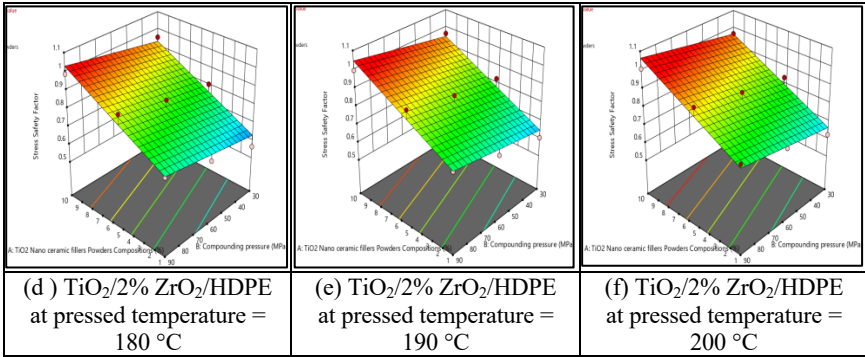
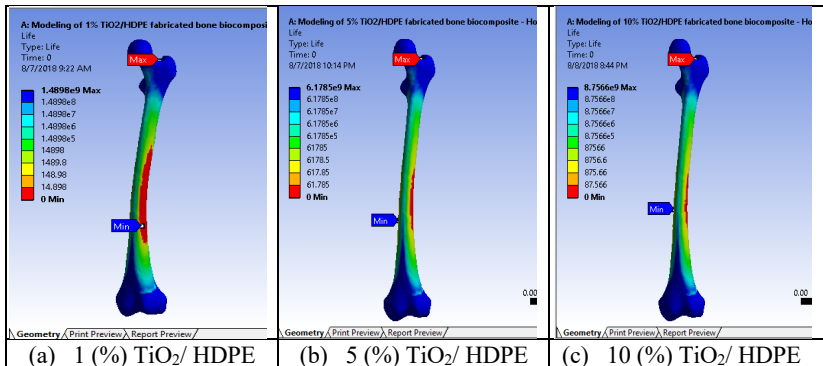


Figure 12: The 3D graphs for the effect of the input parameters on the stress safety factors values

The ANSYS analyses of the fatigue life values for the fabricated bio materials are given in Figure 13 and Figure 14, where the fatigue life values increased with increasing the compact temperature, the pressure and the nano filler content. The maximum fatigue livevalueof the modeled femur bone reached 4.3247×10^{10} cycles which is equivalent to actual service of the activity during normal movement of the patient after the operation for more than 28 years.

This value is the case of using 10% $\text{TiO}_2/2\% \text{ZrO}_2/\text{HDPE}$ nano composite and it is more than when using 1% $\text{TiO}_2/2\% \text{ZrO}_2/\text{HDPE}$ nano composite by 46.28% and more than if not using 2% ZrO_2 nano filler by 69.40. These results give a great freedom of choice to use the successful biocomposite substances in vivo tests with a good flexibility and a better life performance in line with the age, the patient status and the degree of injury.



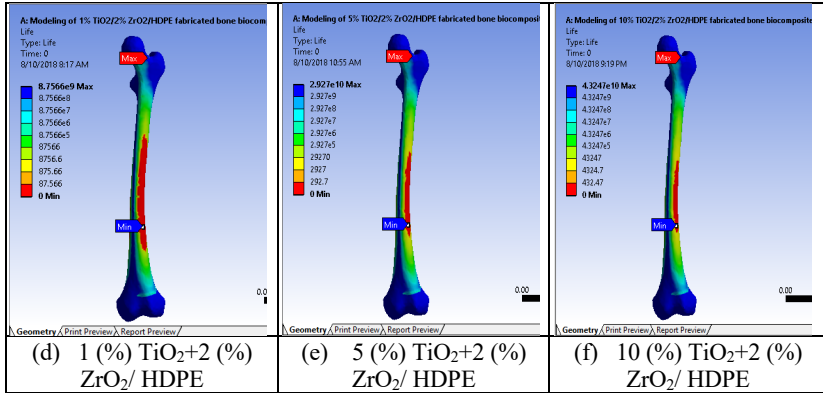


Figure 13: The effect of the input parameters on the fatigue life values at 90 MPa compounding pressure and 200 °C hot pressed temperature

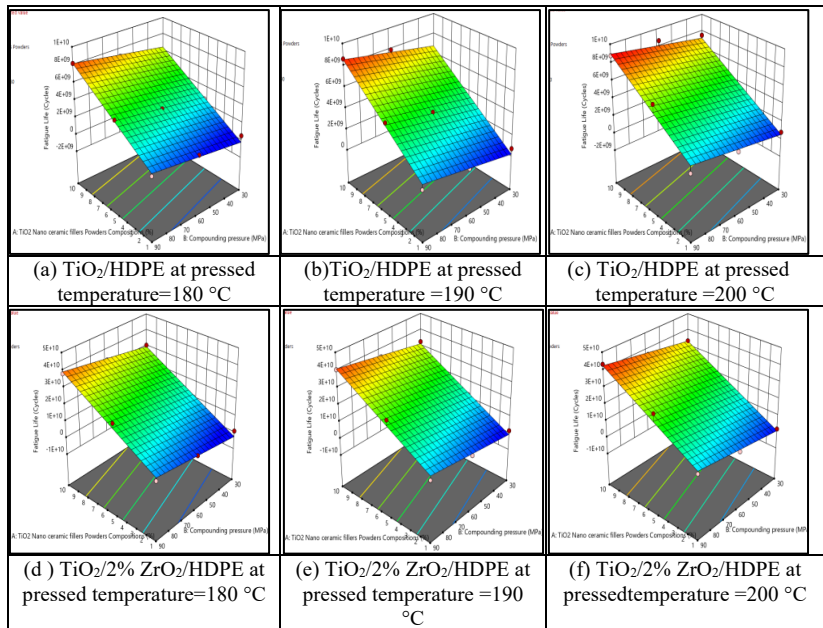


Figure 14: The 3D graphs for the effect of the input parameters on the fatigue life values

Conclusions

This study attempted to create a bone simulation model that can withstand the highest stresses and strains. All the results of experiments in the present work were designed by using the response surface methodology (RSM) and the analysis of variance (ANOVA) technique, and the P-values were less than 0.0500 implies that the models are significant. The following conclusions can be deduced from the results of the current research:

- 1) The results showed for all the fabricated nano bio-composites systems, that output performance parameters, including the compression fracture strengths, the micro-Vickers hardness (H_v), the stress safety factor and the fatigue lives values were increased by increasing the process input parameters, i.e. Nano ceramic powder (TiO_2), the adding of zirconia ceramic nano filler (ZrO_2), the compounding pressure and the hot pressed temperature. And the vice versa for the strain energy and equivalent elastic strain values, the nano ceramic powders compositions represented the main factor influencing the results.
- 2) With the increase of the TiO_2 contain from 1% to 10%, the compression fracture strength value increased by 50%. With adding of 2% partial stabilized zirconia (Y-PSZ), this value was increased by 28.21%.
- 3) When increasing the nano TiO_2 ceramic content from 1% to 10%, the micro-Vickers hardness increased by 8.45% and when adding 2% of zirconia (ZrO_2), an additional increase in micro hardness by 40.19% was achieved.
- 4) When using 10% TiO_2 + 2% ZrO_2 /HDPE bio composite at the highest compact temperature of 200 °C and a compounding pressure of 90 MPa, the strain energy reduced by 82.69 % when compared with the using of 1 % TiO_2 + 2 % ZrO_2 / HDPE bio composite. While, when increasing the nano ceramic content from 1% to 10% without adding the ZrO_2 nano filler, it reduced by 142.25%.
- 5) When increasing the nano TiO_2 ceramic content to 10%, the equivalent elastic strain value reached to 0.0205 mm/mm, which is lower than when using 1% TiO_2 ceramic content by 67.81%. The equivalent elastic strain values reduced further in its value by 14.53% when adding 2% of zirconia (ZrO_2).
- 6) The maximum equivalent von –Misses Stress obtained is equal to 39.957 MPa. Experimental results manifested that when increasing the nano ceramic content from 1% to 10%, the stress safety factors increase by 58.38% and when adding 2% of zirconia (ZrO_2), the stress safety factors reached its maximum value, with an additional increase in its value by 21.42%.
- 7) The maximum fatigue lives values of the modeled femur bone reached 4.3247×10^{10} cycles, which is equivalent to actual service of the activity during the normal movement of the patient after the operation for more

than 28 years. This value is the case when using 10% TiO₂/2% ZrO₂/HDPE nano composite and it is more than when using 1% TiO₂ content by 46.28% and more than if not used 2% ZrO₂ nano filler by 69.40.

The results obtained allow the biomedical engineering designers to choose the appropriate and the successful bio composite substances for in vivo tests and for a better life performance in line with the age, the patient degree of injury status, the clinical situation and therefore the required static and dynamic loads when designing a material to repair or replace the fractured bones partially or totally due to the different types of accidents.

References

- [1] M. E. Zagane, S. Benbarek, A. Sahli, B. Bachir and B. Serier, "Numerical simulation of the femur fracture under static loading", *Structural Engineering and Mechanics* 60 (3), 405-412 (2016).
- [2] C. Luca, T. Fulvia, B. Massimiliano, B. Fabio, S. Susanna and V. Marco, "Multiscale investigation of the functional properties of the human femur", *Phil. Trans. R. Soc. A* 366, 3319–3341 (2008).
- [3] A. A. Abdel-Wahab, A. R. Maligno, and V. V. Silberschmidt, "Micro-scale Modelling of Bovine Cortical Bone Fracture: Analysis of Crack Propagation and Microstructure Using X-FEM", *Computational Materials Science* 52, (1), 128 – 135 (2012).
- [4] S. Jenan Kashan and G. Huseein, "The Development of Biomimetic Nano CaCO₃/ PPBio Composites as Bone Repair Materials- Optimal Thermal Properties Evaluation", *Journal of Babylon University, Engineering Sciences* 25, (5), 1562-1571 (2017).
- [5] A. Adeel, "Implantable zirconia bioceramics for bone repair and replacement: A chronological review." *Mater. Express* 4 (1), 1-12 (2014).
- [6] G. Toktam, S. Azadeh, H. E. Mohammad, M. Alireza, M. Jebrael and M. Ali, "Current Concepts in Scaffolding for Bone Tissue Engineering", *The Archives of Bone and Joint Surgery* 6 (2), 90-99 (2018).
- [7] Sergey V. D., "Biocomposites and hybrid biomaterials based on calcium orthophosphates", *Biomater* 1 (1), 3-56 (2011).
- [8] I. M. Abdel-Hamid, S. M. Mohammad, M. Anusha, P. Hifsa and M. K. Uma, "On the Injection Molding Processing Parameters of HDPE-TiO₂ Nanocomposites," *Materials* 10 (85), 1-25 (2017).
- [9] C. C. Ahmet, U. Vahdet and K. Recep, "Three-Dimensional Anatomic Finite Element Modelling of Hemi-Arthroplasty of Human Hip Joint", *Trends Biomater. Artif. Organs* 21 (1), 63-72 (2007).

- [10] P. S. R. Senthil Maharaja, R. Maheswaranb and A. Vasanthanathan, “Numerical Analysis of Fractured Femur Bone with Prosthetic Bone Plates”, *Procedia Engineering* 64, 1242 – 1251 (2013).
- [11] I. Dmitry, B. Yuri and B. Anatoly, “A numerical comparative analysis of ChM and Fixion nails for diaphyseal femur fractures”, *Acta of Bioengineering and Biomechanics* 18 (3), 73-81 (2016).
- [12] S. Srimongkol, S. Rattanamongkonkul, A. Pakapongpun, D. Poltem, “Mathematical Modeling for Stress Distribution in Total Hip Arthroplasty”, *International Journal of Mathematical Models and methods in Applied Sciences* 6 (7), 885-892 (2012).
- [13] M. Aleksa, S. Aleksandar, C. Katarina, T. Uros and D. Branislav, “Numerical Analysis of Stress Distribution in Total Hip Replacement Implant”, *Integritet I VekKonstrukcija* 17 (2), 139–144 (2017).
- [14] A. K. Sajad, “The Fatigue Design of a Bone Preserving Hip Implant With Functionally Graded Cellular Material”, *Damiano Pasini Journal of Medical Devices* (7), 1-2 (2013).
- [15] T. Mohamed, R. Emmanuel, C. Patrick, H. Christian, P. Martine and W. M. Sylvie, “Numerical modeling of an osteoporotic femur: comparison before and after total hip prosthesis implantation”, *European Journal of Computational Mechanics* 17 (5,6,7), 785-793 (2008).
- [16] S. H. Abdul Kaleel and B. Ko. Bahuleyan, J. Masihullah, and Mamdouh A., “Thermal and Mechanical Properties of Polyethylene/ Doped-TiO₂ Nano composites Synthesized Using In Situ Polymerization”, *Journal of Nanomaterials*, 1-6 (2011).
- [17] H. Thomas and V. S. Dorothée, “Polymer-Nanoparticle Composites: From Synthesis to Modern Applications”, *Materials* 3, 3468-3517 (2010).
- [18] O. Masahiro and M. Takuya, “Synthesis and modification of apatitenanoparticles for use in dental and medical applications”, *Japanese Dental Science Review* 51, 85-95 (2015).
- [19] W. Bonfield, M. D. Grynpas, A. E. Tully, J. Bowman and J. Abram, “Hydroxyapatite reinforced polyethylene - a mechanically compatible implant material for bone replacement”, *Biomaterials* 2, 185-186 (1981).
- [20] W. Bonfield, “Hydroxyapatite reinforced polyethylene as an analogous material for bone replacement”, *Ann. NY Acad. Sci.* 523, 173-177 (1988).
- [21] M. Wang, R. Joseph, W. Bonfield, “Hydroxyapatite-polyethylene composites for bone substitution: effects of ceramic particle size and morphology”, *Biomaterials* 19, 2357-2366 (1998).
- [22] S. K. Jenan, “Preparation and Characterization of Hydroxyapatite/ Yttria Partially Stabilized Zirconia Polymeric Biocomposite”, PhD. Thesis, Department of Production Engineering and Metallurgy- University of Technology, Baghdad, Iraq, 2014.

- [23] A. T. Procopio, A. Zavaliangos, J. C. Cunningham, “Analysis of the diametrical compression test and the applicability to plastically deforming materials”, *J.Mater. Sci.* 38, 3629-3639 (2003).
- [24] D. Grecu, I. Puculev, M. Negru, D. N. Tarnita, N. Ionvici and R. Dital, “Numerical simulations of the 3D virtual model of the human hip joint, using finite element method”, *Romanian Journal of Morphology and Embryology* 51 (1), 151–155 (2010).
- [25] Z. M. El Sallah, B. Smail, B. Ali, S. Abderahmen, B. B. Bachir and B. Serier, “Numerical Simulation of The Femur Fracture With and Without Prosthesis Under Static Loading Using Extended Finite Element Method (X-FEM)”, *Journal of Mechanical Engineering* 14 (1), 97-112 (2017).
- [26] R. Lennert, J. Dennis, B. Adam and V. Nico, “The Mechanical Response of a Polyetheretherketone Femoral Knee Implant Under a Deep Squatting Loading Condition”, *Proc IMechE Part H: J Engineering in Medicine* 231 (12) 1204–1212 (2017).
- [27] K. P. Sandeep and K. S. Jai, “A review on application of finite element modelling in bone biomechanics”, *Perspectives in Science* 8, 696-698 (2016).
- [28] S. Marek, G. Robert, A. Max, D. Charlène, G. Nicolas, E. Sebastian and V.Cécile, “A new approach to prevent contralateral hip fracture: Evaluation of the effectiveness of a fracture preventing implant”, *Clinical Biomechanics* 30 (7), 713-719 (2015).
- [29] A. MacLeod, A. H. Simpson and P. Pankaj, “Experimental and numerical investigation into the influence of loading conditions in biomechanical testing of locking plate fracture fixation devices”, *Bone and Joint Research* 7 (1), 111-1200 (2018).
- [30] N. Bartosz and N. Jerzy, “Numerical Simulation of Influence of Chosen Parameters on Tensile Stresses in Bone Cement Layer in Total Hip Arthroplasty”, *Advanced in Materials Science* 6 (2) (10), 9-17 (2006).
- [31] D. Ajay and B. Manish, “Finite element analysis of human fractured femur bone implantation with PMMA thermoplastic prosthetic plate”, *Procedia Engineering* 173, 1658-1665 (2017).
- [32] C. Desai, H. Hirani and A. Chawla, “Life Estimation of Hip Joint Prosthesis”, *The Institution of Engineers*, 1-7 (2014).
- [33] Z. Bing-hui, Q. Chuan-yong and Q. Qing-Hua, “Bone Distribution simulation during damage-repair bone remodeling in human proximal femur”, *Advanced Materials Research* 634-638, 883-891 (2013).
- [34] J. E. Shigley and C. R. Mischke, “*Mechanical Engineering Design*”, 8th ed., McGraw-Hill Inc., 2006.
- [35] J. S. Kashan, N. H. Rija, and T. A. Abbas, “Modified Polymer Matrix Nano Biocomposite for Bone Repair and Replacement- Radiological

- Study,” *Engineering and Technology Journal* 35 (Part A) (2), 365-371, (2017).
- [36] J. S. Kashan, , and S. M. Ali, “Modeling and simulation for mechanical behavior of modified biocomposite for scaffold application”, *Ingeniería e Investigación* 39(1), 63-75 (2019).
- [37] R. Dhabalel and V. S. Jattil “A bio-material: mechanical behaviour of LDPE-Al₂O₃-TiO₂”, *Materials Science and Engineering* 149, 1-10 (2016).

Influence of Process Parameters in Wire and Arc Additive Manufacturing (WAAM) Process

Nor Ana Rosli¹, Mohd Rizal Alkahari^{2*},
Faiz Redza Ramli³, Mohd Nizam Sudin⁴, Shajahan Maidin⁵

^{1,2,3,4}Faculty of Mechanical Engineering,
Universiti Teknikal Malaysia Melaka,
Hang Tuah Jaya Durian Tunggal, 76100, Melaka, Malaysia
*rizalalkahari@utem.edu.my

²Advanced Manufacturing Centre, Universiti Teknikal Malaysia Melaka,
Hang Tuah Jaya Durian Tunggal, 76100, Melaka, Malaysia

⁵Faculty of Manufacturing Engineering,
Universiti Teknikal Malaysia Melaka,
Hang Tuah Jaya Durian Tunggal, 76100, Melaka, Malaysia

^{1,2,4,5}Center of Advanced Research on Energy
Universiti Teknikal Malaysia Melaka,
Hang Tuah Jaya Durian Tunggal, 76100, Melaka, Malaysia

ABSTRACT

Wire and arc additive manufacturing (WAAM) has developed a wide range of processes and applications. This technology is a new approach to modern manufacturing and is gaining interest from the research community due to its ability to create affordable, large-scale components. Nevertheless, WAAM may be affected by porosity, humping and undercut. These issues need to be addressed in a specific way to achieve desired quality that is comparable to the traditional processing technique. This article examines various weld travel speeds, where defects start appearing. The effects of travel speed and wire feed speed (WFS) were also discussed. It was found that, travel speed and WFS had a major influence on deposition width and height and a stable deposited layer was produced between heat input values of 0.2620 kJ/mm and 0.32756 kJ/mm.

Keywords: *Wire and arc additive manufacturing, gas metal arc welding, additive manufacturing, 3D printing.*

Introduction

WAAM is one of the three-dimensional (3D) printing/additive manufacturing variants that involve the welding processes, such as inert gas and plasma welding [1]. Due to its potential and curiosity in understanding the process, many developments, mechanical properties and in process monitoring of the 3D metal printing have been reported [2, 3]. The potential of WAAM has gained much attention from the industrial manufacturing sector due to its capability to provide significant reductions in production cost and lead times [4]. WAAM uses a wire from a reel that feeds through a welding torch and passes a contact tip to supply the welding current. It also uses an electric arc as a heat source to deposit metal ornaments. The process can be divided into three distinctive methods depending on the wire being fed, which are gas metal arc welding (GMAW), gas tungsten arc welding (GTAW) and plasma arc welding (PAW) [5].

Besides the advantages offered by 3D printing in general, there is still a big gap between the knowledge and potential of 3D printing especially related to WAAM process that needs to be explored and optimized, such as process monitoring and control [6]. Some of the major challenges faced by all wire-feed AM processes, including WAAM, are the residual stresses and distortion generated during the process [7]. These problems may originate from the excessive energy input, high deposition rate or large temperature gradient due to the unfit input parameter at the beginning of the AM process. Therefore, optimum process parameters of WAAM are required to ensure the best possible final fabricated parts. WFS and travel speed are closely related to the quality of the formed part. A previous study showed that the travel speed significantly impacted the bead width, where it decreased as travel speed increased, whereas the bead height did not vary significantly. The relationship between the voltage and the theoretical wire speed was totally different from the one that was obtained experimentally, where in the theoretical case; the voltage increased as WFS was increased [8]. However, in practice the wire speed hardly reached the programmed value, therefore, the theoretically calculated voltages could not be reached. Diltthey claimed that there was a delay in droplet formation when the WFS was increased until enough energy from the arc was exposed to the wire [9]. As consequence, the distance between the wire and weld pool reduced and drastically changed the transfer modes.

In this study, the optimal process parameters of WAAM were studied in terms of WFS and travel speed of a 3D printer to enhance the quality of

WAAM process. The impacts of these two parameters were considered by analysing the defects formed on the multi-layer deposition.

Experimental Details

Experimental setup

The WAAM system consisted of a 3D printer machine, GMAW system and shielding gas system. The GMAW system is a heat source that was applied to melt the metal wire. The 3D printing machine with the GMAW system was developed in Universiti Teknikal Malaysia Melaka (UTeM) was used for this study. This is shown in Figure 1 [10].

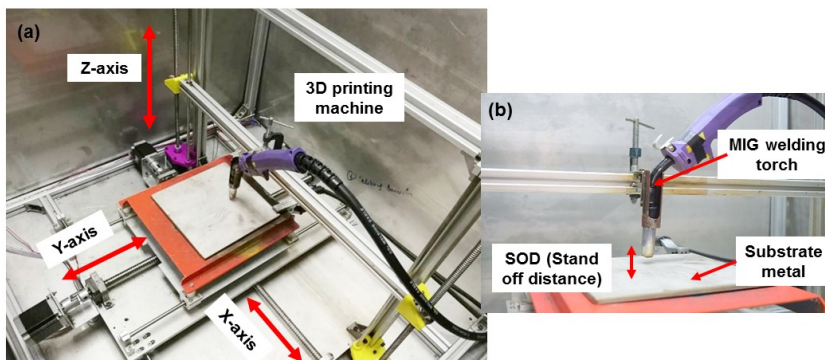


Figure 1: Experimental setup of WAAM system

A shielding gas that contained argon was utilised to avoid oxidation during the build-up process. The spool of the ER70S-6 with wire diameter of 1.2 mm was loaded on the wire-feeding system. It was also coaxial with the welding torch, which resulted in an easier tool path. The element content of the deposition wire (ER70S-6) is shown in Table 1. During the experiments, a 6 mm mild steel plate was employed as the base metal or substrate with dimensions of 300 mm × 300 mm × 300 mm. The stand-off distance (SOD) between the welding torch and substrate was constant at 5 mm. This was crucial to ensure uninterrupted deposition material and smooth wire-feeding supply to the melt pool. Low values of SOD were unable to supply smooth wire-feeding due to the small space, whereas high values of SOD resulted in wastage of wire deposition. The welding torch was mounted on the vertical plane of the z-axis direction and the substrate was placed on the horizontal plane of the x-axis and y-axis. The movement of each axis was driven by four stepper motors and controlled automatically through Repetier-Host. After

performing deposition on each layer, the z-axis was increased by a predefined layer height, while the substrate remained stationary. The deposition direction between the adjacent layers was zig-zag pattern as shown in Figure 2. This was done to provide a uniform layer height across the wall and consequently prevent the production of hump that could produce a depression at the end, which accumulates with each deposited layer.

Table 1: Chemical composition of metal wire ER 70S-6

Element	C	Mn	S	Ni	V	Cr	Cu	Si	P	Mo
wt%	0.06-	1.40-	0.035	0.15	0.03	0.15	0.50	0.80-	0.025	0.15
	0.15	1.85	max	max	max			1.15		max

Detail of Experimentation

The experiments were conducted to identify the effects of travel speed and WFS on deposition characteristics. The process overview as illustrated by the overall flow in Figure 2.

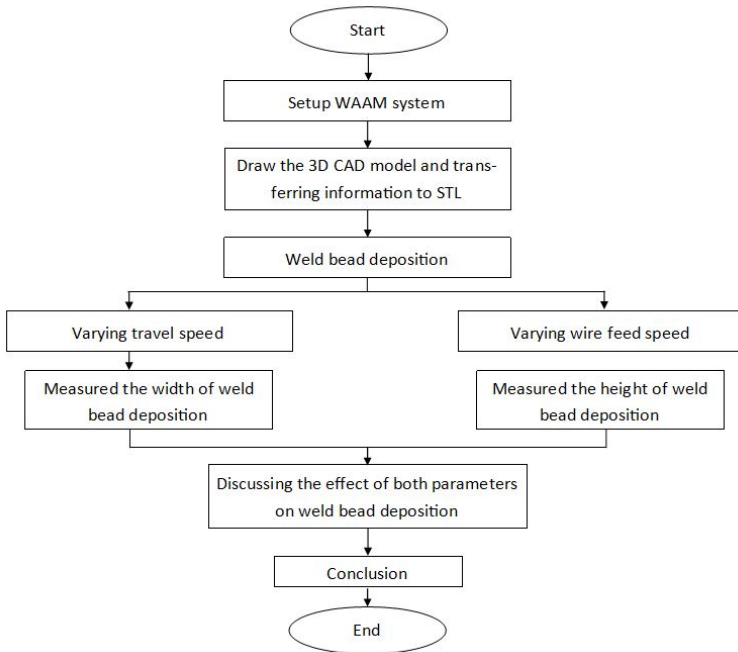


Figure 2: Flow chart for the study conducted

In this work, five layers were deposited under different values of travel speed and WFS. The deposition was performed with a dimension of 70 mm in length. The parameters used for each sample are presented in Table 2. There were seven process parameters listed, namely WFS, wire material, wire diameter, welding current, welding voltage, travel speed, and layer height. Some of the process parameters remained constant while varying travel speed and WFS.

Table 2. Process condition for deposit layers

Condition	Unit	
Wire feed speed (WFS)	mm/s	72, 80, 88, 120
Wire material	-	ER70S-6
Wire diameter (mm)	mm	1.2
Current, I	A	95
Voltage, V	V	17.24
Travel speed	mm/s	2,4,5,8,10,15
Layer height	mm	2.0

The main experiments were designed and conducted by setting the values of the travel speed and WFS to obtain different values of heat input. The test samples were made by superimposing five layers and applying the build orientation technique as shown in Figure 3. At the beginning, a SOD of 5 mm between the welding torch and substrate was measured. After the first layer, the increment of each layer was constant at 2.0 mm.

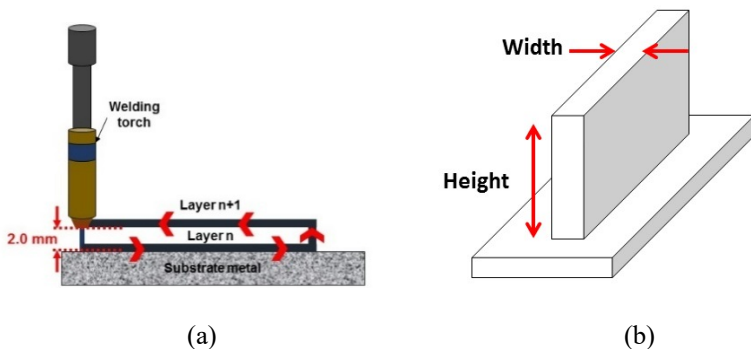


Figure 3: (a) Deposition direction of multi-layer weld bead, (b) Nomenclature of deposited layer output parameters

Results and Discussion

In order to obtain deposition of the intended shape without any defects, the most important key is to understand the effect of the process parameters involved. This section analyses the effects of heat input, printing speed and WFS on the deposited layer. During the measuring process, the deposited layer was captured to obtain the width and height along the deposition.

Effect of travel speed

The results presented six samples that were fabricated with varied printing speeds between 2 mm/s and 15 mm/s, while the WFS was kept constant at 120 mm/s. During the experiments, the properly formed deposited layer was measured in terms of width and relations to the variables. Figure 4 shows that as printing speed increases, the heat input decreases due to their inversely proportional relationship. On the other hand, the increase of the printing speed leads to the decrease of width of the deposited layer. This is because faster travel speeds enhance the cooling rate but reduce the ratio of the temperature gradient to solidification growth [11]. The evolution of the geometric characteristics shows that the width of the deposits decreases because heat accumulation reduces with increasing speed. An irregular bead deposit also takes places when the heat input reduces, thus forming a defect known as “humping” between the layers. Humping is one of the common defects that occurs in welding, which prevents further deposition operation [11]. This occurrence is related to low energy input from the heat source and high travel speeds [12]. After an irregular layer was formed at the beginning, it continued to the end of the deposit layers. It was observed that printing speeds between 4 mm/s and 5 mm/s produced a steady deposition width with an appropriate heat input to melt the metal wire and form successful weld beads.

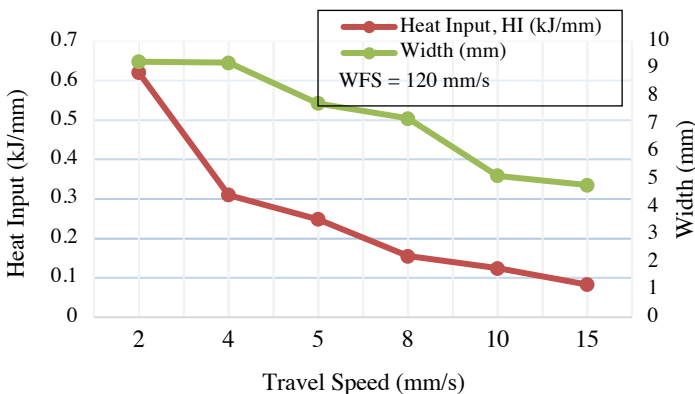


Figure 4: Effect of travel speed on deposit layers

As shown in Figure 5, two out of the six samples produced layer deposition with different travel speeds. At travel speed of 4 mm/s, a deposited layer with a thick width was formed without humping and regarded as a stable deposition. However, at travel speed of 8 mm/s, an unstable deposition was identified due to humping that occurred on the weld bead deposition. After five layers of deposition, the surface was uneven due to irregular deposition at the beginning. The formation of humping can also be described as periodic undulation that consists of hump and valley of the weld bead, which occur due to the backflow of molten metal [12]. Nonetheless, theoretically, higher travel speeds can be obtained by optimising various process parameters while maintaining the same heat input per distance [13].

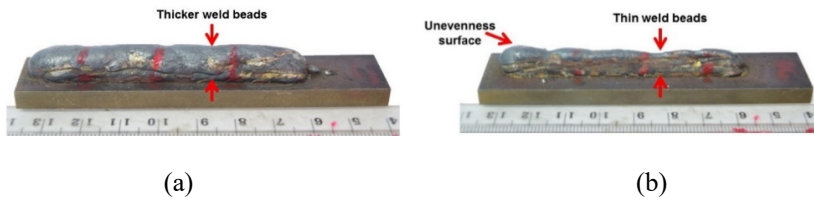
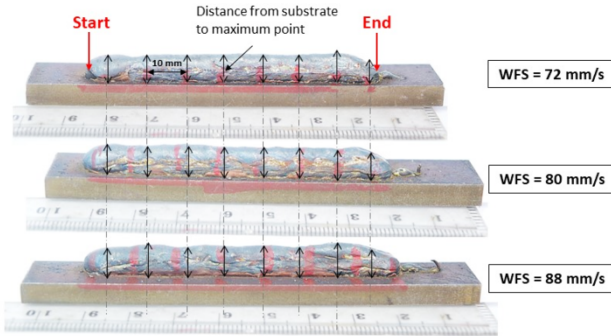


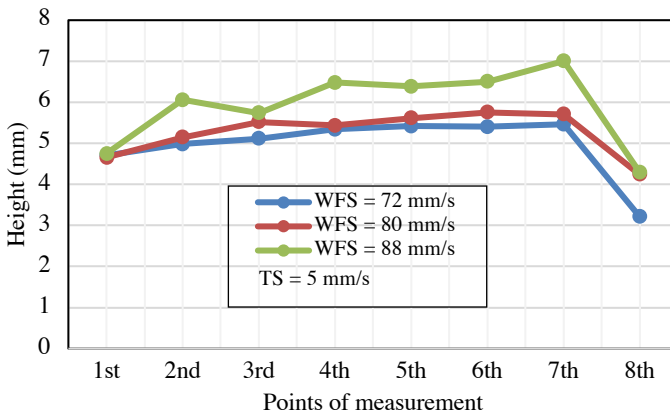
Figure 5: Various speed of weld deposition; (a) Travel speed 4 mm/s, and (b) Travel speed 8 mm/s

Effect of wire feed speed

WFS is one of the process parameters verified as a factor that influences the quality of a deposit. In this study, the WFS was varied from 72 mm/s to 88 mm/s. The height of the multi-layer deposition was, measured at eight different points along the layer surface as shown in Figure 6(a) and Figure 6(b). The results showed that the increase of WFS increased the unevenness of the bead surface within the framework of a constant travel speed. The deposition height increased rapidly with the increase of WFS and there was also a slight increase in deposition width. This was related to the overlapping process of the molten weld bead. The increasing WFS with a constant travel speed caused the material being deposited per unit time to increase by a constant heat input from the arc to the weld pool. Therefore, the process became unstable, undercut and lack of fusion might occur.



(a)



(b)

Figure 6: (a) Height was measured at eight different points, (b) Influence of wire feed speed on the layer deposit surface

The layer appearance is a clear indication of whether the layer deposition is stable or not. As shown in Figure 6(a), the layer looks unstable when the WFS is increased. Continuous layer deposition can still be obtained but the increasing amount of wire that is added to melt the pool leads to irregular layer deposition and influences the weld profile. Therefore, more energy is needed to melt the metal wire at higher WFS.

Conclusion

The purpose of this paper was to investigate the effects of travel speed and WFS. Therefore, the following conclusions were made:

- Travel speed and WFS had a major influence on deposition width and height.
- Based on the effect of travel speed on the deposited layer, it was concluded that the width of the deposit decreased due to heat accumulation, which reduced with increasing travel speed. As WFS increased, the deposition height also increased rapidly.
- An unstable deposition was identified at travel speed of 8 mm/s due to humping. As travel speed increased, the deposited layer became worse and defect started to occur. It started at the initial deposition and the increment of each layer became unstable. However, higher travel speeds could still be obtained by optimising other process parameters while maintaining the heat input per distance.
- A stable deposition was produced between heat input values of 0.2620 kJ/mm and 0.32756 kJ/mm.

Acknowledgements

The authors would like to thank Universiti Teknikal Malaysia Melaka (UTeM), and Ministry of Education Malaysia for research grant FRGS/1/2015/TK03/FKM/02/ F0026.

References

- [1] S. W. Williams, F. Martina, C. A. Addison, J. Ding, G. Pardal and P. Colegrove, "Wire + arc additive manufacturing," *Materials Science and Technology* 32(7), 641-647 (2016).
- [2] M. R. Alkahari, T. Furumoto, T. Ueda and A. Hosokawa, "Melt pool and single-track formation in selective laser sintering/selective laser melting," *Advanced Material Research* 933, 196-201 (2014).
- [3] H. A. Habeeb, M. R. Alkahari, F. R. Ramli, R. Hasan and S. Maidin, "Strength and porosity of additively manufactured PLA using a low-cost 3D printing," *Proceedings of Mechanical Engineering Research Day 2016*, 69-70 (2016).
- [4] S. Rios, P. A. Colegrove, F. Martina and S. W. Williams, "Analytical process model for wire + arc additive manufacturing," *Additive Manufacturing* 21, 651-657 (2018).
- [5] C. R. Cunningham, J. M. Flynn, A. Shokrani, V. Dhokia S. T. Newman, "Invited review article: Strategies and processes for high quality wire arc additive manufacturing," *Additive Manufacturing* 22, 672-686 (2018).
- [6] M.A. Nazan, F.R. Ramli, M.R. Alkahari, M.N. Sudin, M.A. Abdullah, "Optimization of warping deformation in open source 3D printer using

- response surface method,” Proceedings of Mechanical Engineering Research Day 2016, 71-72 (2016).
- [7] M. Dinovizer, X. Chen, J. Laliberte, X. Huang and H. Frei, “Effect of wire and arc additive manufacturing (WAAM) process parameters on bead geometry and microstructure,” Additive Manufacturing 26, 138-146 (2019).
- [8] J. L. Prado-Cerqueira, J. L. Diguez and A. M. Camcho, “Preliminary development of a wire and arc additive manufacturing system (WAAM),” Procedia Manufacturing 13, 895-902 (2017).
- [9] U. Dilthey, D. Fuest and W. Schellaer, “Laser welding with filler wire,” Optical and quantum electronics 27 (11), 1181-1191 (1995).
- [10] N. A. Rosli, M. R. Alkahari, F. R. Ramli, S. Maidin, M. N. Sudin, S. Subramoniam and T. Furumoto, “Design and development of a low-cost 3D metal printer,” Journal of Mechanical Engineering Research & Developments 41, 47-54 (2018).
- [11] A. Adebayo, J. Mehnen and X. Tonnelier, “Limiting travel speed in additive layer manufacturing,” (2013).
- [12] E. Soderstrom and P. Mendez, “Humping mechanisms present in high speed welding,” Science and technology of welding and joining 11(5), 572-579 (2006).
- [13] J. Ding, P. Colegrove, J. Mehnen, S. Ganguly, P. S. Almeida, F. Wang, and S. Williams, “Thermo-mechanical analysis of wire and arc additive layer manufacturing process on large multi-layer parts,” Computational Materials Science 50(12), 3315-3322 (2011).

Vibration Suppression Control of Three Inertial Systems

Duong Minh Duc*, Nguyen Manh Linh, Dao Quy Thinh, Do Trong Hieu
Hanoi University of Science and Technology

*duc.duongminh@hust.edu.vn

ABSTRACT

This paper concerns with vibration suppression control for three inertia resonance system which can be used as the model for many moving mechanisms widely used in industry such as steel rolling mills, flexible arms, large-scale space structures, etc. Since the mechanical resonance which causes vibration is unavoidable, especially at high speed operation, vibration suppression plays a key role in improving the accuracy of the system. In this research, a linear quadratic regulator-based speed controller with an integrator that can effectively suppress the torsional vibration is applied to control the system. Instead of using conventional state observer that is sensitive to noise and model uncertainties, the extended state observer is used to overcome the disturbance and uncertainty problems. Moreover, this observer also gives us the load torque information that is used to improve the load response. Simulation results show the effectiveness of the proposed controller. In addition, the comparison to conventional PID controller also be done to verify the advantages of the proposed approach.

Keywords: *Three inertial system; extended state observer; linear quadratic regulator; vibration suppression*

Introduction

Nowadays, high precision and fast response motor driver systems are widely used in industry such as steel rolling mill, robot manipulator, electrical vehicle, etc. Generally, these moving mechanisms can be regarded as multi-inertia systems with several inertia moments, gears and springs. Theoretically, vibration is unavoidable in above mentioned systems where motion is involved due to the mechanical resonance. For most motions, conventional proportional-integral-differential (PID) controller is sufficient to meet the desired requirements due to the fact that the nature frequency of the mechanical

system is quite high in comparison with the motion maneuver. However, for applications where both fast dynamic and high precision positioning are required, vibration suppression plays a key role in improving the system performance.

To deal with the vibration problem, most researches treat the motion mechanism as a 2-inertia system which comprised of mass, spring and damping. Then, various control methods are employed to suppress the vibration such as resonant ratio control [1], state feedback control [2,3], linear quadratic Gaussian (LQG) control [4,5], linear quadratic control with extended state observer (ESO) [6], active disturbance rejection control [7], fractional order PID- k controller [8], model predictive control [9], back-stepping position control [10], adaptive speed control [11]. Since the simplified model and the real system may be different in the number of resonant frequencies, i.e., the number of links of a manipulator is three or more, the effectiveness of the control system based on the 2-inertia model may be degraded in practice.

To further improve the system performance in term of vibration suppression, multi inertia model, i.e., three and more inertia system, is considered [12]. In [13], a three-inertia system is controlled by using PI/PID control. In addition, a modified integral plus proportional plus derivative (m-IPD) controller is used to suppress vibration in 3-inertia system. Fuzzy controller with differential evolution is also employed to control this 3-inertia system [12]. Despite of improved performance, the tuning procedure of the aforementioned methods are quite complicated due to the presence of the modeling error and uncertainties.

In this research, a linear quadratic regulator (LQR) control with an extended state observer (ESO) is proposed to handle the vibration problem of the 3-inertia system. The proposed method is not only effective in torsional vibration suppression but also robust against parameters variation since the ESO is employed to estimate the immeasurable state variables and load disturbance. In advanced, the tuning procedure of the method is simplified which plays a very importance role in practical applications. Particularly, the method can also be extended to higher order inertia systems.

To this end, the paper is organized as follows. The mathematical model of the 3-inertia system is introduced in section II. Section III shows the design procedure of the ESO and the LQR. Numerical simulations which verify the validity and effectiveness of the proposed strategy are shown in section IV. The conclusions are shown in the last section of the paper.

Three-Inertia System Model

A typical 3-inertia system, which consists of three rigid inertias and two torsional shafts, is shown in Figure 1.

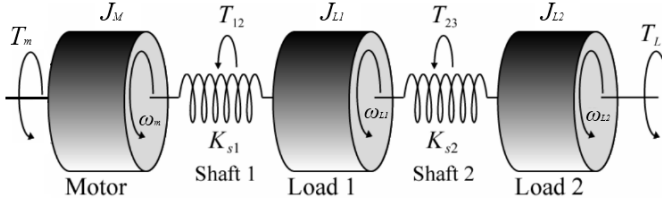


Figure 1: Three inertial system.

In this figure, ω_m is the motor angular speed, ω_{L1} is the angular speed of load 1, ω_{L2} is the angular speed of load 2, J_m is the motor inertia, J_{L1} is the inertia of load 1, J_{L2} is the inertia of load 2, T_m is the motor torque, T_L is the load torque, T_{12} is the torsional torque of shaft 1, T_{23} is the torsional torque of shaft 2, K_{s1} is the stiffness of shaft 1 and K_{s2} is the stiffness of shaft 2. The 3-inertia system can be modeled by the following equations:

$$\begin{cases} J_m \frac{d\omega_m}{dt} = T_m - T_{12} \\ \frac{dT_{12}}{dt} = K_{s1}(\omega_m - \omega_{L1}) \\ J_{L1} \frac{d\omega_{L1}}{dt} = T_{12} - T_{23} \\ \frac{dT_{23}}{dt} = K_{s2}(\omega_{L1} - \omega_{L2}) \\ J_{L2} \frac{d\omega_{L2}}{dt} = T_{23} - T_L \end{cases} \quad (1)$$

Equation (1) can be rewritten in state-space form as:

$$\begin{aligned} \dot{x} &= Ax + B_1 T_L + B_2 T_m \\ y &= Cx \end{aligned} \quad (2)$$

where

$$A = \begin{bmatrix} 0 & -1/J_m & 0 & 0 & 0 \\ K_{s1} & 0 & -K_{s1} & 0 & 0 \\ 0 & 1/J_{L1} & 0 & -1/J_{L1} & 0 \\ 0 & 0 & K_{s2} & 0 & -K_{s2} \\ 0 & 0 & 0 & 1/J_{L2} & 0 \end{bmatrix} \quad (3)$$

$$B_1 = \begin{bmatrix} 0 \\ 0 \\ 0 \\ 0 \\ -1/J_{L2} \end{bmatrix} \quad B_2 = \begin{bmatrix} 1/J_m \\ 0 \\ 0 \\ 0 \\ 0 \end{bmatrix}$$

$$C = [1 \quad 0 \quad 0 \quad 0 \quad 0];$$

From Equation (2), the transfer function from T_m to ω_m is:

$$\frac{\omega_m(s)}{T_m(s)} = \frac{(s^2 + \omega_{a1}^2)(s^2 + \omega_{a2}^2)}{J_m(s^2 + \omega_{r1}^2)(s^2 + \omega_{r2}^2)} \quad (4)$$

In which, ω_{a1} , ω_{a2} are anti-resonant frequencies and ω_{r1} , ω_{r2} are resonant frequencies of the system and are given by.

$$\omega_{a1} = \frac{1}{\sqrt{2}} \sqrt{\left(\frac{K_{s1} + K_{s2}}{J_{L1}} + \frac{K_{s2}}{jL2}\right) - \sqrt{\left(\frac{K_{s1} + K_{s2}}{J_{L1}} + \frac{K_{s2}}{jL2}\right)^2 - 4 \frac{K_{s1}K_{s2}}{J_m}}} \quad (5)$$

$$\omega_{a2} = \frac{1}{\sqrt{2}} \sqrt{\left(\frac{K_{s1} + K_{s2}}{J_{L1}} + \frac{K_{s2}}{jL2}\right) + \sqrt{\left(\frac{K_{s1} + K_{s2}}{J_{L1}} + \frac{K_{s2}}{jL2}\right)^2 - 4 \frac{K_{s1}K_{s2}}{J_m}}} \quad (6)$$

$$\omega_{r1} = \frac{1}{\sqrt{2}} \sqrt{\frac{\left(\frac{K_{s1}}{J_m} + \frac{K_{s1} + K_{s2}}{J_{L1}} + \frac{K_{s2}}{jL2}\right) - \sqrt{\left(\frac{K_{s1}}{J_m} + \frac{K_{s1} + K_{s2}}{J_{L1}} + \frac{K_{s2}}{jL2}\right)^2 - 4 \frac{J_m + J_{L1} + J_{L2}}{J_{L1}J_{L2}} K_{s1}K_{s2}}}{2}} \quad (7)$$

$$\omega_{r2} = \frac{1}{\sqrt{2}} \sqrt{\frac{\left(\frac{K_{s1}}{J_m} + \frac{K_{s1} + K_{s2}}{J_{L1}} + \frac{K_{s2}}{jL2}\right) + \sqrt{\left(\frac{K_{s1}}{J_m} + \frac{K_{s1} + K_{s2}}{J_{L1}} + \frac{K_{s2}}{jL2}\right)^2 - 4 \frac{J_m + J_{L1} + J_{L2}}{J_{L1}J_{L2}} K_{s1}K_{s2}}}{2}} \quad (8)$$

These resonant frequencies cause vibrations and therefore degrade the system performance. The controller must be designed not only for speed/position tracking, but also for vibration suppression.

Control of 3-Inertia System

State and Disturbance Observer

To implement the state feedback controller, all the state variables should be known. However, not all state variables are available for measure because of

the high cost, mounting constraints or noise. In this case, a state observer is a good solution to estimate the immeasurable state variables. In this paper, the ESO [14] is chosen because of its better performance over other observers such as high-gain and sliding-mode observers in term of robustness against disturbance.

Consider the fifth order system (2), in order to estimate the states and loads disturbance of this system by the ESO, the following transformation matrix T is employed:

$$T = \begin{bmatrix} 1 & 0 & 0 & 0 & 0 \\ 0 & -J_m & 0 & 0 & 0 \\ 1 & 0 & \frac{J_m}{K_{S1}} & 0 & 0 \\ 0 & -(J_m + J_{L1}) & 0 & -\frac{J_{L1}J_m}{K_{S1}} & 0 \\ 1 & 0 & \frac{J_m}{K_{S1}} + \frac{J_m + J_{L1}}{K_{S2}} & 0 & \frac{J_{L1}J_m}{K_{S1}K_{S2}} \end{bmatrix} \quad (9)$$

Let $x^* = T^{-1}x$. Then, Equation (2) can be written as:

$$\begin{cases} \dot{x}_1^* = x_2^* + \frac{1}{J_m} u \\ \dot{x}_2^* = x_3^* \\ \dot{x}_3^* = x_4^* - \frac{K_{S1}}{J_m^2} u \\ \dot{x}_4^* = x_5^* \\ \dot{x}_5^* = a(t) + \frac{K_{S1}^2}{J_m^2} \left(\frac{1}{J_m} + \frac{1}{J_L} \right) u \\ y = x_1^* \end{cases} \quad (10)$$

with

$$a(t) = (-K_{S1}K_{S2} \frac{J_m + J_{L1} + J_{L2}}{J_m J_{L1} J_{L2}}) x_2^* + \left(\frac{-1}{J_{L2}} + \frac{K_{S1} + K_{S2}}{J_{L1}} + \frac{K_{S1}}{J_m} \right) x_4^* - \frac{K_{S1}K_{S2}}{J_m J_{L1} J_{L2}} T_L \quad (11)$$

By treating $a(t) = x_6^*(t)$ as an augmented state variable, $h(t)$ as the derivative of $a(t)$ which is unknown, the system state-space model in Equation (10) becomes:

$$\begin{cases} \dot{x}_1^* = x_2^* + \frac{1}{J_m} u \\ \dot{x}_2^* = x_3^* \\ \dot{x}_3^* = x_4^* - \frac{K_{s1}}{J_m^2} u \\ \dot{x}_4^* = x_5^* \\ \dot{x}_5^* = x_6^* + \frac{K_{s1}^2}{J_m^2} \left(\frac{1}{J_m} + \frac{1}{J_L} \right) u \\ \dot{x}_6^* = h(t) \\ y = x_1^* \end{cases} \quad (12)$$

To estimate the new states variable x^* , the following ESO is used:

$$\begin{cases} e = z_1 - y \\ \dot{z}_1 = z_2 - \beta_1 g_1(e) + \frac{1}{J_m} u \\ \dot{z}_2 = z_3 - \beta_2 g_2(e) \\ \dot{z}_3 = z_4 - \beta_3 g_3(e) - \frac{K_{s1}}{J_m^2} u \\ \dot{z}_4 = z_5 - \beta_4 g_4(e) \\ \dot{z}_5 = z_6 - \beta_5 g_5(e) + \frac{K_{s1}^2}{J_m^2} \left(\frac{1}{J_m} + \frac{1}{J_L} \right) u \\ \dot{z}_6 = \beta_6 g_6(e) \end{cases} \quad (13)$$

where β_i ($i=1, \dots, 6$) are observer gains, z_i ($i=1, \dots, 6$) are estimated values of x_i^* , and $g_i(e)$ ($i=1, \dots, 6$) can be either linear or nonlinear functions. In this paper, $g_i(e) = e$ is chosen. With appropriate values of β_i , the estimation of x_i^* and the system states $\hat{x} = T\hat{x}^*$ can be obtained. Then the estimation of load torque \hat{T}_L can be determined by

$$\hat{T}_L = \left(-a(t) + \left(-K_{s1}K_{s2} \frac{J_m + J_{L1} + J_{L2}}{J_m J_{L1} J_{L2}} \right) x_2^* + \left(\frac{-1}{J_{L2}} + \frac{K_{s1} + K_{s2}}{J_{L1}} + \frac{K_{s1}}{J_m} \right) x_4^* \right) \frac{J_m J_{L1} J_{L2}}{K_{s1} K_{s2}} \quad (14)$$

Controller Design

To extend the bandwidth of the motion mechanism, vibration caused by mechanical resonant must be suppressed. Besides, other requirements of a standard controlled system such as stability, minimal tracking error, etc., must also be fulfilled. To achieve the aforementioned goals simultaneously, a state feedback control with an extended integral of error state variable is utilized to eliminate the steady-state error. The design procedure is as followings.

The block diagram of the state feedback control system is shown in Figure 2 in which K_i is the integral gain, K_d is feed forward gain to compensate the load torque, and $F = [f_1 f_2 f_3 f_4 f_5]$ is the state feedback gain.

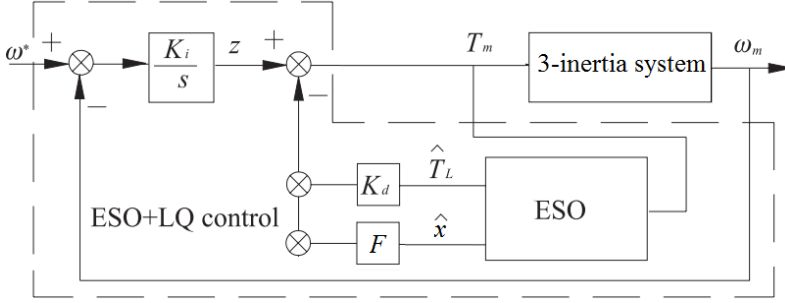


Figure 2: Proposed controller schema

In order to determine the integral gain and the state feedback gain, we first define a new state variable S as:

$$S = \int_0^t (\omega_m - \omega^*) dt \quad (15)$$

Then, by differentiating both sides of Equation (15), it yields:

$$\dot{S} = \omega_m - \omega^* = Cx - \omega^* \quad (16)$$

Combining Equation (2) and Equation (16), a new state-space model in which the torque T_m is substituted by the control signal u is derived as follows:

$$\begin{bmatrix} \dot{x} \\ \dot{S} \end{bmatrix} = \begin{bmatrix} A & 0 \\ C & 0 \end{bmatrix} \begin{bmatrix} x \\ S \end{bmatrix} + \begin{bmatrix} B_2 \\ 0 \end{bmatrix} u + \begin{bmatrix} B_1 & 0 \\ 0 & -1 \end{bmatrix} \begin{bmatrix} T_L \\ \omega^* \end{bmatrix} \quad (2)$$

In steady-state, $\dot{x} = 0$ and $\dot{S} = 0$, then the steady-state solution x_s , S_s and u_s must satisfy the following equation:

$$\begin{bmatrix} B_1 & 0 \\ 0 & -1 \end{bmatrix} \begin{bmatrix} T_L \\ \omega^* \end{bmatrix} = - \begin{bmatrix} A & 0 \\ C & 0 \end{bmatrix} \begin{bmatrix} x_s \\ S_s \end{bmatrix} - \begin{bmatrix} B_2 \\ 0 \end{bmatrix} u_s \quad (18)$$

Substituting Equation (18) into Equation (17), it gives:

$$\begin{bmatrix} \dot{x} \\ \dot{S} \end{bmatrix} = \begin{bmatrix} A & 0 \\ C & 0 \end{bmatrix} \begin{bmatrix} x - x_s \\ S - S_s \end{bmatrix} + \begin{bmatrix} B_2 \\ 0 \end{bmatrix} (u - u_s) \quad (19)$$

Define a new state variable Z as:

$$Z = \begin{bmatrix} Z_1 \\ Z_2 \end{bmatrix} = \begin{bmatrix} x - x_s \\ S - S_s \end{bmatrix}, \dot{Z} = \begin{bmatrix} \dot{x} \\ \dot{S} \end{bmatrix}, q = u - u_s \quad (20)$$

Then Equation (19) becomes:

$$\dot{Z} = \begin{bmatrix} A & 0 \\ C & 0 \end{bmatrix} \begin{bmatrix} Z_1 \\ Z_2 \end{bmatrix} + \begin{bmatrix} B_2 \\ 0 \end{bmatrix} q = \bar{A}Z + \bar{B}q \quad (21)$$

Choose the performance index J as follows:

$$J = \int_0^\infty [\alpha(\omega_m - \omega_m^*)^2 + \beta(\omega_{L1} - \omega_m^*)^2 + \varepsilon(\omega_{L2} - \omega_m^*)^2 + \delta(S - S_s)^2 + \gamma(u - u_s)^2] dt \quad (22)$$

or

$$J = \int_0^\infty (Z^T QZ + Rq^2) dt \quad (23)$$

where

$$Q = \begin{bmatrix} \alpha & 0 & 0 & 0 & 0 & 0 \\ 0 & 0 & 0 & 0 & 0 & 0 \\ 0 & 0 & \beta & 0 & 0 & 0 \\ 0 & 0 & 0 & 0 & 0 & 0 \\ 0 & 0 & 0 & 0 & \varepsilon & 0 \\ 0 & 0 & 0 & 0 & 0 & \delta \end{bmatrix} \text{ and } R = \gamma$$

Then, the state feedback gain $K = [K_1 K_2]$ of the LQR control for system in Equation (21) subject to performance index in Equation (22) can easily be computed. Consequently, the control input q is:

$$q = -KZ = -K_1 Z_1 - K_2 Z_2 \text{ or } u - u_s = -K_1(x - x_s) - K_2(S - S_s) \quad (24)$$

Since $u_s = -K_1 x_s - K_2 S_s$ in steady state, Equation (24) becomes:

$$u = -K_1 x - K_2 S = -K_1 x - K_2 \int_0^t (\omega_m - \omega^*) d\tau \quad (25)$$

By considering Figure 2, it can be realized that $F = [f_1 f_2 f_3 f_4 f_5] = K_I$ and $K_I = K_2$. Since the load torque of which the sudden change may cause speed drop and initiate hazardous torsional vibration is observed by the ESO, the feed forward compensation gain $K_d = 1$ is sufficient.

With the ESO, the state estimation errors can approach zero with arbitrarily dynamic [15]. Then, the stability of the control system can be guaranteed by the LQR controller [16].

Numerical Simulation

In this section, numerical simulations are carried out to verify the effectiveness of the proposed control strategy. The systems parameters are provided in Table 1.

Table 1: Systems parameters

Name	Symbol	Value
Motor inertia	J_m	1552 Kg m^2
Inertia of load 1	J_{L1}	1000 Kg m^2
Inertia of load 2	J_{L2}	542 Kg m^2
Stiffness of shaft 1	K_{S1}	5.93×10^6 Nm rad^{-1}
Stiffness of shaft 2	K_{S2}	5.93×10^6 Nm rad^{-1}
Load Disturbance	T_L	0.2×10^6 Kg m^2

After being well tuned, weighting matrices Q and R in Equation (23) are chosen with $\alpha = 1000$, $\beta = 10^7$, $\varepsilon = 7.10^6$, $\delta = 10^{13}$ and $\gamma = 1$. Then, the state-feedback gain is $K = [3,0560.10^5 \quad 2,2702 \quad 2,0347.10^4 \quad -1.0770 \quad 2.7274.10^3 \quad 3,1623.10^6]$. The gains of ESO are $\beta_1 = 6\omega_0$, $\beta_2 = 15\omega_0^2$, $\beta_3 = 20\omega_0^3$, $\beta_4 = 15\omega_0^4$, $\beta_5 = 6\omega_0^5$ and $\beta_6 = \omega_0^6$ where $\omega_0 = 1000$.

The performance of the proposed control strategy is first investigated by step-response analysis. A constant reference speed, i.e., 30 rad/s, is used and the corresponding systems response is shown in Figure 3. It can be observed that the speed of the motor and loads quickly track the reference speed without vibration. In addition, the robustness of the controller against the load disturbance is also verified in this simulation. In detail, an external disturbance is introduced at time instance $1s$. It can be seen that the influence of the disturbance is quickly compensated by the controller in about 0.1 s.

In order to show the validity of the ESO, the error between the real and the observed speeds of motor, load 1 and load 2 are calculated and shown in Figure 4. It can be realized that these errors are extremely small even in transient-state, and quickly converge to zero in steady-state.

To show the advantage of the proposed control strategy over the conventional PID controller, comparative simulation is also carried out. A PID controller of which parameters are well tuned by particle swarm optimization (PSO) technique is used for system (2). The comparative speed responses of the PID controller and the proposed controller are provided in Figure 5. It can be seen that although being optimized, the PID controller still shows poor performance, i.e., large overshoot with torsional vibration. In contrast, the

proposed controller shows much better performance with smooth transient-state whilst the vibration is completely removed.

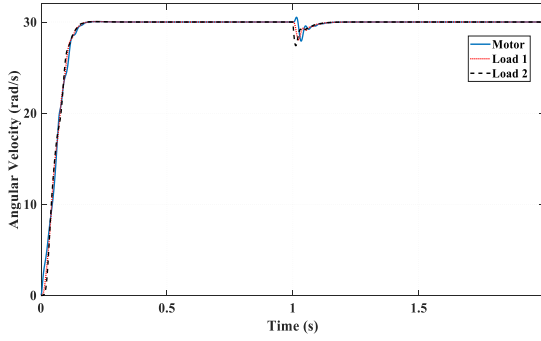


Figure 3: Velocity responses of the system with the proposed controller

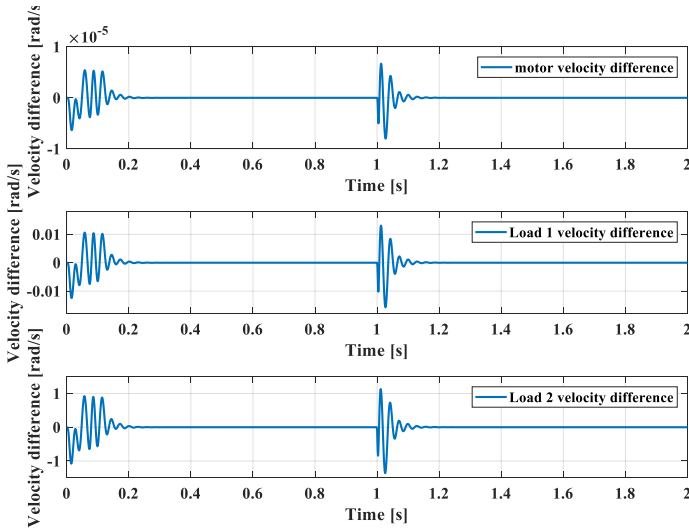
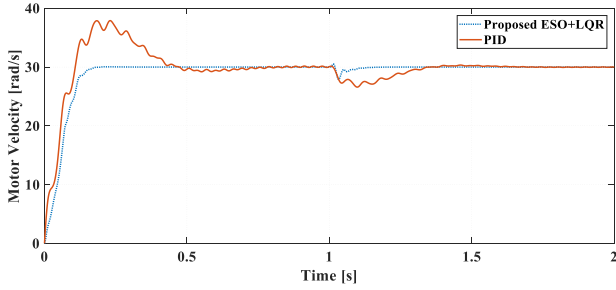
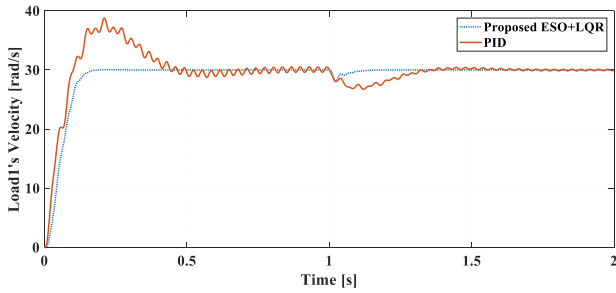


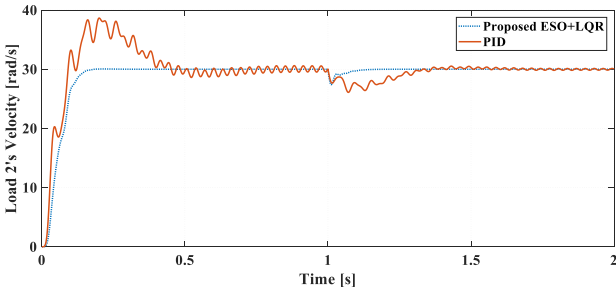
Figure 4: Speed estimation errors



(a) Motor velocity



(b) Load 1 velocity



(c) Load 2 velocity

Figure 5: Comparison between PID and the proposed controller

Finally, the robustness of the proposed control strategy against the parameter variation is test. The moment of inertial of the loads used in simulation is two times larger than the one used in control design. The simulation result in this case is shown in Figure 6. Although the system model is inaccurate, the system speed still tracks the reference one without vibration. However, the overshoot is unavoidable in this case. The reason may come from the transient response of the ESO.

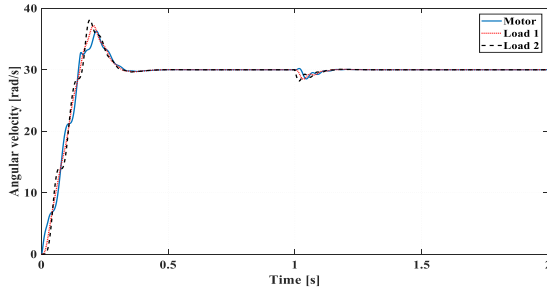


Figure 6: Velocity responses of the system with the proposed controller in case of parameter uncertainty.

Conclusion

In this paper, we proposed the LQR controller based ESO for a three-inertia system in order to achieve vibration suppression and disturbance rejection. The unknown states and load torque are estimated using ESO. Then, the state feedback and feedforward compensation for load torque are employed in control design. Theoretical analysis and numerical simulations show that the proposed control strategy guarantees the system stability, good performance and robustness with parameters variation as well as load disturbance. Particularly, the control strategy can easily be extended to be applied to any order inertia systems.

References

- [1] Hori, Yoichi, Hideyuki Sawada, and Yeonghan Chun, "Slow resonance ratio control for vibration suppression and disturbance rejection in torsional system," *IEEE Transactions on Industrial Electronics* 46.1, 162-168 (1999).
- [2] Song, Seung-Ho, et al., "Torsional vibration suppression control in 2-mass system by state feedback speed controller," *Proceedings of IEEE International Conference on Control and Applications* IEEE (1993).
- [3] Hori, Yoichi, Hiroyuki Iseki, and Koji Sugiura, "Basic consideration of vibration suppression and disturbance rejection control of multi-inertia system using SFLAC (state feedback and load acceleration control)," *IEEE Transactions on Industry Applications* 30.4, 889-896 (1994).
- [4] Ji, Jun-Keun, Dong-Choon Lee, and Seung-Ki Sul, "LQG based speed controller for torsional vibration suppression in 2-mass motor drive

- system," Proceedings of IECON'93-19th Annual Conference of IEEE Industrial Electronics. IEEE (1993).
- [5] Ji, Jun-Keun, and Seung-Ki Sul, "Kalman filter and LQ based speed controller for torsional vibration suppression in a 2-mass motor drive system," *IEEE Transactions on industrial electronics* 42.6, 564-571 (1995).
 - [6] Zhang, Ruicheng, and Chaonan Tong, "Torsional vibration control of the main drive system of a rolling mill based on an extended state observer and linear quadratic control," *Journal of Vibration and Control* 12.3, 313-327 (2006).
 - [7] Zhao, Shen, and Zhiqiang Gao, "An active disturbance rejection based approach to vibration suppression in two-inertia systems," *Asian Journal of Control* 15.2, 350-362 (2013).
 - [8] Ma, Chengbin, and Yoichi Hori, "Backlash vibration suppression control of torsional system by novel fractional order PIDk controller," *IEEJ Transactions on Industry Applications* 124.3, 312-317 (2004).
 - [9] P. J. Serkies and K. Szaba, "Model predictive control of the two-mass with mechanical backlash," *Computer Applications in Electrical Engineering*, 170-180 (2011).
 - [10] M. Mola, A. Khayatian, and M. Dehghani, "Backstepping position control of two-mass systems with unknown backlash," 2013 9th Asian Control Conference, ASCC (2013).
 - [11] S. Brock, D. Luczak, K. Nowopolski, T. Pajchrowski, and K. Zawirski, "Two Approaches to Speed Control for Multi-Mass System with Variable Mechanical Parameters", *IEEE Transactions on Industrial Electronics*, 64 (4), 3338-3347 (2017).
 - [12] Ikeda, Hidehiro, and Tsuyoshi Hanamoto, "Fuzzy controller of three-inertia resonance system designed by differential evolution." *Journal of International Conference on Electrical Machines and Systems* 3 (2), (2014).
 - [13] G. Zhang and J. Furusho, "Control of three-inertia system by PI/PID control", *Trans of IEE Japan* 119-D (11), 1386-1392 (1999).
 - [14] Huang, Yi, and Wenchao Xue, "Active disturbance rejection control: methodology and theoretical analysis," *ISA transactions* 53.4, 963-976 (2014).
 - [15] D. Yoo, S. S. T. Yau, Z.Gao, "On convergence of the linear extended observer," Proceedings of the IEEE International Symposium on Intelligent Control, Munich, Germany, 1645-1650 (2006).
 - [16] Anderson, B. D., & Moore, J. B., "Optimal control: linear quadratic methods," Courier Corporation (2007).

Heat Transfer of Swirling Multi Jets Impinging System

Amar Zerrouk*, Ali Khelil, Larbi Loukarfi
Control Laboratory, Test, Measurement and Mechanical Simulation,
University of Chlef, Algeria, BP 151
*zerroukamar@yahoo.fr

ABSTRACT

This work is the subject of an experimental and a numerical study of a system of swirling jets system impinging a plane wall. The experimental test bench comprising three diameter D diffusers, which are $2D$ distant between the axes, impacting perpendicular plate, by setting the impact height $H = 4D$. The swirl is obtained by a generator (swirl) of compound 12 fins arranged at 60° relative to the vertical placed just at the exit of the diffuser. A portable VELOCICALC PLUS anemometer device at various stations measures the blowing temperature of the swirling jets hitting the plate. The results of this study have shown that, the global jet has the same characteristics as a free jet, close to the obstacle it undergoes a considerable deviation characterized by the weakening of the temperature and the speeds then the development of the jet. The temperature amplitudes decrease, as we approach the plate. The velocity profiles show that velocity changes direction and increases radially. The Nusselt number is moderate at the level of the impact surface ensuring the homogenization of the heat transfer of the plate. The system was simulated numerically by the Fluent program based on the turbulence model (k -epsilon). The latter gave results of temperature and velocity fields having profiles in line with those of experimental results.

Keywords: *Turbulent swirling jet, impinging a plaque, thermal homogenization, ventilation, (k -epsilon) model.*

Nomenclatures

D: Diameter of the diffuser [m]
d: Diameter of the valve diffuser support [m]
 D_{hy} : Hydraulic diameter [m]
H: Impact height [m]

- G_θ : Flux of angular momentum [$\text{m}^4.\text{s}^{-2}$]
 G_x : Flux of Axial momentum [$\text{m}^4.\text{s}^{-2}$]
 R : Radius of the diffuser [m]
 r, X : Dimensional cylindrical coordinates [m]
 Nu : Nusselt Number [-]
 R_h : Radius of the valve diffuser support [m]
 R_n : The radius of diffuser [m]
 Re : Reynolds number [-]
 S : Swirl number [-]
 T_a : Ambient temperature [$^\circ\text{C}$]
 T_i : Jet temperature at the point considered. [$^\circ\text{C}$]
 T_r : Reduced temperature [-]
 T_m : Maximum temperature at the outlet of the diffuser [$^\circ\text{C}$]
 U : Velocity in the axial direction [$\text{m}.\text{s}^{-1}$]
 U_m : Maximum velocity at the exit of the diffuser [$\text{m}.\text{s}^{-1}$]
 U_r : Reduced dimensionless axial velocity. [-]
 U_i : Jet velocity at the point considered [$\text{m}.\text{s}^{-1}$]
 V : Velocity in the radial direction [$\text{m}.\text{s}^{-1}$]
 W : Velocity in the tangential direction [$\text{m}.\text{s}^{-1}$]
 α : Inclination angle of the vanes [$^\circ\text{deg}$].

Introduction

Several research papers have treated the convective transfer of free jet and confined flows, the swirling flow characteristics through an air jet impinging on flat surfaces or complex geometry, in order to improve the transfer of heat or localized mass in a portion of a system. This type of configuration is used in particular for anti-icing systems for aircraft turbojet engines as shown in Figure 1, for cooling electronic components, blading turbines, or quenching metallurgical and glass flows, as well as in convective drying of tunnels. A method commonly used in the aeronautical field for anti-ice operations of the front part turbojet engines of airplanes using hot air jet impinging the walls of frosted internal power of the engine as shown in Figure 1. For this, it is necessary to know the structure of the impinging jet in Figure 2, and the parameters that influence this behavior.

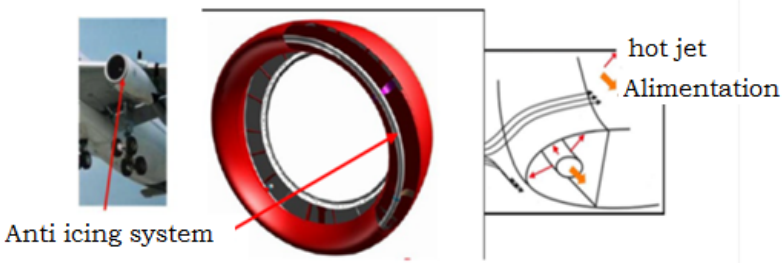


Figure 1: Anti-icing of the turbojet engine by impacting jets [1]

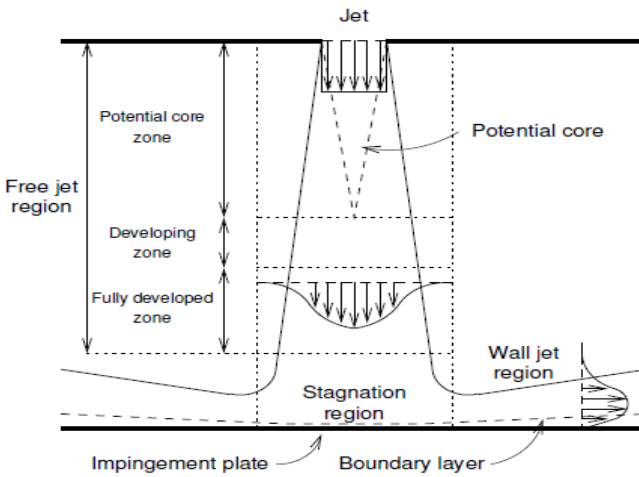


Figure 2: Flow configuration of a round impinging jet with regions of different flow regimes [2]

This section presents an overview of the current knowledge of the flow and heat transfer of both single impinging jets and multiple impinging jet arrays. First, the hydrodynamics of a single jet are described, followed by the flow features of multiple jet arrays. Next, single and multiple jet heat transfer is discussed. The dependencies of the Nusselt number on geometrical parameters and the temperature of the jet are discussed based on non-dimensional correlations.

Figure 2 shows the flow of an impinging jet issuing from a nozzle in a flat plate. An impinging jet is commonly divided into three regions based on the flow structure: the free jet region, the stagnation region, and the wall jet region.

Experimental setup

The realized experimental device as shown in Figure 3 composed of a frame of the cubic shape of metal; having at its upper part the hot air blowing apparatus (hairdryer), directed from the top downwards and in its lower part a diffuser (1) according to configuration studied. This device allows scanning the maximum space provided by a particular arrangement of the rods supporting the temperature sensors (2); the temperature field is explored through a portable anemometer device VELOCICALC PLUS (3). Easily guided rods support the sensors vertically and horizontally to sweep the maximum space, a horizontal plate (4) Formica material, the temperature and velocity fields are measured in different stations in the axial directions and radial flow.

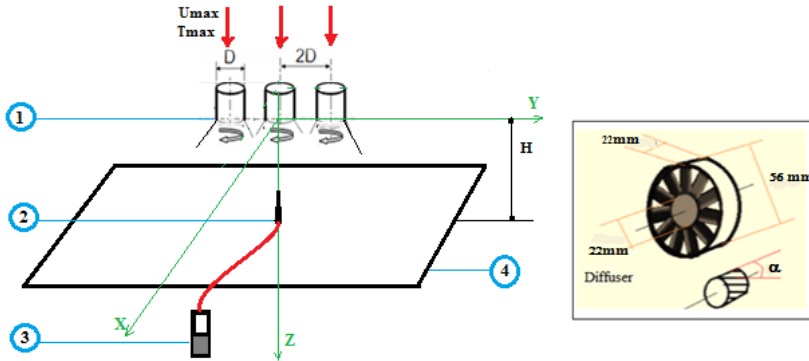


Figure 3: Experimental configuration and visualization of digital sensors [3]

The Number of Swirl

A dimensionless number that defines a measure of the ratio between the angular momentum of the axial flow and axial momentum characterizes the swirl [4].

$$S = \frac{G_{\theta}}{RG_x} = \frac{\int_0^R r^2 U W dr}{R \int_0^R \left(U^2 - \frac{W^2}{2} \right) dr} \quad (1)$$

The swirl number can be evaluated at any position of the jet because the two quantities are calculated. Swirling helps promote and improve the process

of mixing and transfer, as well as the jet has the advantage of quickly flourish in free jets.

Another empirical formula is used for calculating the number of swirl that the swirl number defined according to the geometric parameters of the swirl generator. This number S can be written as follows [5]:

$$S = \frac{2}{3} \left[\frac{1 - \left(\frac{R_h}{R_n} \right)^3}{1 - \left(\frac{R_h}{R_n} \right)^2} \right] \cdot \text{tg} \alpha \quad (2)$$

Such that:

α : is the angle of the fins built swirl generator (see Figure 3),

R_h : is the radius of the vane diffuser support,

R_n : is the radius of diffuser.

Note that in the case of a swirler hub without a nucleus ($R_h = 0$), the expression becomes [6]:

$$S = \frac{2}{3} \text{tg} \alpha \quad (3)$$

In this study, the axial and tangential velocities U and W , respectively, were measured at the outlet of a diffuser with a swirling jet hot wire anemometer triple probes (DISA55M01). Four values of the swirl number can be used, $S = 0$ to $\alpha = 0^\circ$, $S = 0.4$ to $\alpha = 30^\circ$, $S = 0.7$ to $\alpha = 45^\circ$ and $S = 1.3$ to $\alpha = 60^\circ$, respectively. According to reference [7], the swirl number is used, which corresponds to $\alpha = 60^\circ$.

Operating Conditions

The experimental setup was placed in a laboratory room isolated from the outside air, having the following dimensions: length = 4 m, width = 3.5 m and height = 3 m. There must be a free flow of the isolation and testing, the initial temperature at the blowing port was 90°C for each jet.

Measurement Procedure

The values of the initial flowing temperature (T_i) and the value of the ambient temperature (T_a) is measured by precision temperature sensors (1/100). It is noted that when the temperature stabilizes, with a delay ten minutes was sufficient to achieve this stabilization, after measuring, the temperatures for a

given configuration, the blowing sail is stopped and preceded to the movement of the rods door probes to other measurement point.

Dimensionless Quantities

The reduced temperature of measurement is obtained by reference to the maximum average temperature at the outlet of the blowing port and the room temperature:

$$T_r = \frac{T_i - T_a}{T_{max} - T_a} \quad (4)$$

The reduced dimensionless axial velocity is obtained from the maximum speed to the outlet of the blowing port.

$$U_r = \frac{U_i}{U_{max}} \quad (5)$$

The radial and axial distances are given by reference to the diameter of the blow port as dimensionless r/D and x/D .

Numerical Procedure

The Turbulence Model (k-ε) Standard

The turbulence model (K-ε) is a model of turbulent viscosity in which Reynolds stresses are assumed to be proportional to the gradient of the average velocity, with a proportionality constant representing the turbulent viscosity. This hypothesis, known by the name the assumption of "Boussinesq" provides the following expression for the stress tensor Reynolds [8]:

$$\overline{\rho u_i' u_j'} = \rho \frac{2}{3} k \delta_{ij} - \mu_t \left(\frac{\partial u_i}{\partial x_j} + \frac{\partial u_j}{\partial x_i} \right) + \frac{2}{3} \mu_t \frac{\partial u_i}{\partial x_i} \delta_{ij} \quad (6)$$

Here it is the turbulent kinetic energy defined by:

$$k = \frac{1}{2} \sum_i \overline{u_i'^2} \quad (7)$$

Eddy viscosity is obtained by assuming that it is proportional to the product of the scale of the turbulent velocity and length scale. In (k-ε) model,

these scales velocities and lengths are obtained from two parameters k and the kinetic energy dissipation rate. So can express by the following relation:

$$\mu_t = \rho C_\mu \frac{k^2}{\varepsilon} \quad (8)$$

With: $C_\mu = 0,09$ (empirical constant).

k values and ε required in the equation are obtained by solving the following conservation equation:

$$\begin{aligned} \frac{\partial}{\partial t}(\rho k) + \frac{\partial}{\partial x_j}(\rho u_j k) &= \frac{\partial}{\partial x_j} \left(\left(\mu + \frac{\mu_t}{\sigma_k} \right) \frac{\partial k}{\partial x_j} \right) + G_k + G_b - \rho \varepsilon + S_k \\ \frac{\partial}{\partial t}(\rho \varepsilon) + \frac{\partial}{\partial x_j}(\rho u_j \varepsilon) &= \frac{\partial}{\partial x_j} \left(\left(\mu + \frac{\mu_t}{\sigma_\varepsilon} \right) \frac{\partial \varepsilon}{\partial x_j} \right) + G_{1\varepsilon} \frac{\varepsilon}{k} (G_k - C_{3\varepsilon} G_b) - C_{2\varepsilon} \rho \frac{\varepsilon^2}{k} + S \end{aligned} \quad (9)$$

Such as:

$C_{1\varepsilon} = 1.44$ and $C_{2\varepsilon} = 1.92$: empirical constants.

$\sigma_k = 1.0$ and $\sigma_\varepsilon = 1.3$: numbers of Prandtl for k and ε respectively.

S_k and S_ε : are terms for sources k and ε respectively.

G_k : represent the generation of the turbulent kinetic energy due to the average velocities gradient.

$$G_k = \mu_t \left(\frac{\partial u_j}{\partial x_i} + \frac{\partial u_i}{\partial x_j} \right) \frac{\partial u_j}{\partial x_i} \quad (10)$$

G_b : Coefficient generation of turbulence due to the entrainment.

$$G_b = -g_i \frac{\mu_t}{\rho \sigma_h} \frac{\partial \rho}{\partial x_i} \quad (11)$$

Domain Calculating and Mesh

The computational domain is divided into a number of volumes called no superposed control volume such that each volume surrounding each point of the mesh. The differential equation is integrated for each volume control and the result of this integration gives the discrete equation expressed using the values of the function ϕ (scalar quantity) for a set of grid points. The discrete

equation obtained expresses the principle of conservation for ϕ on the volume control in the same manner that the differential equation expressed for an infinitesimal volume control [9].

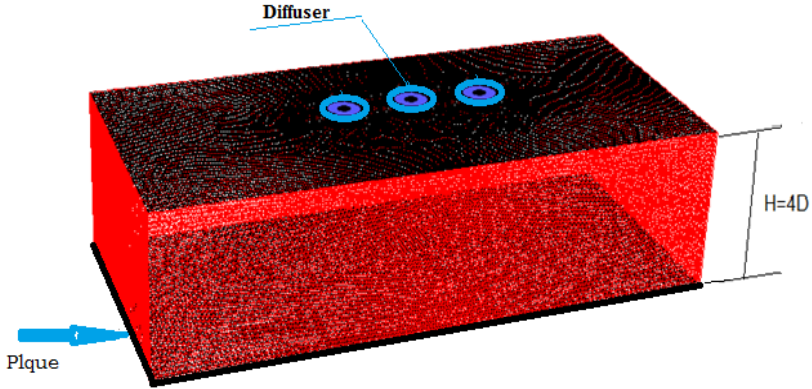


Figure 4: Domain calculating and mesh geometry for three diffusers with hauteur of impact $4D$

Calculations were tested on various meshes for the control of the solution, in order to seek the limit of the independence of the solution compared to the fineness of the mesh, with meshes of tetrahedral form, a number of 865421 cells and a number 166655 nuds. We can therefore conclude that the mesh is acceptable and the solution is independent of the mesh. An entry condition for the pressure outlet type diffuser, with an entry speed of $U = 10 \text{ ms}^{-1}$, and a temperature $T_0 = 363 \text{ °K}$, a hydraulic diameter $D_{\text{hyd}} = 0.047 \text{ m}$, the Reynolds number $Re = 30,000$. At the exit, a pressure outlet type condition is set. The plate having dimensions of $450 \times 100 \text{ mm}$.

Numerical Results

Reduced Temperature Profiles and Reduced Velocity Profiles

We will present the results, reduced temperature profiles Tr and mean velocity profiles dimensionless Ur , depending on the ratio r/D in Figure 5 and Figure 6 for a single jet in relation to a height of impact $H = 4D$.

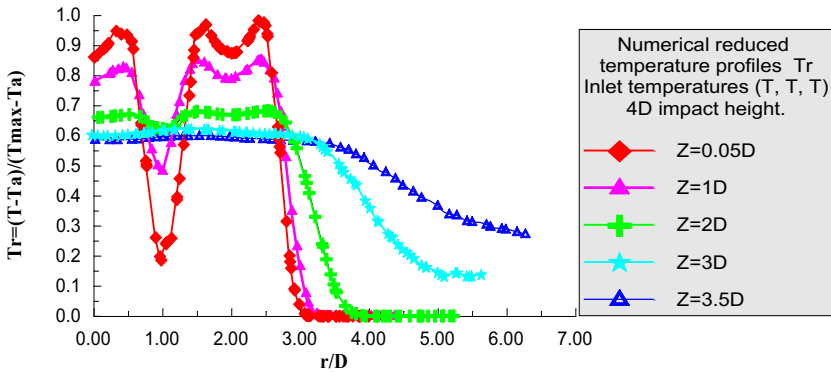


Figure 5: Profiles of the reduced temperature for a swirling turbulent jet with height impact 4D

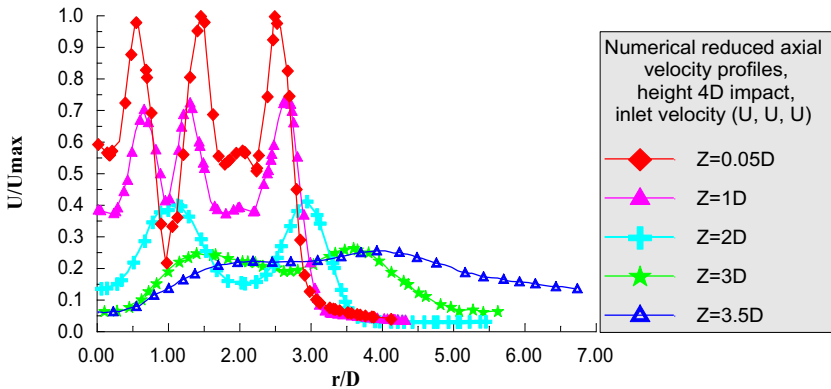


Figure 6: Profiles of the reduced velocity for a swirling turbulent jet with height impact 4D

We note that the curves of temperatures and velocities diminish maximum amplitude potential heart level jet (close to the blowing port), to low amplitudes near the impact region. The reduced temperature tends towards the ambient temperature T_a , downstream of the jet. The mean velocity dimensionless U_r diminishes as one moves downstream and becomes almost parallel to the plate. Thus, the single jet has a low sprawl.

The increase in temperature and speed for $r / D > 3$ represents the deflection of the fluid on the impact surface in the radial direction.

Profiles of the Nusselt Number, Nu

The Nusselt number characterizes the heat transfer from the impinging jets. It is a dimensionless number that quantifies the heat transfer between a fluid and a wall of the baffle plate. It represents the ratio of convective exchanges on conductive exchanges [10].

$$Nu = \frac{h.D_{hy}}{\lambda} \quad (12)$$

Such as:

h : Local convective heat transfer coefficient [W.m⁻².K⁻¹]

λ : The thermal conductivity of air, taken at the reference temperature [W.m⁻¹.K⁻¹]

D_{hy} : hydraulic diameter [m]

As a general rule, the heat transfer correlations in this regime are described by the following equation:

$$Nu = C . Re^m . Pr^n \quad (13)$$

The constants C , m and n depend on the geometry of the jet and the geometry of the impact surface. The dimensionless numbers of Nusselt (Nu), Reynolds (Re) and Prandtl (Pr) take into account the thermo-physical properties of the fluid at its temperature at the nozzle outlet. Thermo physical properties are estimated at the temperature of the impinging jet.

Table 1: Correlations in the flow area

Authors	Flow regime	C	m	n	Reynolds values
McMurrall et al. (1966)	Laminar	0.75	0.5	0.33	3.10^5
	Turbulent	0.037	0.8	0.33	3.10^5
Vader (1988)	Laminar	0.89	0.48	0.4	$100-3.10^5$
Robidou (2000)	Laminar	0.81	0.53	0.4	$5000-6000$
Kouachi	Turbulent	0.042	0.78	0.33	$104-10^5$

According to, Me Murray et al. [11] for a turbulent flow $C = 0.037$, $m = 0.8$ and $n = 0.33$. From where:

$$Nu = 0.037 Re^{0.8} (Pr)^{0.33} \quad (14)$$

Re is the Reynolds number. It is defined by:

$$Re = \frac{\rho \cdot U \cdot D_{hy}}{\mu} \quad (15)$$

Where;

ρ : density of air [kg.m⁻³]

U : average velocity [m.s⁻¹]

D_{hy} : hydraulic diameter [m]

Pr : Prandtl number is a dimensionless number; it represents the ratio of momentum diffusivity and thermal diffusivity.

$$Pr = \frac{\mu \cdot Cp}{\lambda} \quad (16)$$

μ : dynamic viscosity [N.s.m⁻²]

Cp : specific heat [J.kg⁻¹.K⁻¹]

λ : air thermal conductivity en [W.m⁻¹.k⁻¹]

Figure 7 shows the superposition of the Nusselt Nu number profiles, whose impact height is $H = 4D$, for an inlet velocity in the diffusers (U , U , U) and an inlet temperature (T , T , T). Initially, the Nusselt profiles indicate peaks at the blast port and disturbances. These disturbances are due to the support of the fins. Amplitudes and disturbances decrease progressively as we move downstream of the jet. At station $Z = 3.5D$, the number of Nusselt is moderate at the level of impact surface ensuring homogenization of heat transfer plate.

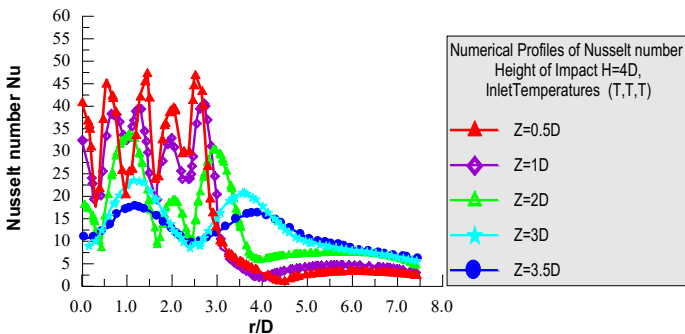


Figure 7: Profiles of the Nusselt number Nu depending of the dimensionless distance r/D

Temperature field and velocity vectors

Figure 8 illustrates the temperature and velocity vector field in the (y, z) plane of a three-jet system, for an impact height $H = 4D$, relative to an input temperature distribution (T, T, T) . Note that it has symmetry with respect to the z -axis. The potential cone is uniform for all three jets; the distribution of the temperature field is well balanced over the entire domain. For the velocity field in the impact region, a deflection zone appears, so that the velocities change from the axial direction to the radial direction.

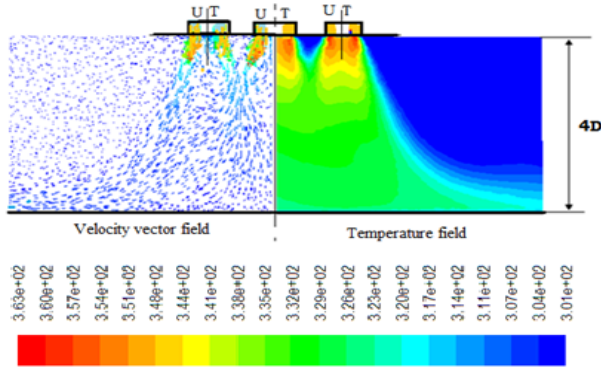


Figure 8: Temperature field and velocity vectors

Figure 9 shows the temperature field lines being symmetrical with respect to the main axis of the jet, an entire and balanced propagation of the heat transfer over the entire domain, the temperature reaches the entire surface of the plate, which favours homogeneity thermal transfer over the entire surface of the plate.

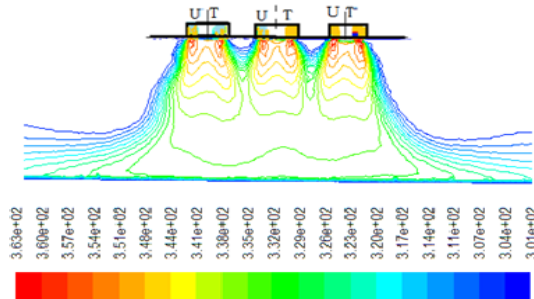


Figure 9: Temperature field lines

Figure 10 shows the contours temperature fields on the wall of the heated plate by a system of three jets impacting the plate at a height $H = 4D$, with the inlet temperatures of the diffuser (T, T, T). It should be noted that in the figure this distribution of the temperature field is distributed symmetrically and almost over the entire surface of the plate. Thus, it promotes the homogeneity of the heat transfer over the entire surface of the plate.

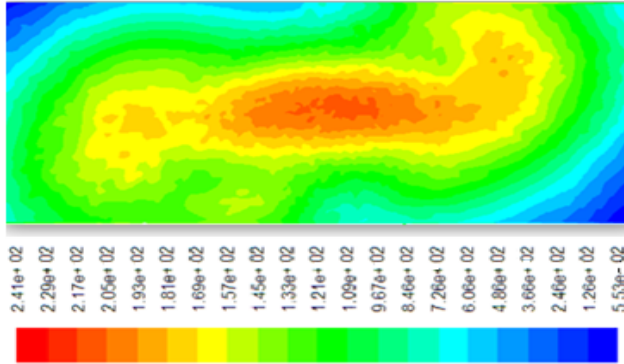


Figure 10: Contour temperature field of the plaque

Validation of Results

The quality of comparison between the numerical results and experimental results comparison is evidenced in Figures 11 on the inlet temperature T_r , at the reduced velocity U_r in the (y, z), respectively. The numerical results of the model with two transport equations (K- ϵ) used to simulate this case, are in good agreement with experimental results. However a smaller gap in the first station. The model (K- ϵ) considers an isotropic turbulent viscosity.

Without omitting the influence of uncertainties of measurements operated on. Despite the shortcomings, the model (K- ϵ) gave acceptable results qualitatively. Nevertheless, it is a relatively simple and inexpensive simulation tool.

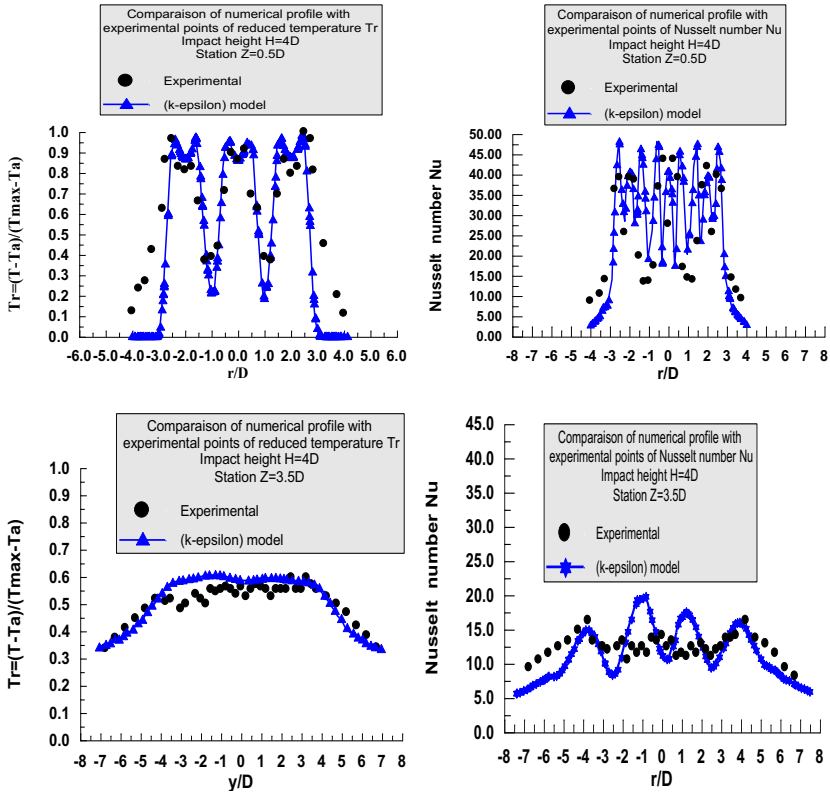


Figure 11: Comparison of numerical and experimental profiles of the reduced temperature Tr and Nusselt number for stations (0.5D and 3.5D) in the (r, z) , with height of impact 4D

Conclusion

The results of this study show that initially, the resulting jet has the same characteristics as a free jet. Near the obstacle that it undergoes a considerable deviation characterized by the weakening of the speed and the development of the jet (With the temperature and velocity amplitudes decreasing as one approaches the plate). In contact with the plate, the temperature and velocity curves are almost parallel to the plate. The velocities change direction and would grow radially. The swirling ensures a uniform distribution of the heat with a complete diffusion of the jet. It slows the fluid particles and promotes better jet development to provide better heat transfer and uniform temperature

distribution along the plate. The presence of the plate decreases the differences in the temperature of the jet, the temperature of the plate decreases gradually downstream of the jet as one approaches the plate. The number of Nusselt is moderate at the impact surface level ensuring homogenization of heat transfer plate. The comparison between the numerical results and the experimental results presented in this study indicates that the model with two equations of transport (K-) has produced satisfactory results. Despite the weaknesses of this model, the latter has given acceptable results on the comparison plan. It remains a relatively simple and inexpensive simulation tool to use.

References

- [1] P. Reulet, R. Phibel, P. Grenard, "Comparison calculations experiments on the cooling impact of subsonic jets," SFT day, March 9. 16. Paris, 2006.
- [2] R. Viskanta, "Turbulent flow in the near field of a round impinging jet", *International Journal of Heat and Mass Transfer* 54(23), 4939-4948 (2011).
- [3] A. Zerrouk, A. Khelil, L. Loukarfi, "Numerical study of a three swirling jets system impacting a plane plate", *Control Laboratory, Test, Measurement and Mechanical Simulation, University of Chlef, Algeria, Journal of Mechanics & Industry* (2016).
- [4] A. K. Gupta, D.G. Lilley, N. Syred, "Swirl flows", London: Abacus Press (1984).
- [5] Y. Huang, V. Yang, "Dynamics and Stability of Lean-Premixed Swirl-Stabilized Combustion", *Progress in Energy and Combustion Science*, 35 (4), 293-364 (2009).
- [6] H. Saato, M. Mori, T. Nakamura, "Development of a Dry Ultra-low NO_x Double Swirler Staged Gas Turbine Combustor," *Journal of Engineering for Gas Turbine and Power*. January 120, (1998).
- [7] M. Braikia, L. Loukarfi, A. Khelil, and H. Naji, "Improvement of thermal homogenization using multiple swirling jets," *Université Lille Nord de France, Thermal Science* 16 (1), 239-250.
- [8] B.E. Launder, D.B. Spalding, "Mathematical models of turbulence", *Dept of Mechanical Engineering, Imperial Collogue of Science and Technology, London. England* (1972).
- [9] Dimh. Vo. Ngoc, Dinh. Vo. Ngoc, "Numerical methods of local integral on finite volumes", *School of Engineering, University of MONCTON. CANADA* (1989).
- [10] G. Wigley, J.A. Clark, "Heat transport coefficients for constant energy flux models of broad leaves", *Boundary Layer Meteorology* 139-150 (1974).

- [11] D.C. Mc Murray, P.S. Myers, O.A. Uyehara, “Heat Transfer Conference”, in proceeding 2, 292 (1966).
- [12] FLUENT User’s Guide, 2006.

Study on Drag Coefficient (C_D) Value of Low-Energy Prototype Class Car

J. Jodiputra, S. Tobing*, H. Gunawan,
Mechanical Engineering Department
Faculty of Engineering, Atma Jaya Catholic University of Indonesia
Banten, Indonesia

*sheila.tobing@atmajaya.ac.id

M.G. Andika

National Laboratory for Aerodynamics, Aeroelastics, and Aero-Acoustics
Technology, The Agency for Assessment and Implementation of Technology
(BPPT), Banten, Indonesia

ABSTRACT

Researches on car design are closely related to the field of aerodynamics. The design was done to minimize the drag force. The experimental method was only used for testing the initial design and the final design. Improvement and modification were done by using the CFD simulation. The experiments were done using the Low Speed Wind Tunnel (LSWT) owned by the National Laboratory for Aerodynamics, Aeroelastics, and Aeroacoustics Technology. The Reynolds number ranged from 505,225 to 671,528. The research began with the initial design called JM-5, tested in the LSWT. Modifications were done throughout the research to achieve the lowest drag coefficient value. In the end, JM-4v2 became the final design with the lowest drag coefficient value of 0.202.

Keywords: Low-energy prototype class car, Coefficient of drag, Low Speed Wind Tunnel, CFD; KMHE car

Nomenclature

C_D	Drag coefficient value
CFD	Computer Fluid Dynamic
JM-5	Model of JM-5
JM-4	Model of JM-4

LSWT	Low Speed Wind Tunnel
Re	Reynolds number
S	Sectional frontal area
V	Velocity

Introduction

Kontes Mobil Hemat Energi (KMHE) is a competition organized by Direktorat Jenderal Pendidikan Tinggi (DIKTI) on a national scale and followed by many universities in Indonesia. This competition aims to support the creativity of many students from various institutions or universities in creating a low-energy car. The low-energy car in KMHE divided into two classes, namely urban class and prototype class. Prototype class cars are required to have a design that can minimize energy consumption so that it can go as far as possible [1]. Factors affecting energy consumption in energy-efficient cars are shown in Figure 1. This study focused on examining the effect of aerodynamics on the energy consumption of a low-energy prototype class car [2].

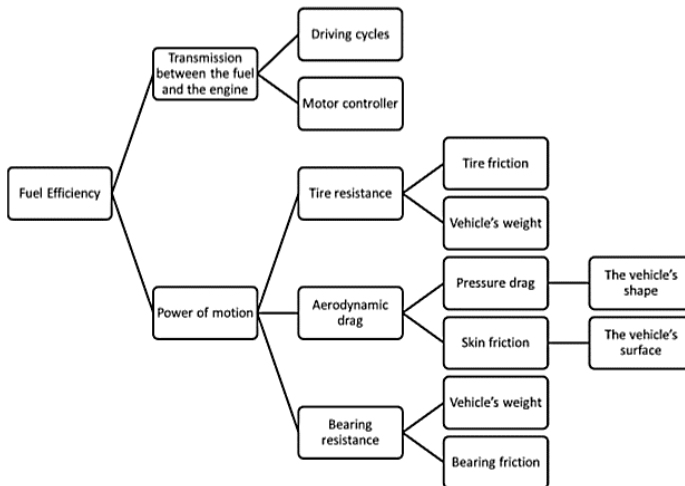


Figure 1: Factors affecting the energy consumption of low-energy car [2]

Aerodynamic studies of drag coefficients were done by Eugene from Mapua Institute of Technology Philippines. Team Cardinals 2012 successfully created a low-energy prototype class car, named Aguila. Aguila's body was built with a length of 2.59 m and a frontal area of 0.32 m² (without wheels).

Through simulation done on CATIA V5 software, Aguila showed a drag coefficient value of 0.3 within a constant velocity of 16.67 m/s (equal to 60 km/h). The simulation was conducted only on the car body without considering the effects of the wheels. The team participated in the Shell Eco-marathon Asia race in 2012 [3].

Aerodynamic studies were also conducted by Danek, a student of the Silesian University of Technology in Poland. Danek conducted an aerodynamic study on a low-energy prototype class car called MuSHELLka. MuSHELLka had a length dimension of 2.75 m with a frontal area of 0.297 m² (including wheels). The open-wheel configuration was applied to the front wheels which were located outside the body. Through simulation done in software ANSYS CFX, MuSHELLka showed a drag coefficient value of 0.255 within a constant velocity of 9.72 m/s (equal to 35 km/h). Unlike the previous literature, MuSHELLka simulation was done with the wheel-mounted, like the real one. MuSHELLka raced in the Shell Eco-marathon competition in 2012 and finished in the 10th position [4].

Things were slightly different from the simulation conducted by Abo-Serie from Konya Mevlana University in Turkey. They simulated the low-energy prototype class car called Eco-Rumi with a wheel enclosed by a disc-shaped cover separated from the body. Eco-Rumi had a length dimension of 2.9 m with a frontal area of 0.265 m² (with a covered wheel). The simulation of aerodynamics was done by using STAR CCM+ software and showed a drag coefficient value of 0.127 within a constant velocity of 7.3 m/s (equal to 26,28 km/h) [5].

Like MuSHELLka, Cieslinski from the Lodz University of Technology conducted an aerodynamic study on different cars, Eco Arrow Prototype 3. Eco Arrow Prototype 3 had the same open wheel configuration as MuSHELLka. Eco Arrow Prototype 3 had a length of 3.1 m with a frontal area of 0.25 m² (with open wheels). When fairing was used as a wheel cover, the frontal area became 0.27 m². Eco Arrow Prototype 3 car simulation was done by using ANSYS FLUENT software with two different conditions: with the fairing and without the fairing. As a result, the car with fairing showed a lower drag coefficient value of 0.182, while the other one without fairing showed a drag coefficient value of 0.197 [6].

Similar to Aguila, a CFD simulation conducted by Joshua also focused on the car's body. He used Antawirya Turangga Veda as the initial model (built by the Antawirya team, University of Diponegoro) and Antawirya Turangga Veda II as the final model. Changes were made on the front and rear sections of the car. He modified the front and rear sections of the car with narrower design. The simulation ran on four velocities variables and the Reynold numbers ranged from About 19% decrement of C_D value was obtained from 0.262 to 0.213 [7].

Methodology and setup

This study used two types of testing methods: experimental testing and CFD. Experimental testing was conducted by using Low Speed Wind Tunnel (LSWT) owned by National Laboratory for Aerodynamics, Aeroelastics, and Aeroacoustics. An experimental test was only performed on the initial and final model, while CFD was done in between. CFD was conducted for the development and improvisation of the model design to produce the lowest drag coefficient value. All models used in the experimental testing were made by using 3D printers with PLA filament printing material. For CFD, the models were made by using SOLIDWORKS 2015 and the analysis was done by using ANSYS Fluent 17.2. The whole development and improvisation design were also done by using SOLIDWORKS and ANSYS Fluent. This step was carried out to reduce the cost and effort of the research.

Methodology and Model

In this research, the drag coefficient equation was the basic equation. The drag coefficient was a dimensionless value. To be dimensionless, the drag force must be divided against the dynamic pressure multiplied by the frontal area of the model. Equation (1) describes the definition of a drag coefficient. The drag force (F_{drag}) was obtained from the normal pressure (p) and the shear stress (τ) along the surface of the model. Then the dynamic pressure was generated by the relative speed of the airflow against the model and had a constant magnitude along with the model [8].

$$C_D = \frac{F_{\text{drag}}}{\frac{1}{2} \rho V^2 A} \quad (1)$$

“ ρ ” was the density (kg/m^3) and “ V ” was the fluid flow velocity (m/s). The unit of the dynamic pressure was Newton per millimeter squared (N/mm^2), which is the unit of pressure. “ A ” value was the frontal area of the model's front view. The frontal area was determined from a certain distance measured from the front end of the car body. The area was a front view of the model seen perpendicularly to the direction of the incoming fluid flow. Thus, the frontal area was measured in two dimensions [9].

As mentioned earlier, there were two models: the initial and the final model. The initial model called JM-5 and the final model called JM-4. Both models were shown at all views in Figure 2, Figure 3, and Figure 4. Then, the steps of development and improvisation from the initial model to the final model were described in the following chart in Figure 5.



(a) (b)
Figure 3: Rear view of (a) JM-5 as the initial model, and (b) JM-4 as the final model



(a)



(b)

Figure 4: Side view of (a) JM-5 as the initial model, and (b) JM-4 as the final model



Figure 5: The steps of development and improvisation from JM-5 to JM-4 model

In addition to the force measurement (to get the drag coefficient value), wool tuft visualization was also done to get the visualization of air around the model. This wool tuft visualization was compared to the visualization from the CFD. This step was done to validate all CFD results. The installed wool tuft on each model could be seen in Figure 2, Figure 3, and Figure 4. JM-5 model was painted in a different color to make it look different from the JM-4 model.

Experimental Setup

Low Speed Wind Tunnel was chosen for the experimental testing that used non-aircraft models. The size of the test section was 1.5 m of width and 2 m of length. It supported the 3D printed models with a size of 0.307 m of length, 0.06 meters of width, and 0.048 m of height. The Reynold number ranged from 505,225 to 671,528. In addition, the Reynolds number greater than 500,000 was turbulent flow regimes. Turbulent flow always occurs in reality, thus more and more in line with the events and aerodynamic phenomena in reality.

The scale of the model size was 1:8.1. This scale was set to prevent having a large blockage ratio, which was below 20%. The frontal area of the model (calculated and reviewed on SOLIDWORKS) was 0.00458 m². With the selected model size and test section size at LSWT, the blockage ratio was 1.85%. The blockage ratio was considered low, so it could be ignored. The testing was not interrupted by the size of the test section.

This experimental testing preparation has been done both from modeling to load cell calibration. The position of the model was placed according to Figure 6. Visible model tied with a stem which was then paired using a bolt to the load cell. Because the length of the stem was too short, the load cell position must be elevated to reach the bolt hole in the stem. As a result, the load cell was attached to an acrylic rod and the acrylic rod was clamped by a “C” clamp on the profile beam. In addition to the model, there was also a ground board installed in the test section. Distance from the model to the ground board was as far as 3 mm. This distance was adjusted to make sure that the drag force obtained was not disturbed by the friction between the

model (which was its tire) and the ground board during the test. The ground board was acting as a conveyor replacement, where its function was as the basis of a model and represented the road where the car was moving. However, because the ground board was not moving like a conveyor and the model was made with a fixed wheel that could not rotate, the ground board function was only as a foundation. The ground board position was arranged as seen in Figure 7 (a), while the position of the model has been done with the help of laser alignment as seen in Figure 7 (b).

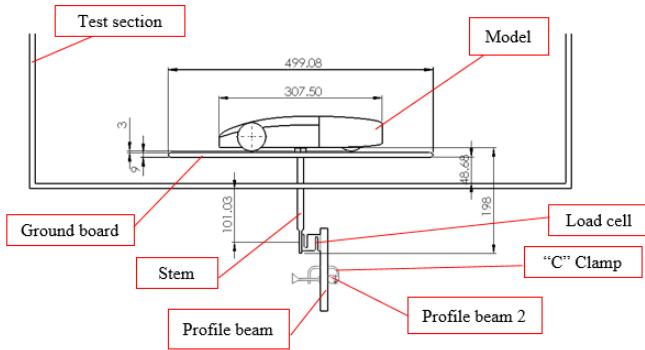
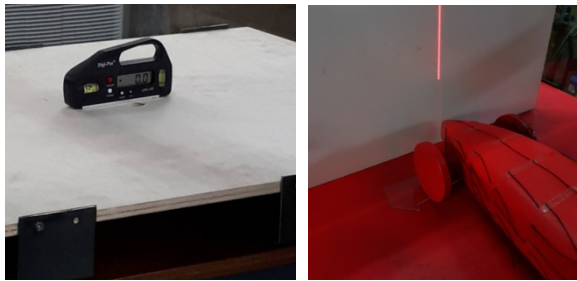


Figure 6: Experimental testing scheme



(a)

(b)

Figure 7: (a) Adjustment of the ground board and (b) alignment of the model by using laser alignment

CFD Setup

CFD simulation was done using ANSYS 17.2 software. The model geometry was made using SOLIDWORKS 2015 software. The model was placed inside two pieces of domain, the primary domain and a smaller domain named car box. Both domains were air. The model was made on a 1:8.1 scale and all sides of the car were used for computing. Detailed display of domain dimensions and placement are shown in Figure 8.

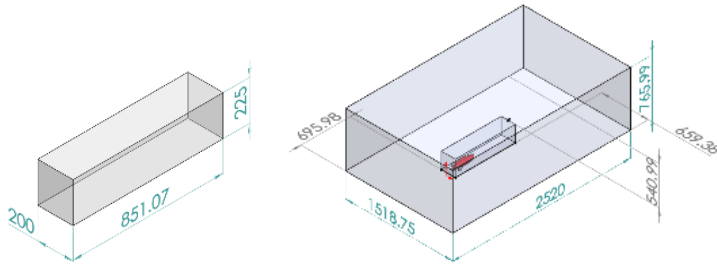


Figure 8: Detail of domain dimensions and placement

The meshing process was done on ANSYS ICEM CFD. Meshing with a tetrahedral form was applied across domains and the model. The total elements generated range from 4 million to 5 million elements. The meshing process is done on sub software ANSYS ICEM CFD. Meshing with a tetrahedral form is uniform across domains and models. The total elements used range from 4 million to 5 million elements. The size of elements used in domains, car boxes, and the model was as in Table 1.

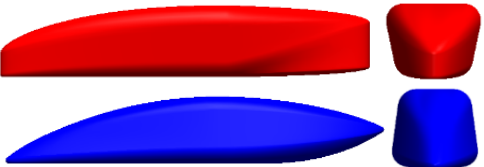
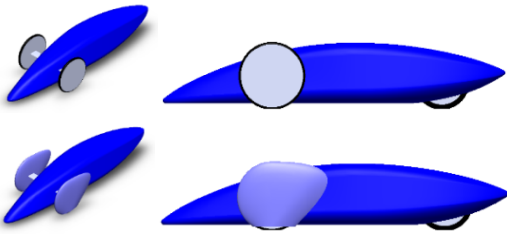
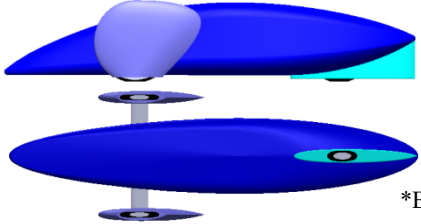
Table 1: Size of element used

Object	Sizing	Size type	Element size
Domain	Global sizing	Element size	Min.: 0.002 m Prox. Min. Size: 0.005 m
Car box	Body sizing	Body of influence	0.005 m
Model	Face sizing	Element size	0.004 m
Model	Inflation	First layer thickness	First layer height: 0.000854 m Max. layers: 10 Growth rate: 1.15

The flow simulation was performed by using Fluent. The simulations were run based on the Navier-Stokes equations under the $k-\omega$ SST turbulent model at a steady state. The air density was assumed to be constant at 1.225 kg/m^3 . The Reynolds ranged from 505,225 to 671,528. The dynamic viscosity was constant at 1.789×10^{-5} .

Table 2 listed the geometries tested in the CFD as a modification from the JM-5 model into a JM-4 model.

Table 2: Geometries tested in the CFD

Geometry	Picture
JM-5 (red) & JM-4 (blue)	
JM-4 with unclosed wheel and closed front wheel	
JM-4 with the closed front wheel and closed rear wheel	

*Bottom view

Results and discussion

Experiment Results for Initial Design

Experimental testing was done by testing in three Reynolds numbers, as shown in Table 3.

Table 3: Result from experimental and CFD testing for JM-5 model

Re	C_D Exp.	C_D CFD	Error
505.225	0,362	0,269	25,69%
557.853	0,375	0,302	19,47%
610.480	0,391	0,341	12,79%

It appears that the higher the Reynolds number, the greater the value of the drag coefficient (C_D). It seemed not aligned with Equation (1), where the higher the speed, the value of the C_D should decrease. It was not wrong if the drag force (F) felt by the object (in this case is that the car body) is constant. However, in this experimental data, this upward trend indicates that as the speed increases, the drag force that felt by the car body was also getting more significant. In other words, the increase in the drag force felt by the car body will be proportional to the dynamic pressure multiplied by the frontal area (A).

It appeared that the error between experimental results and CFD simulation result is quite large. This was due to various factors. The first factor was friction on the surface of the model that could be contributed to the drag force. In the CFD simulation, the type of material is negligible so there was undoubtedly a difference with experimental results. The second factor was the turbulent model on CFD simulation. Turbulence in the real-life could not be modeled 100% identical in CFD simulations. The CFD simulations are limited to the resources of the computer so that turbulence modeling should be simplified. One way to simplify the turbulence was averaging flow fluctuations as applied in the $k-\omega$ SST turbulent model as a member of the RANS (Reynolds Averaged Navier Stokes). The third factor was the occurrence of undesirable moments that happened on the stem that holding the model. When performing the test, the load cell used was only 1 unit and it was located outside of the bottom of the test section. In contrast to the airfoil test using 2 load cells mounted on the left side and the right side outside the test section. With only 1 load cell and long stem length (about 450 mm), there was an unexpected and undesirable moment during the test. This moment was seen in the value of the load cell, the force shall show a positive value (compression), but it showed a negative value. After making some precise arrangements, the negative value was overcome but due to only one load cell was used and the length of the stem, this factor could be still the cause of a significant error.

Wool tuft visualization

Figure 9 shows the wool tuft visualization on the front section of the JM-5 model. In this section, the wool looked not showing any movement. Stating that the steady wool condition was visible from the similarity of wool conditions on the sequence of picture (Figure 9) from left to right. In the absence of vibration and steady wool behavior as well as the direction of this freestream, it could be stated that there had been no point of separation yet and the airflow was still attached and flowing smoothly on the surface of the front section of the JM-5 model. This means that on the front section of the JM-5 model has not seen as the source of the drag force.



Figure 9: Wool tuft visualization on the front section of JM-5 model

In Figure 10, it appears that some of the wool on the middle section of the JM-5 model had started to not be aligned with the freestream direction and some of it was already visible blurred. The wool that not aligned with the freestream indicates the potential for flow to separate, while the blurred wool indicates at that point the airflow had separated from the JM-5 model and resulted in the creation of wakes that could contribute a significant drag force.

Seen in Figure 11, that most of the wool on the rear section of the JM-5 model was blurred. From this blurred look, it could be said that the wool had vibrated and signified the occurrence of airflow separation before reaching the rear end of the JM-5 model. This suggested that the separation point on the back of the JM-5 model occurred too early and would produce large wakes. Wakes occurred in contrast at the rear end of the JM-5 model as shown in Figure 11. It appears that the entire wool is faded and certainly vibrates indicating a large area of wakes occurred behind the JM-5 model.

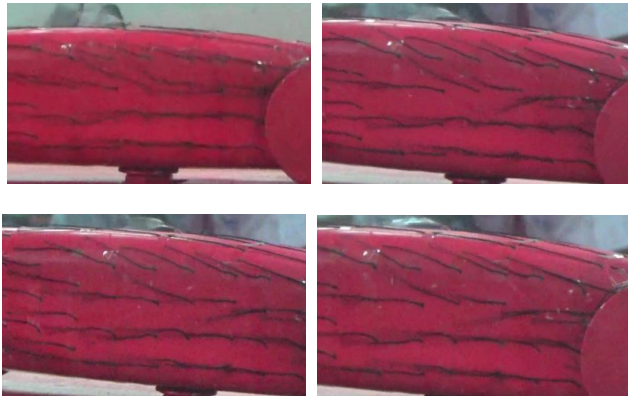


Figure 10: Wool tuft visualization on the middle section of JM-5 model

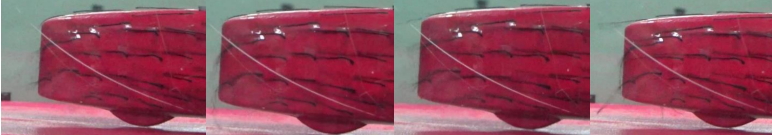


Figure 11: Wool tuft visualization on the rear section of JM-5 model

CFD Simulation

Comparing the body of the models

After knowing the C_D value of the JM-5 model, JM-4 was created as a new model. The JM-4 model had a different length and it affected the Reynold number. In addition to the length, the nose and tail shape of the JM-5 model also changed. The changes were seen in Table 2.

Table 4: Results of JM-5 model and JM-4 model in CFD

Model	Re	C_D CFD	C_D
JM-4	555.748	0,0912	0,170
	613.638	0,167	
	671.529	0,252	
JM-5	505.225	0.104	0,183
	557.853	0.177	
	610.480	0.267	

This section of simulation only analyzes the body of the models (without the wheels). Table 4 showed that the C_D value of the JM-4 model was 7.64% lower than the JM-5 model. This showed that the change in length, the nose shape, and the tail shape on the model JM-5 managed to minimize the drag force. This was consistent with the literature which says that the lower nose shape and smaller tail form could decrease the C_D value [10]. This statement was supported by the visualization from CFD results in Figure 12 and Figure 13.

Figure 12 showed the visualization of static pressure contour on the front section of the JM-5 model and JM-4 model. The red area was the area of static pressure. The static pressure on the front of the model also called the stagnation point and could inhibit the car's movement as it contributed to the drag force. It was clear that the red area on the front of the JM-5 model was more significant than the JM-4 model. It was stated that the significant pressure on the front of the JM-5 model contributed more drag force so that the C_D value would increase. Aside from the stagnation point, the cause of the drag force was wakes that occurred behind the model. Wakes occurred because of the

drastic difference in pressure resulting in a gradation of adverse pressure, creating a vacuum effect on the rear section of the car. In Figure 13, wakes were marked with a blue area. It appeared that the wakes on the JM-5 model weremore extensive than the JM-4 model. The wakes area on the JM-5 model was more extensive because the shape of the tail of the JM-5 model was larger than the JM-4 model. With a larger tail, the lower-pressure region at the rear of the model got bigger. The enlargement of the lower pressure region increased the encounter between the higher pressure and the lower pressure so that the wakes region gets bigger. From these two visualizations, it could be stated that the JM-5 model had a more significant drag force than the JM-4 model, so the JM-4 model had resulted in lower C_D value. Thus, the JM-4 model was chosen to be modified further.

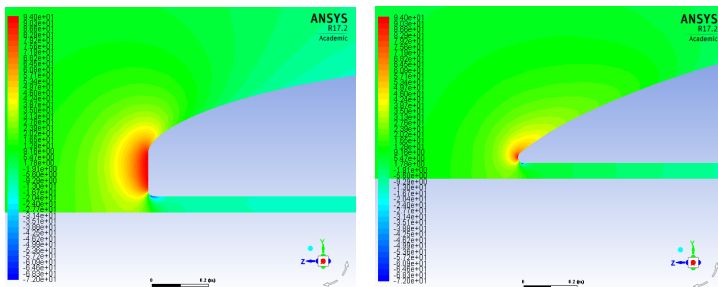


Figure 12: Contour of static pressure on the front section of JM-5 model (left) and JM-4 model (right)

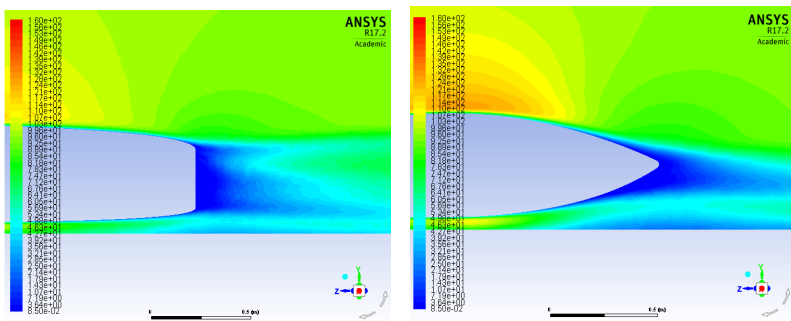


Figure 13: Contour of dynamic pressure on the rear section of JM-5 model (left) and JM-4 model (right)

Front wheel cover

The simulation results in Table 5 showed that the design of the car with the front wheel that had been covered successfully produced a lower C_D value of 0.243. The covered front wheel successfully decreased the C_D value by 13.67% before the front wheel was closed. This indicated that the use of a cover on the front wheel had a significant role in reducing the C_D value.

Table 5: Results of the JM-4 model with the uncovered front wheel and covered front wheel

Front wheel	Re	C_D CFD	C_D
Uncovered	555.748	0.165	0.291
	613.638	0.283	
	671.529	0.424	
Covered	555.748	0.155	0.256
	613.638	0.243	
	671.529	0.369	

The contour of dynamic pressure shown in Figures 14 and Figure 15 illustrated the comparison between the uncovered and covered front wheels. It could be seen that in Figure 14 there was a shrinkage of wakes region when the wheel was covered. The shrinkage of the wake area was more visible from the top view, as in Figure 15. The shrinkage of the wake area had successfully reduced the C_D value by 13.67% from the uncovered wheel. The wakes area was minimized due to the shape of the cross-section of the cover that resembles airfoil (viewed from the top view).

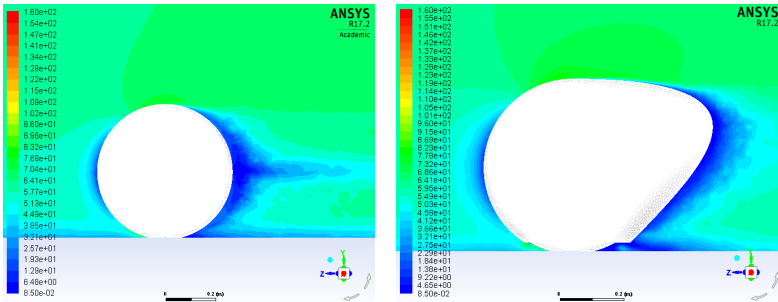


Figure 14: Contour of dynamic pressure on the uncovered front wheel (left) and covered front wheel (right) from the side view

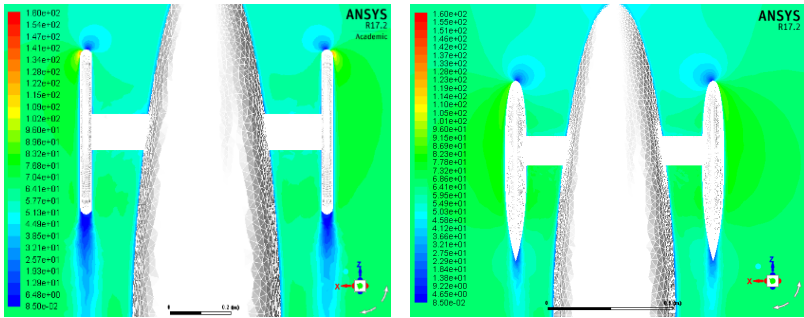


Figure 15: Contour of dynamic pressure on the uncovered front wheel (left) and covered front wheel (right) from the top view

Rear wheel cover

Table 6 showed the simulation results of the effect of the rear wheel cover on decreasing the C_D value. It shall be noted that the uncovered rear wheel condition was already covered front wheel and the rear wheels had not been covered. This means that the C_D value on the uncovered rear wheel was the same as the covered front wheel in the previous section. The simulation results in Table 6 showed that the rear wheel cover successfully decreased 26.73% of the C_D value in the JM-4 model. This indicated that the use of the rear wheel cover had the same role as the front wheel cover in terms of reducing the C_D value.

Table 6: Results of the JM-4 model with the uncovered rear wheel and covered rear wheel

Rear wheel	Re	C_D CFD	C_D
Uncovered	555.748	0.155	0.256
	613.638	0.243	
	671.529	0.369	
Covered	555.748	0.168	0.202
	613.638	0.201	
	671.529	0.236	

By installing the rear wheel cover, the area of the wake was minimized successfully. It could be seen in Figure 16 that the wakes region was minimized by delaying the encounter between the higher-pressure stream and the lower pressure, which becomes the outset of wakes. Following the results of the previous test, the cross-sectional shape of the rear wheel cover was also made to resemble an airfoil to minimize the drag force. This proved successful because the area of the wake had been narrowed down, shown in Figure 17.

Thus, the rear wheel cover was recommended for installation to minimize the value of the C_p .

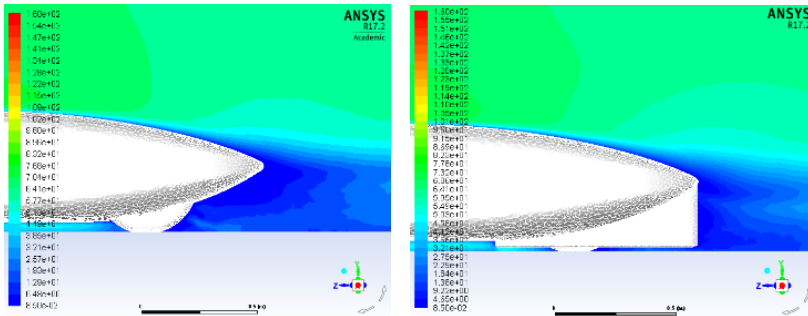


Figure 16: Contour of dynamic pressure on the uncovered rear wheel (left) and covered rear wheel (right) from the side view

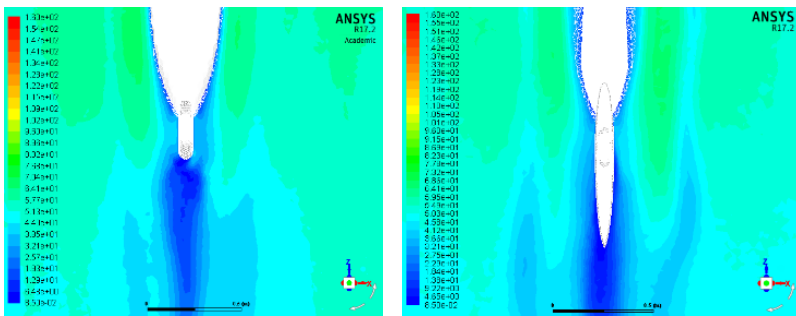


Figure 17: Contour of dynamic pressure on the uncovered rear wheel (left) and covered rear wheel (right) from the side view

Experiment Results for Final Design

The final design in this research was the JM-4 model that had been installed front wheel cover, and rear wheel cover. So, this final design was named the JM-4 v2 model. Table 7 showed the results of experimental testing on the final design. It appeared that the value of the C_D was still increasing as the Reynolds number increased. Although the error was quite large, but this upward trend was still in accordance with the CFD simulation had done. The cause of the error had been discussed in the previous sections.

Table 7: Result from experimental and CFD testing for JM-4 model

Re	C_D Exp.	C_D CFD	Error
555.748	0,276	0.168	39.13%
613.638	0,283	0.201	28.98%
671.529	0,290	0.236	18.62%

Wool tuft visualization

Figure 18 showed the wool tuft visualization on the front section of the JM-4 v2 model. It appeared that the whole wool behavior seen on the front of the JM-4 v2 model was still steady and parallel with the freestream. It was also noticed that there was no vibrated wool caused by airflow. Steady wool behavior and no vibrated wool indicated that there had been no separation point and the airflow still attached to the surface of the front section of the model. Thus, in this section, there was no significant drag force yielded yet.

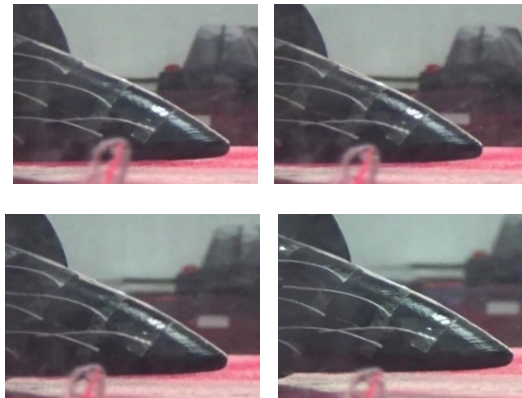


Figure 18: Wool tuft visualization on the front section of the JM-4 v2 model

The difference between the JM-4 v2 model with the JM-5 started from the middle section to the rear section. In Figure 19, it appeared that the wool on the middle section of the JM-4 v2 model was not blurred. This showed that the wool was still steady and showed the airflow still attached to the surface of the body, so it is called the attached flow. In addition, it appeared that the wool was still parallel with the direction of the freestream which indicated that airflow on the middle section of the JM-4 v2 model had not occurred separation and not resulted in a significant drag force.

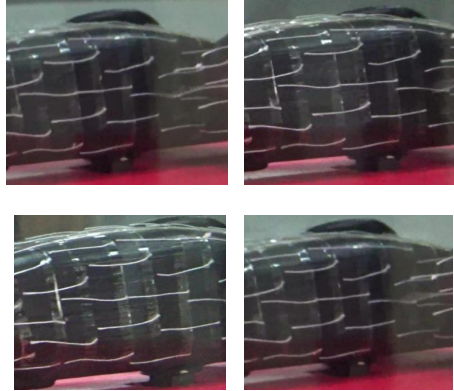


Figure 19: Wool tuft visualization on the middle section of JM-5 model

Figure 20 showed that the wool behavior on the rear section of the JM-4 v2 model was still steady. The wool started to blur at the rear end of the JM-4 v2 model. From this, it could be ascertained that the wool had been vibrated. The wool located at the rear of the model (before the rear end of the model) showed the location of the separation point that became the beginning of the wakes. The area of wakes on this visualization was not fully visible because the area of the wake lay from the rear end of the model until it was completely separated from the model (towards the back). So, wool tuft visualization was only to show the early phases of wakes or when the wool at the end of the model looks blurry or vibrating.

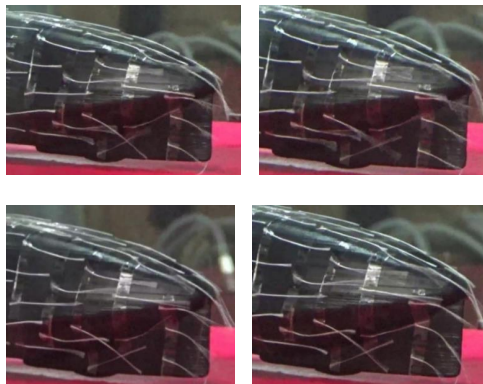


Figure 20: Wool tuft visualization on the rear section of JM-5 model

When comparing the wool tuft visualization between the JM-5 model and the JM-4 v2 model, it was clear that the JM-4 v2 model had better wool tuft behavior than the JM-5 model. This was seen from the middle of both models, where the wool on the JM-5 model had started to vibrate while the JM-4 v2 model did not. Then continue to the rear of the model where the difference was noticeable, that the wool on the JM-5 vibrated more than on the JM-4 v2 model. From the comparison of visualization and CFD result data, it can be stated that the design of JM-4 v2 is the final design with a C_D value of 0.202.

Conclusion

This study was successfully conducted in both experimental and CFD. Both methods showed the aerodynamic phenomenon with their own unique visualization. The experimental method used the wool tuft to visualize whether and where the separation between airflow and the surface of the body occurred, which was create wakes and therefore created drag force. Wool tuft will vibrate to indicate where the separation occurred. This vibration of the wool tuft began at the middle of the models and continue along the body until at the rear end of the models. CFD method used colors to visualize the pressure difference in all sections required. Pressure difference could lead to a stagnation point and separation point. Stagnation point occurred on the front section of the models and separation point occurred between the middle section of the models until the rear end of the models.

Designing the shape of a car body was crucial in order to reduce the C_D value, especially for low-energy prototype class cars, which was the object of this study. Begin with the front section of the car, the best shape achieved at this study in order to reduce drag was the lower nose shape. At the rear, the best shape was a smaller tail form. Both shapes were applied to JM-4 and successfully contributed 7.64% in drag reduction compared to the initial design. The front and rear wheel of the car also contributes to the creation of drag so it should be covered. The covered front wheel contributed 13.67% from the uncovered front wheel, while the covered rear wheel contributed 26.73% from the uncovered rear wheel in an attempt to reduce drag. Overall, this study obtained the lowest C_D value of 0.202 on the final design (JM-4 v2).

Acknowledgment

The authors would like to acknowledge the help and support of the National Laboratory for Aerodynamics, Aeroelastics, and Aeroacoustics Technology, Research Center for Science and Technology.

References

- [1] KMHE committee, Tentang KMHE. [Online]. Available: <http://kmhe2017.its.ac.id/info>. [Accessed: Oct. 14, 2017].
- [2] J. J. Santin, C. H. Onder, J. Bernard, D. Isler, P. Kobler, F. Kolb, N. Weidmann, L. Guzzella, *The World's Most Fuel Efficient Vehicle: Design and Development of PAC CAR II*, 1st ed. Zurich: vdfHochschulverlag, 2007. [Online].
- [3] F. Eugene, *Development of An Aerodynamic Carbon Fiber Vehicle Body for Shell Eco-Marathon 2012 Prototype Category*, Mapua: Mapua Institute of Technology, 2012.
- [4] W. Danek, "Determination of The Drag Coefficient High Performance Electric Vehicle," *Modelowanie Inzynierskie* (1), 36-41 (2013).
- [5] E. Abo-Serie and E. Oran, "Aerodynamic Considerations for A Low Drag Shell Eco-Marathon Competition Car," *International Conference on Automation and Mechatronics Engineering (ICAME)* 2016.
- [6] A. Cieśliński, W. Prym, M. Stajuda, D. Witkowski, "Investigation on Aerodynamics of Super-Effective Car for Drag Reduction," *Mechanics and Mechanical Engineering* (20), 295-308 (2012).
- [7] T. S. Utomo and J. S. Jhon S., "Analisis Aerodinamika Body Mobil Hemat Energi Antawirya Residual-Sat Dengan Menggunakan Metode Computational Fluid Dynamics," *Jurnal Teknik Mesin S-1*(5), 50-59 (2017).
- [8] J. D. Anderson, *Fundamentals of Aerodynamics*, 2nd ed. New York: McGraw-Hill Inc., 1991.
- [9] J. Katz, *Race Car Aerodynamics: Designing for Speed*, 2nd ed. Massachusetts: Bentley Publisher, 1995.
- [10] Gillespie, D. Thomas, *Fundamentals of Vehicle Dynamics*, 4th ed. Denvers: Society of Automotive Engineers, Inc., 1992.

Study on the Development of a Quaternary Layer of B_4C - TiB_2 - Al_3Ti - Al in AA7050 / B_4C Ex-Situ Composite and Influence of Heat Treatment on Mechanical and Wear Properties

Arvind Kumar*, Ram Naresh Rai
Production Engineering Department,
NIT Agartala-799046, Tripura, India.
*Email: arvjha5@gmail.com

ABSTRACT

In the current investigation, AA7050- B_4C composite developed through flux assisted (K_2TiF_6 flux) stir casting method. The FESEM microstructure studies confirm the uniform distribution of the reinforcements. The EDAX analysis confirms the formation of the intermetallic phase of TiB_2 and Al_3Ti across the interface of B_4C particles and the aluminium matrix. The developed composite was heat treatment as per T-6 specifications, and a comparative study has been done on microstructures, mechanical properties and wear properties for as-cast composite (ACC) and Heat-treated composite (HTC). The effect of heat treatment on the microstructure and bond mechanism shows that the B_4C particles are fairly incorporated in the matrix. Ti decomposes and forms quaternary layers of B_4C - TiB_2 - Al_3Ti - Al across B_4C particles. These layers not only prevent the decomposition of B_4C particles into the matrix, also acts as the effective load transfer layers. Consequently, there is an enhancement in tensile strength by 16.4%, hardness by 15.9%, compressive strength by 14.8%, and impact strength by 10.9%. This may be due to the interface strengthening and precipitation hardening mechanism. There is a significant reduction in wear rate and coefficient of friction after heat treatment; this may be due to the improvement in hardness and compressive strength of the composite.

Keywords: AA7050/ B_4C composite; wear; stir casting; K_2TiF_6 flux; ACC; HTC

Introduction

7XXX aluminium alloys are known for their high strength to weight ratio, excellent fatigue strength and appreciable corrosion resistance. These superior properties have made this material suitable for structural components of aircraft and automobiles [1-2]. Nevertheless, these alloys are weak in wear resistance that restricts its application in many potential fields. Metal Matrix Composites (MMC) is the new generation engineered materials that possess the properties of matrix material and ceramic reinforcements. This combination resulted in unique mechanical properties such as high specific strength, elastic modulus, toughness and wear resistance [3]. Composite materials are highly demanded materials for automobiles and aerospace. The liquid metallurgical techniques of developing composite have some significant advantages such as simplicity, economical and manufacturing of intricate components [4]. Boron carbide (B_4C) is one of the sturdy materials (3700 HV), exhibits the high degree of chemical stability, efficient thermal properties, low density (2.52 g cm^{-3}) and high elastic modulus of 427 GPa [5,6]. Besides these remarkable properties, B_4C lacks its wettability with aluminium below 1100 °C. Several efforts were put forward by many researchers to improve the wettability of B_4C by adding the same reacting agents such as K_2TiF_6 , $KCl-KF$, Mg , Zr , and Ti into the molten matrix. The addition of K_2TiF_6 has got dual benefits; Ti reacts exothermally with B_4C and makes a strong interfacial bond between B_4C particles and the aluminium matrix [7,8]. The formations of a robust interfacial bond improve the mechanical and wear properties of the composite [9]. Popularly, wear is a phenomenon of progressive damage to the surfaces in terms of material loss or movement of material or by developing cracks on the surfaces caused by relative motion. In the phenomenon of wear, the combined stress of compression and shear occurs in the contact region resulting in plastic deformation [10, 13]. Therefore, the hardness of the materials plays a vital role in wear resistance. Since ceramic particles are hard materials, hence the ceramic reinforced composite have better wear resistance than unreinforced alloys [14]. Mahapatra et al. [15] reported that normal load is the dominant factor for material loss and sliding distance was a significant factor influencing coefficient of friction (COF). Similarly, Ranjith et al. [16] reported that for AA7050 alloy/ B_4C_p/SiC_p hybrid composite wear rate increases with an increase in load and decreases with an increase in sliding speed.

Although, there are numerous research on the Al/ B_4C composite, but the development of Al7050/ B_4C composite, particularly effect of heat treatment on microstructure mechanical properties and wear properties have not been addressed yet. Therefore, the prime objective of this paper is to develop AA7050/ B_4C composite through stir casting method and study the effect of heat treatment on the microstructure, mechanical and wear properties of the composite.

Materials and Methods

Al 7050 alloy (Al-5.8Zn-2.4-Cu-1.9 Mg) used as matrix material chemical composition of the alloy is shown in Table 1 and B₄C particles with mesh size F120 having an average particle size of 106 μm chosen as the reinforcement material. The chemical composition of the B₄C particles listed in Table 2. The presence of B₄C and its size confirmed from SEM and Point EDAX analysis of the particle shown in Figure 1. About 1.3 kg of the wrought Al 7050 alloy melted in an induction furnace as shown in Figure 2. Approximately 7.5 (wt %) of B₄C particles and the exactly similar amount of flux K₂TiF₆ were preheated separately at 400 °C for 2 hours in a muffle furnace and then mixed together. This mixture was introduced into the molten matrix in a free flow manner and continually stirred at 350 rpm for 5 minutes. Hexachloroethane (degasser) was used for degassing the composite melt. Then the complete mixture was poured into the preheated permanent mould at 350 °C and allowed the melt to cool slowly by insulating the mould with glass wool. The as-cast composite was then subjected to solutionising heat treatment at 480 °C to obtain a single-phase supersaturated solid solution followed by cold water quenching. Further, artificial ageing was performed at 120 °C for 24 hours to have controlled the decomposition of the supersaturated solid solution to form finely dispersed precipitates [17].

Table 1: Chemical Composition of Al-scrap alloy

Elements	Zn	Mg	Cu	Si	Fe	Cr	Mn	Al
% (by weight)	5.88	1.9	2.4	0.031	1.095	0.006	0.022	Balance

Table 2: Chemical Composition of B₄C

Elements	B	C	Others	B ₄ C
wt %	76	17	--	95

Tensile and compression test samples prepared as per ASTM E8/E8M and ASTM E9 standards shown in Figure 3(A) and Figure 3(B). Tensile and compression test carried on a universal testing machine with a crosshead speed of 0.5 mm/min. The impact test carried out on Zwick Roell impact tester machine as per ASTM E23-12c standard the test sample is shown in Figure 3(C). Three sets of test samples of tensile, compression and impact test were prepared for both ACC and HTC and the average value of each set is considered for analysis of the result.

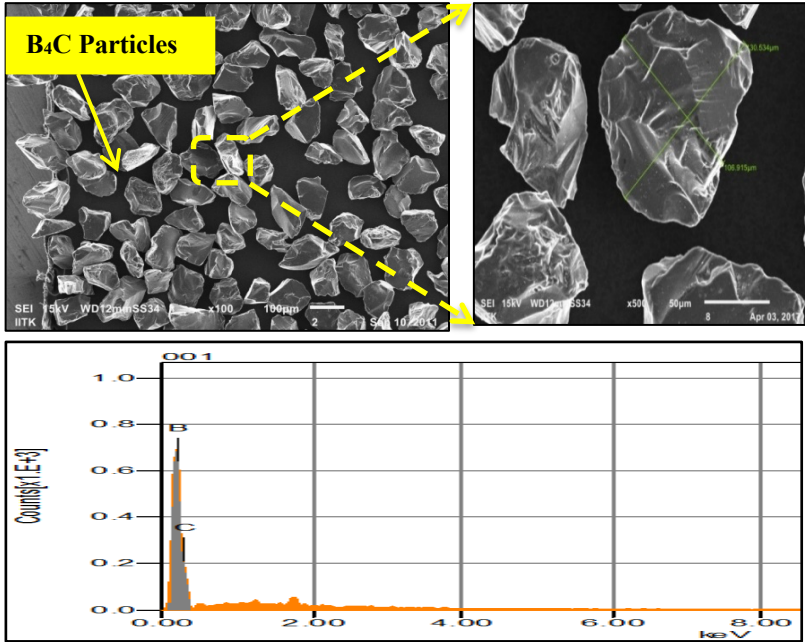


Figure 1: Boron carbide particles

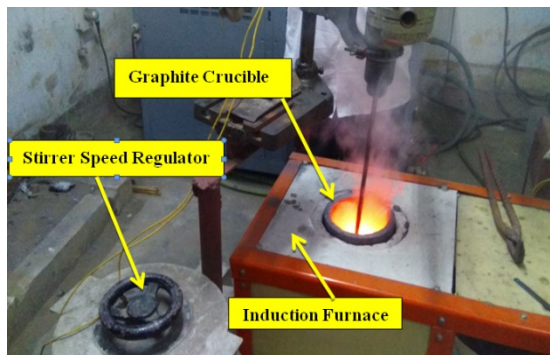


Figure 2: Stir Casting Setup

The hardness of the composite in was measured by Vickers hardness tester as per ASTM E 384, with the applied normal load of 2.5 kgf with a diamond pyramid indenter. Five measurements conducted and the average of these reading considered for reporting the hardness. For microscopic analysis, composite samples were polished and etched by Keller's reagent.

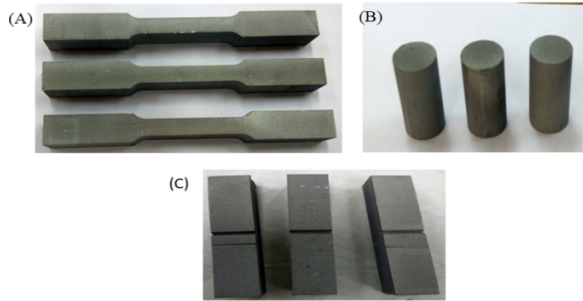


Figure 3: (A) Tensile specimen, (B) Compressive specimen, and (C) Impact specimen

Dry sliding wear tests of the composite were performed on DUCOM TR-20LE Pin-on-Disc tribometer as per ASTM G99 standard. The process parameters opted for the present experiment were normal loads and sliding speed which varies at levels of 10 N, 20 N and 30 N and of 0.5 m/s and 1 m/s respectively. Constant parameters for the wear test were sliding distance 1000 m, room temperature 23 °C and relative humidity of 60 %. The samples for wear test were cylindrical pin of diameter 6 mm and length 27 mm (Figure 4). Three tests conducted for each set of experiment. The test samples thoroughly cleaned with acetone before the test. The responses of the present analysis were wear rate and coefficients of friction (COF). Wear rate evaluated as weight loss of the pin per unit sliding distance. The weight loss of the pin during the wear test measured with a digital weighing machine of accuracy 0.001 g. COF evaluated as a ratio of frictional force to normal load.



Results and Discussions

Microstructure

Figure 5(A) and Figure 5(B) shows the microstructure of ACC and HTC. The microstructures reveal that there is a fair distribution of B_4C in the matrix with less patch of porosity. After heat treatment, the incorporation and distribution of B_4C particles in the matrix enhance (Figure 5B). As can be seen from Figure 5A that the B_4C particles surrounded by Ti agglomerations and B_4C particles clustering also appeared on the matrix surface. Furthermore, after heat treatment it found that the B_4C particles are well incorporated as Ti decomposes and form a clear reaction layer of Ti-bearing intermetallic enveloping the B_4C particles and Al matrix.

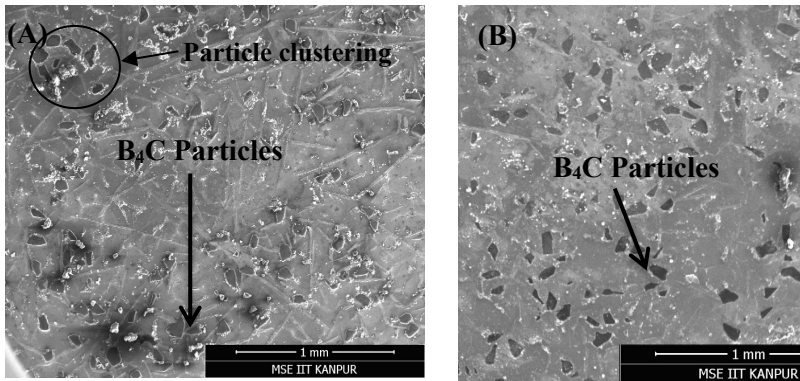


Figure 5: (A) Microstructure of ACC, and (B) Microstructure of HTC

It also seems that the application of K_2TiF_6 flux enhances the interface between B_4C and Al matrixes. These interfaces formed due to the exothermic reaction between Ti and B_4C . Ti has good affinity towards Boron carbide in the presence of molten Al and react exothermally with Boron [7,14]. Due to exothermic reaction, there evolves the enormous amount of heat at the vicinity of B_4C particle, results in local melting of B_4C and form TiB_x , also Ti react with Al and forms Al_3Ti intermetallic compound. Therefore, a quaternary layer of $B_4C-TiB_2-Al_3Ti-\alpha-Al$ is formed as evidence of proper incorporation of B_4C particles in the Al matrix. For the present study FESEM-EDAX line scan as shown in Figure 6 done at the interface, the line starts from $\alpha-Al$ to B_4C particle crossing reaction layer. The line scan across the reaction layer indicates that the aluminium interact with Ti and forms Al_3Ti intermetallic compounds and the Ti line interact with Boron and form a thin layer of TiB_x intermetallic compounds after Al_3Ti . Therefore, the reaction layer comprises of a quaternary layer of $B_4C-TiB_2-Al_3Ti-Al$ at Al- B_4C interface [11,12]. Uniform distribution

and proper incorporation of B_4C particles in the matrix, enhances the load-bearing capacity of the composite after heat treatment [22]. The similar discussion made by Kennedy et al. [18]. Therefore, the mechanical strength and wear properties of the heat-treated composite improves.

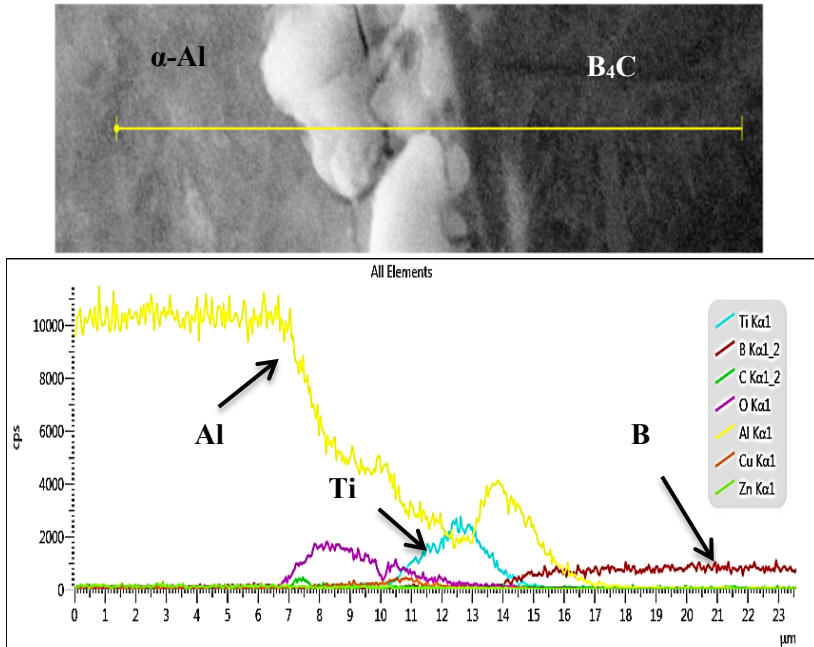


Figure 6: Reaction mechanism at particle matrix interface

Mechanical properties

Table 3 and Figure 7 shows the comparative study of mechanical properties of ACC and HTC. The result shows that there is a significant improvement of about 16.4% in the ultimate tensile strength in HTC over ACC. This improvement could be attributed to the precipitation hardening of the alloy matrix. Notably, the presences of titanium enhance the heterogeneous nucleation of α -Al grains, and thereby strengthen the grain boundaries by hindering the dislocation movements [14].

It is well known that the B_4C particles possess high inherent hardness. These particles, when dispersed into the soft α -Al matrix, enhance the hardness of the composite.

Table 3. Mechanical properties of the composite

AA7050/ B ₄ C Composite	Hardness (BHN)	Std. Dev.	Tensile Strength (N/mm ²)	Std. Dev.	Compressive Strength (N/mm ²)	Std. Dev.	Impact Energy (KJ/m ²)	Std. Dev.
ACC	132.1	12.53	230.66	15.04	374.21	12.47	24.17	1.69
HTC	157.7	8.04	275.33	13.50	439.52	14.35	27.16	1.42

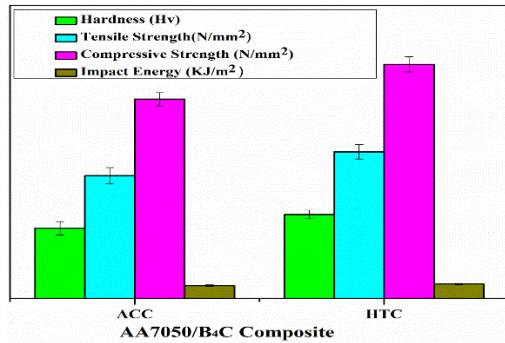


Figure 7: Mechanical properties of ACC and HTC

Furthermore, as discussed above the formation of interface layers contributes to the increase in the interface strength between α -Al matrix and B₄C. Also, the heat treatment further enhances the hardness of composite by 15.9% due to precipitation hardening mechanism. Collectively, the strengthening mentioned above mechanisms contributes to the improvement in the hardness of the composite through the Orowan mechanism [3,4]. Similarly, improvement in compressive strength and impact energy of the composite recorded as 14.8% and 10.9% respectively after heat treatment.

Wear properties of the composite

The pin on disc dry sliding wear tests were conducted on the ACC and HTC separately with the process parameters such as applied load and sliding speed. Each experiment was repeated for three times and the average of three has been taken for analysis. The test result reveals the improvement in the wear resistance in HTC than ACC. Wear is surface damage due to the combined effect of shear and compressive stress. Since due to the precipitation hardening effect, hardness and compressive strength of the composite increased after heat treatment. Therefore, the wear rate of HTC is lower than the ACC [3,20]. The load versus wear rate plots shown in the Figure 8 and Figure 9 indicate that the wear rate of ACC is higher than that of HTC for all loads and speeds investigated. Additionally, it is also anticipated that the strain hardening and

dynamic ageing phenomena prevail during the dry sliding which contributes to the increase in the wear resistance of the composite.

Further, observations on the effects of load and sliding speed of the composite on the coefficient of friction (COF) have been presented in Figure 8 and Figure 9. From the plots, it can be found that the COF increases with the increase in the load until 20 N and decreases significantly on the further increase of load. This could be attributed to the change the modes of wear from two-body abrasion to three-body abrasion as the wear debris interfere between the sliding surfaces [21]. Such a trend is seen in both ACC and HTC conditions for sliding speeds of 0.5 m/s and 1 m/s. Moreover, the COF of HTC is less than ACC. This may be attributed to the uniform dispersion and excellent interface of B_4C particles with the matrix. B_4C particles are expected to provide adequate dislocation pile-up which results in the strain hardening of the composites, which significantly contributes to improving the wear resistance of the composite [22].

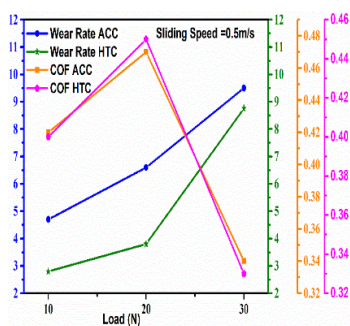


Figure 8: Wear rate and COF for ACC and HTC at sliding speed of 0.5 m/s

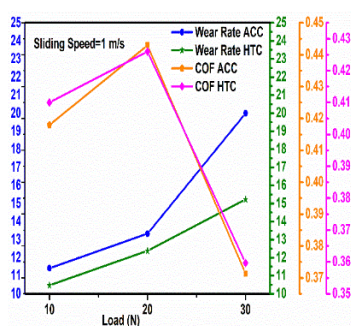


Figure 9: Wear rate and COF for ACC and HTC at sliding speed of 1 m/s

Conclusions

From the experimental evidence, the following conclusions have been drawn:

1. AA7050- B_4C composite developed successfully by flux assisted stir cast method, and the microstructure reveals the uniform distribution of B_4C particles into the matrix.
2. The EDAX analysis confirms the formation of a quaternary layer of $B_4C-TiB_2-Al_3Ti-Al$ across the B_4C particles. These layers enhance the interface strength between the matrix and reinforcement.

3. Heat treatment enhanced the tensile strength, hardness, compressive strength and impact strength by 16.4%, 15.9%, 14.8% and 10.9% respectively through precipitation hardening mechanism.
4. After heat treatment wear properties of the composite improved, wear rate and coefficient of friction of HTC is less than ACC for all set of loads and sliding speed.

References

- [1] J.C.Williams and E.A. Starke Jr., "Progress in structural materials for aerospace systems." *Acta Materialia* 51(19), 5775-5799 (2003).
- [2] G.Shaand A Cerezo. "Early-stage precipitation in Al–Zn–Mg–Cu alloy (7050)," *Acta Materialia* 52(15), 4503-4516 (2004).
- [3] Lashgari, H. R., Zangeneh, S., Shahmir, H., Saghafi, M., and Emamy, M., "Heat treatment effect on the microstructure, tensile properties and dry sliding wear behavior of A356–10% B₄C cast composites," *Materials and Design* 31(9), 4414-4422 (2010).
- [4] B.V. Ramnath, C. Elanchezhian, M. Jaivignesh, S. Rajesh, C. Parswajinan, A.S. Ghias, "Evaluation of mechanical properties of aluminiumalloy–alumina–boron carbide metal matrix composites," *Materials and Design* 58, 332-338 (2014).
- [5] V.P. Mahesh, P.S. Nair, T.P. Rajan, B.C. Pai, R.C. Hubli, "Processing of surface-treated boron carbide-reinforced aluminium matrix composites by liquid–metal stir-casting technique," *Journal of composite materials* 45(23), 2371-2378 (2011).
- [6] A. K.Suri, C.Subramanian, J. K.Sonber, and T. C. Murthy, "Synthesis and consolidation of boron carbide: a review," *International Materials Reviews* 55 (1), 4-40 (2010).
- [7] K.Kalaiselvan, N. Murugan, and S Parameswaran, "Production and characterization of AA6061–B₄C stir cast composite," *Materials & Design* 32(7), 4004-4009 (2011).
- [8] Q.Hu, Z.Haidong, and F. Li., "Effects of manufacturing processes on microstructure and properties of Al/A356–B₄C composites," *Materials and Manufacturing Processes* 31(10), 1292-1300 (2016).
- [9] F.Toptan, A.Kilicarslan, A.Karaaslan, M.Cigdem and I.Kerti, "Processing and microstructural characterisation of AA 1070 and AA 6063 matrix B₄C_p reinforced composites," *Materials and Design*, 31, 87-91 (2010).
- [10] A.Mazahery and M.O. Shabani, "Influence of the hard coated B₄C particulates on wear resistance of Al–Cu alloys," *Composites Part B: Engineering*, 43(3), 1302-1308 (2012).

- [11] Z.Zhang, K.Fortin, A.Charette and X.G.Chen, "Effect of titanium on microstructure and fluidity of Al-B₄C composites," *Journal of materials science* 46(9), 3176-3185 (2011).
- [12] Z.Zhang, X.G. Chen, and A.Charette, "Particle distribution and interfacial reactions of Al-7%Si-10%B₄C die casting composite," *Journal of materials science* 42(17), 7354-7362 (2007).
- [13] Y.Sahin and V. Kilicli, "Abrasive wear behaviour of SiC_p/Al alloy composite in comparison with ausferritic ductile iron," *Wear* 271(11-12), 2766-2774 (2011).
- [14] S. M. Kumar, V.Chakraborty, S.Subramanya and B. S. Murty, "Tensile and wear behaviour of in situ Al-7Si/TiB₂ particulate composites," *Wear* 265(1-2), 134-142 (2008).
- [15] B.S.Yigezu, M.M. Mahapatra and P.K.Jha, "On modeling the abrasive wear characteristics of in situ Al-12% Si/TiC composites," *Materials and Design* 50, 277-284 (2013).
- [16] R.Ranjith, P.K.Giridharan, J.Devaraj and V.Bharath, "Influence of titanium-coated (B₄Cp+ SiCp) particles on sulphide stress corrosion and wear behaviour of AA7050 hybrid composites (for MLG link)", *Journal of the Australian Ceramic Society* 53(2), 1017-1025 (2017).
- [17] D. Das, P Mishra, A Chaubey and S Singh, "Fabrication process optimization for improved mechanical properties of Al 7075/SiCp metal matrix composites", *Management Science Letters* 6(4), 297-308 (2016).
- [18] A. R.Kennedy and S. M. Wyatt, "The effect of processing on the mechanical properties and interfacial strength of aluminium/TiC MMCs," *Composites Science and Technology* 60(2), 307-314 (2000).
- [19] Liu, Z. W., Q. Han, and J. G. Li, "Formation of small blocky Al₃Ti particles via direct reaction between solid Ti powders and liquid Al," *Metallurgical and Materials Transactions A* 43(12), 4460-4463 (2012)
- [20] R.N.Rao, S.Das, D.P. Mondal, and G. Dixit, "Effect of heat treatment on the sliding wear behaviour of aluminium alloy (Al-Zn-Mg) hard particle composite," *Tribology international* 43(1-2), 330-339 (2010).
- [21] M.Uthayakumar, S.Aravindan, and K.Rajkumar, "Wear performance of Al-SiC-B₄C hybrid composites under dry sliding conditions," *Materials and Design* 47, 456-464 (2013).
- [22] J.M. Mistry, and P.P. Gohil, "Experimental investigations on wear and friction behaviour of Si₃N₄p reinforced heat-treated aluminium matrix composites produced using electromagnetic stir casting process," *Composites Part B: Engineering* 161, 190-204 (2019).

Design of the MCCIS on the Gas-Fueled Motorcycle to Overcome Detonation in Engine Idling

Didik Nurhadiyanto*, Mujiyono, Angger Gufita, Riyadi Prabowo Moecty,
Fatchurrohman Baihaqi, Sena Budi Pramana
Universitas Negeri Yogyakarta, Indonesia
*didiknur@uny.ac.id

ABSTRACT

Gasoline consumption is greater than fuel oil production in Indonesia. The situation has come to that of a fuel oil crisis. Prior research indicates that the exhaust gas emission of motorized vehicles using gasoline contains lead still as heavy metal. The problem with vehicles using fuel gas is that with the engine ignited and left idling detonation occurs because the gas supply is great while the air supply is small. In addition, the gas tank possible to explodes when sparks come from the combustion chamber. The objective of the research concerned here was to design the Mechanics Converter Considering Idle System (MCCIS) to overcome the problem of detonation at the time of engine idling, to design a flame arrester to prevent an exploding gas tank, and to testing the exhaust gas emission. The MCCIS may be used on low or high speed motorcycles using fuel gas. No detonation occurred in idle speed throughout. The flame arrester was able to avoid the sparks so the fire wasn't moving into the gas tank. Results of the exhaust gas emission tests indicate that exhaust gas emissions at idling, moderate and high speeds are included in the CO and HC content of the specified magnitude.

Keywords: *converter, gas, detonation, idling, flame arrester*

Introduction

The production of gasoline in Indonesia was decrease year by year, while the consumption of gasoline was increase. Figure 1 shows the production and consumption of gasoline [1]. The situation has come to that of a fuel oil crisis start in 2003 [2]. The difference in the use and production of gasoline increases from year to year. It is caused by the increasing number of motorized vehicle owners, which causes gasoline demand to increase as well. On the other hand,

the use of fuel gas for transportation is still quite little compared to its production so that there is still sufficient room for fuel gas marketing, particularly for transportation [3]. Figure 2 shows a production and consumption of natural gas in Indonesia. A great deal of the natural gas produced is exported abroad.

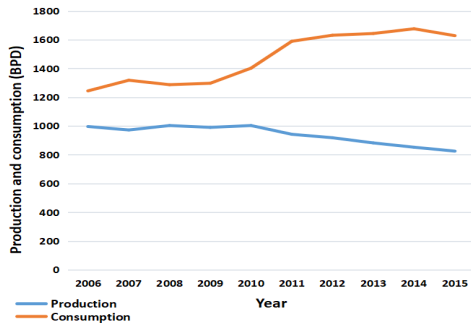


Figure 1: Production and consumption gasoline [1]



Figure 2: Production and consumption of natural gas in Indonesia [3]

It is hoped that in the future many motorcycles use fuel gas. Indonesia is rich with natural resources. Fuel gas in Indonesia is quite great in potential because of the quantity of gas resources. Therefore, the demand for alternative fuels to decrease dependence on conventional fuel becomes very important. Vehicles using fuel gas need to be developed; among them are those using fuel gas. In cost as fuel, gas is cheaper compared to gasoline.

The exhaust gas emission of motorized vehicles using fuel oil contains lead and it causes air pollution. The air pollution due to lead still as heavy metal (Pb) happens because of imperfect combustion in the combustion chamber [4]. The metal Pb in natural state could not degrade or be destroyed.

This metal is also called a non-essential trace element whose content is the highest so that it is very dangerous if accumulated in the human body [5, 6]. Suthisripok et al. mentioned that at an average speed of 60 km/h, the average LPG consumption rate from the city road test was 40 km/L, around 17.7 % higher. This corresponded to a decrease in the energy density of LPG of about 16.2%. The concentration of CO and HC were 44.4 % lower and 26.5% lower in emissions [7].

As for fuel gas as motorcycle fuel, researchers have made research on its use. The use of fuel gas in a motorcycle originally using gasoline could be done with a conversion kit. Erkus et al. seek the influence of the front, middle, and rear positions of fuel spraying into the intake manifold. In the case of gasoline use, the lowering of fuel consumption index achieved in relation with the rear fuel spraying position is optimum compared to those achieved in relation with the front and middle fuel spraying positions at 6000 rpm [8]. There has been researched by Romadoni et al. on gas-fuelled motorcycle performance. The performance of a motorcycle using fuel gas shows improvement in torque and power and lowering in CO, CO₂, and HC emission contents [9]. Another testing method is applied by adjusting the ignition timing or ignition angle to lower the CO and HC emission contents [10, 11]. Results of the testing show that by setting the ignition angles at 11°, 14°, and 17° prior to TMA (thermomechanical analysis) lowering of CO emission amounting to 0.24% - 97.68% and HC emission amounting to 97.5% in volume is known to take place [12].

The type of fuel gas often used is natural gas. Fuel gas compounds are propane (C₃H₈), propylene (C₃H₆), iso-butane (C₄H₁₀), and butylene (C₄H₈). Fuel gases are mixtures of such hydrocarbons which are gaseous under atmospheric pressure but for storage and transportation purposes they could be condensed into liquids at normal temperature under sufficiently great pressure. Liquefied fuel gas, when evaporating, could form into gas around 250 times greater in volume [13].

Fuel gas has the advantage of, among others, having a high octane rating ranging from 120 to 130. It is higher than that for gasoline, which is 80 for the premium type and 90 for the premix type. The result of gas combustion is cleaner because the carbon chain of fuel gas is quite short compared to that of gasoline [14, 15].

A constraint in the use of fuel gas in motorcycles is the overly high engine speed in idling condition. It is caused by overly great amount of fuel gas coming into the intake manifold and the low specific weight of fuel gas (0.562 kg/m³), which is even lower than that of gasoline. It causes detonation when the engine is in ignited and idling condition. In addition, it is easy for the gas tank to explode when sparks come from the combustion chamber. The gas tank explosion highly endangers the motorcycle rider. Therefore, the researcher has made a converter engineering to overcome the problem in

engine ignition and idling and designed a device to prevent gas tank explosion when sparks occur.

The problem occurring in the converter is especially at the time when the engine is on and kept idling. When the engine is idling, detonation occurs because of excessive gas supply while the air supply is still lacking. Gas has the character of being very light and inflammable so that even with a small hole for the gas to go through, its flow would remain great. This does not matter when the engine is run at high speed because then the need for gas is also great. To overcome the problem of a gas tank that is prone to easily explode, it is necessary to design a tank that does not leak easily and is not easily prone to explode. In addition, the creeping of sparks from the combustion chamber needs to be prevented by applying a flame arrester. The flame arrester is useful as safeguard when sparks occur in the area around the engine by means of halting the fire in order that it does not creep to the gas tank.

The research operation concerned here centered on the design of the converter designed, which was called MCCIS from here, to overcome detonation at the time when the engine is on and idling and the design of the flame arrester. The research activity went through the stages of designing the MCCIS, manufacturing it, assembling it, testing it, and obtaining research data.

Research Plan

A design of scheme diagram of the fuel gas flow is seen in Figure 3. First, gas is caused to flow out of the gas tank by using a pressure regulator in 0.05 MPa. After that the gas is allowed to flow to the safety valve or diaphragm valve. The valve functions to direct the gas to idling or high speed engine running. After the safety valve, the gas directed to the idling regulator for flow advance to idling speed engine running and then the process of combustion. When the combustion chamber occurs, the suction process will vacuum at the intake manifold. This process causes the opening of the diaphragm valve and gas to flow toward the idle regulator or faucet to the converter. The idling regulator needed to regulate the consumption of fuel charts idling. Idling speed engine running occurs at the engine speed range of 1000-1200 rpm. When the engine is operating at idle conditions the gas supply is regulate by a pressure regulator and the air supply is very small. Pressure is regulated so that gas and air requirements are very small and in accordance with needs. Gas regulation uses a small gap so that the gas needs when idle are met.

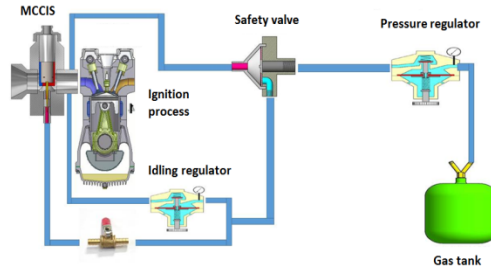


Figure 3: A scheme of the fuel gas flow

Any speed above that range is already upper speed. When the engine at high speed running, the gas is directed toward the regulator for flow advance to upper speed engine running and then the process of combustion. The function of the faucet is to reduce the gas pressure going to the converter. The gas that comes out the cylinder must stay high then it is lowered using a faucet. The principle of decline uses the Bernoulli principle, namely by shrinking the cross section of the flow. Using a smaller cross section the flow will increase but the gas pressure will decrease.

MCCIS functions to regulate the supply of gas and air to combustion chamber so perfect combustion is obtained. This mixing is divided into two types of combustion, namely combustion idle conditions and high speed combustion. Perfect combustion will produce maximum output power. MCCIS parts include body converter, cover converter, jet needle, needle, piston valve, main jet, idle screw, pilot jet, pressure idle control and intake manifold. Comparison between fuel and air is usually called AFR. The AFR to get perfect combustion is 1:11.5.

Figure 4 shows a cross-section image of the MCCIS. The complete version of the MCCIS system could be seen in Figure 5. The materials the MCCIS is made of are aluminum and brass. The reason for these choices is that these materials possess the character of being resistant to heat, releasing heat easily, being resistant to fuel gas pressure, and being resistant to corrosion.

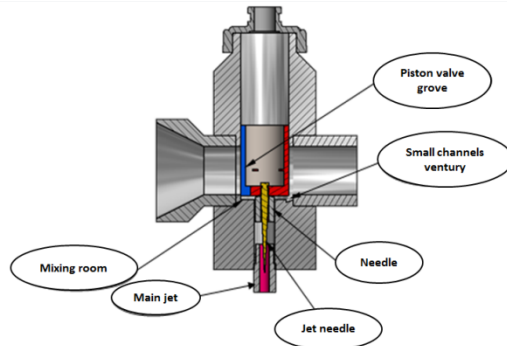


Figure 4: Converter

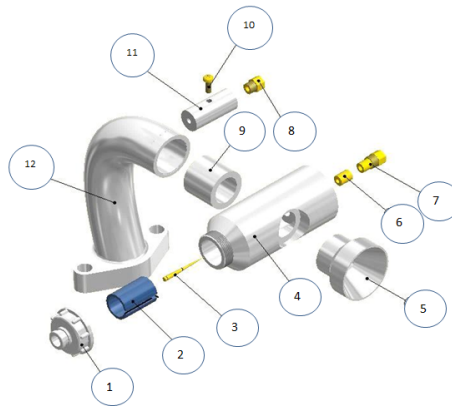


Figure 5: MCCIS System

Remark:

No	Name of part	Material
1	Cover converter	Aluminum
2	Piston valve	Brass
3	Jet needle	Brass
4	Body converter	Aluminum
5	Venturi converter	Aluminum
6	Needle jet	Brass
7	Main jet	Brass
8	Idle jet	Brass
9	Converter joint	Aluminum
10	JIS B 11 – A M3 x 8	Brass
11	Idle part system	Aluminum
12	Intake manifold	Aluminum

Figure 6 shows the gas discharge control. The gas discharge control at higher engine speed is regulated by using, among other components, the piston valve, the jet needle, and the needle.

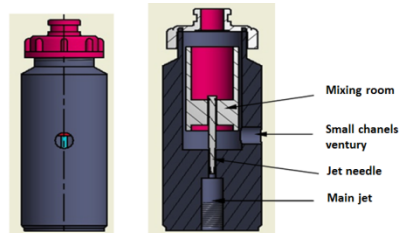


Figure 6 : The gas discharge control

Figure 7 shows the safety valve. This valve functions to release and stop the gas flow. Such regulation works automatically. When the intake manifold contains only a vacuum because of the suction process happening in the combustion chamber, the membrane opens and gas flow occurs and after that the membrane would close again and so on.

Safety kits are components of the MCCIS system guarding the vehicle user's security against and safety from the dangers of a flame or a fire when gas leak occurs and gets ignited because of sparks from a short circuit in the electricity or the surrounding environment. This system consists of the safety valve, diaphragm, and flame arrester. The flame arrester functions to halt fire creeping when a fire occurs so that it reduces the risk of facing greater danger. Figure 8 shows a flame arrester. This device would let fuel gas flow into water and proceed until it comes out of the water and then it would flow to the converter kits. The water functions to halt and extinguish the fire in order that it does not creep to the gas tank. In the flame arrester, there is a valve in order that the water does not get inside the converter kits.

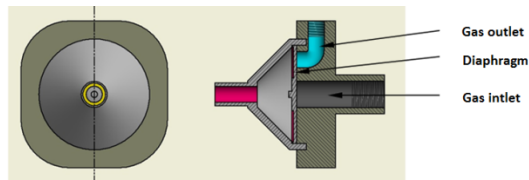


Figure 7: Safety valve

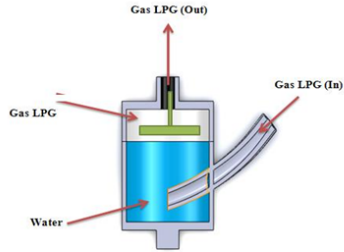


Figure 8: Flame arrester

Method of Experiment

The research used a Honda Supra Fit 100 cc motorcycle produced in 2006. Prior to the research, the motorcycle used conventional petrol fuel as its fuel. In the research, the petrol was replaced with natural gas. Petrol is clearly different in character from natural gas. In order to make it ignite easily, conventional fuel should be sprayed so that it becomes a mist. The mixing and misting process uses a carburetor. Because conventional fuel is liquid in form, it should be made to flow in accordance with the laws of liquid fluids. As for fuel gas, for the combustion, it needs only to be directly ignited with no need to be made misty first. This fluid is quite light; it would fill up empty space. A motorcycle using fuel gas needs a converter that would regulate the fuel gas needed. The gas tank used was a gas container 3 kg in weight produced by the Indonesian state-owned oil and natural gas mining company, Pertamina. It was done in order to make the gas provision easy and such a gas container already proved to be safe.

The research was to design the MCCIS as converter to regulate the fuel gas needed. The MCCIS regulates the gas flow for running the engine at idling speed and at higher speed. To know whether the device functions well or not, the engine needs to be tested. The testing is on the engine running at idling speed and at higher speed. In addition, exhaust gas emission testing and torque testing also need to be done. The fuel mixing system operates by using converter kits with several components, namely, a piston valve, a jet needle, a needle, a mixing chamber, a pilot jet, and a pressure idling control as regulator of the idling condition. The regulator of the amount of air entering the combustion chamber used the piston valve with a groove with a cross-section area of 0.3 cm^2 as place for air entrance when the engine was at idling speed. The testing on the engine running at idling speed was done at Faculty of Engineering at Universitas Negeri Yogyakarta, by turning on the engine and running it at the speed of around 1200 rpm for twenty minutes with the vehicle in an immobile condition. At this stage, attention was paid to the engine to check whether there was any detonation or not. In addition, the engine was also checked to see whether it remained running or stalled. The detonation was

checked using the sound of the motor engine. If detonation occurs, small explosions will occur in the exhaust.

Running the engine at higher speed was done at moderate and high speeds. The engine was started and run at the speed of around 4000 rpm for twenty minutes. Then it was run at the speed of around 8000 rpm for five minutes. At both speeds, the vehicle was not ridden anywhere (the gears were kept in neutral position). A check was made to decide whether detonation occurred or not. The detonation also checked using the sound of the motor engine. If detonation occurs, small explosions will occur in the exhaust. In addition, the engine also checked to decide whether it stalled or remained running.

Testing Machine and Research Support Equipment

The motorcycle performance testing was done in an open place and the road. The testing in the open place was done on the motorcycle with the engine running at idling speed and at higher speed without the vehicle leaving its place. The testing with the engine idling was at the speed of around 1200 rpm. The testing with the engine running at higher speed was at the moderate speed of around 4000 rpm and at the high speed of around 8000 rpm. As for the testing on the road, it was to test the maximum speed and maximum fuel gas consumption. The equipment used in the testing consisted of a motorcycle using fuel gas, a safety helmet, a camera, a digital scale, and a video maker.

Besides the tests above, the exhaust gas emission and the torque produced would also be tested. The torque produced was tested by using a dynamometer while the exhaust gas emission was tested by using an exhaust gas analyzer. The exhaust gas emission testing was done on the vehicle with the engine on at low, moderate, and high speed. The exhaust gas emission threshold levels according to the Indonesian Ministry of Life Environment [16] could be seen in Table 1 while that according to Euro standards [17] could be seen in Table 2.

Table 1: The maximum constrain of exhaust gas emission based on Living Environment Ministry

Category	Made year	Parameters	
		CO%	HC (ppm)
Motorcycle 2 stroke	< 2010	4,5	12.000
Motorcycle 4 stroke	< 2010	5,5	2.400
Motorcycle 2 and 4 stroke	≥ 2010	4,5	2.000

Remark: ppm (part per million)

Table 2: The maximum constrain of exhaus gas emission based on Euro Standard

Reference	CO	HC	NOx	PM
Euro0	12,3	15,8	2,6	-
Euro1	4,9	9,0	1,23	0,4
Euro2	4,0	7,0	1,1	0,15
Euro3	2,1	5,0	0,65	0,1
Euro4	1,5	3,5	0,46	0,02
Euro5	1,5	2,0	0,46	0,02

Result and Discussion

Idling Engine Testing

The motorcycle using fuel gas with the MCCIS successfully passed the testing with the engine idling. During idling speed there was no detonation occurred and the combustion went smoothly. The mixing of the fuel with the air was done well; however, no comparison related to the use the two different fuels was measured. The exhaust gas emission at idling speed remained below threshold levels. The torque produced was not different, either, from that produced when fuel oil was used.

When the engine was running at idling speed, the gas supply was regulated by a pressure regulator at 0.05 MPa. The air coming in was also controlled in order that there was very little flow. The ratio between air and gas was 1:12. The pressure was adjusted so that a suitable ratio was attained for igniting and running the engine in an idling condition. The engine speed around 1200 rpm. In that condition, the MCCIS let very little supply of fuel gas flow because the gap gone through was quite narrow with the cross-section of the hole quite small in area. That was purposely done because the fuel gas and the air needed for engine idling were very little. When the fuel gas flow is great, then detonation would occur. The setting of the fuel gas and air flow was done by trial and error until the most perfect engine running at idling speed was obtained.

The function of the faucet located before the MCCIS system was to maintain the same pressure when supplying fuel gas to the MCCIS. When the pressure exerted was greater compared to the engine need, it was then reduced with the faucet so that the pressure exerted fitted the engine need. It could maintain the same fuel gas pressure in the MCCIS every time in spite of changing engine conditions. It applied the Bernoulli principle as theoretical basis in designing the MCCIS.

Testing of Engine Running at Higher Speed

As previously implied, the system of fuel mixing by using the MCCIS went through several components, namely, the piston valve, jet needle, needle, mixing chamber, and pilot jet. The regulator of the air amount entering the combustion chamber used the piston valve having a groove as the place for the air entrance. The needle and jet needle tapering in form regulated the amount of LPG flow while the magnitude of the air flow entering the combustion chamber was regulated by the piston valve. When acceleration was done, the cross-section area would increasingly enlarge until it became 1.53 cm² to supply more air.

The testing results showed that the motorcycle successfully passed the testing on the engine running at higher speed. No detonation occurred while the engine was on. No problem occurred, either, in starting and running the engine. The mixing of the fuel with the air was also well done; however, no comparison related to the use of the two different fuels was measured, either. The exhaust gas emission at higher speed remained below threshold levels. The torque produced was not different, either, from the one produced by the motorcycle using fuel oil.

Fuel Gas Consumption Testing

The testing on fuel gas consumption was done on the road to attain the condition of actually using the motorcycle on the road. Data collection was done each time a distance of 10 km was covered at the same speed. The data related to the same speed were collected two to three times according to need. The speed used was from three ranges, namely, the 0-40 km, 40-60 km, and 60-90 km speed ranges. It was for the purpose of knowing the fuel gas needed at each speed. The final result was the average of the data obtained at each speed. The data about fuel gas consumption at each speed range could be seen in Table 3.

Table 3: Gas consumption

Experiment	Speed range	Gas consumption
1	0-40	73.03
2	40-60	97.77
3	60-90	45.51
Average		72.1

The general average fuel gas consumption obtained from the three data items above was 72.1 km/kg. Meanwhile, the general average fuel oil consumption was around 50 km/kg. Compared to the use of fuel oil, the use of fuel gas showed an efficiency of 44%.

Exhaust Gas Emission Testing

The data resulting from the emission testing could be seen in Table 4 and trend content of CO, CO₂, HC and O₂ shows in Figure 9 and Figure 10. With the results displayed on the printout from the testing device and the table of threshold levels, it could be concluded that the idling speed of around 1200 rpm produced a CO content of 0.354%. It was already included among the predetermined magnitudes. The HC content of 356 ppm with the lambda (λ) value of 1.385 was also already included among the predetermined magnitudes. The speed of around 8000 rpm produced a CO content of 0.119%, which was already included among the predetermined magnitudes. The HC content of 274 ppm with the lambda (λ) value of 1.342 was also already included among the predetermined magnitudes. The speed of around 10.000 rpm produced a CO content of 0.162%, which was already included among the predetermined magnitudes. The HC content of 630 ppm with the lambda (λ) value of 1.305 was also already included among the predetermined magnitudes.

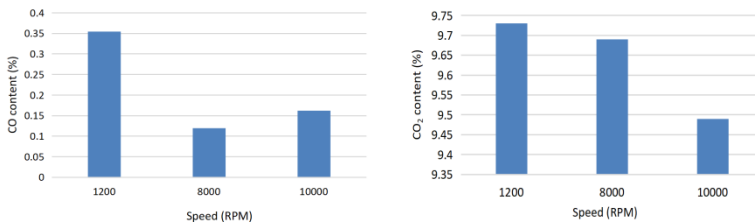


Figure 9: CO and CO₂ content

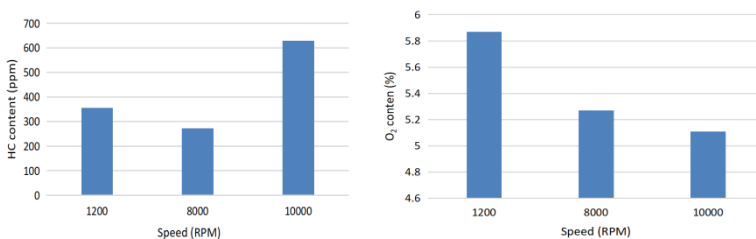


Figure 10: HC and O₂ content

Table 4: Exhaust gas analysis

Gas	Speed	Speed	Speed
Outside temperature (°C)	35	34	34
Pressure (kPa)	988	988	989
Real Humidity (ZHR)	50	50	51
Relative air/fuel ratio (λ)	1,305	1.342	1.385
CO (%)	0.162	0.119	0.354
CO ₂ (%)	9.49	9.69	9.73
HC (ppm)	630	274	356
O ₂ (%)	5.11	5.27	5.87

Torque Testing

The data about the torque of the motorcycle using natural gas could be seen in Figure 11. The same motorcycle was used to make the comparison. The dynamometer was used to measure the torque related to the motorcycle. The testing was done several times with various speed. The testing was done at the speed which would produce the maximum attainable torque and power; that speed should be greater than 5000 rpm. The testing result showed that the maximum attainable power was 5.6 hp at the speed of 7801 rpm and the maximum attainable torque was 6.02 Nm at the speed of 6153 rpm. For comparison, the maximum attainable torque of the motorcycle using petrol at the same speed was 6.21 Nm. The result of the comparison showed that the torque produced was relatively similar.

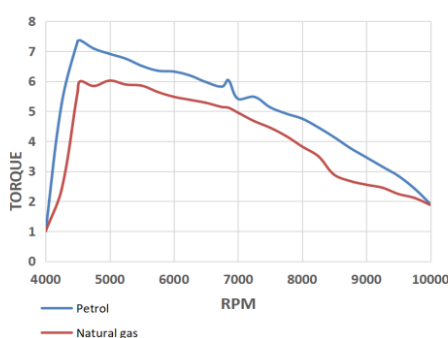


Figure 11: Torque test result for motorcycle using conventional and gas fuel

The natural gas produces 17% lower torque than petrol as shown in the Figure 10. According Suthisripok et al. [7], the performance of the converted natural gas will generally drop 15-20% from the petrol. In general, modified

vehicles suffer from power loss and experience drive problems as a result of retro fit conversion packages design and/or installation.

Conclusion

The conclusion of the research is as follows. The MCCIS could be used on motorcycles using fuel gas with the engine for both idling and higher speed. During idling speed there was no detonation occurred and the combustion went smoothly. The flame arrester could stop the sparks so that the fire did not creep to the fuel gas tank. The results of emission testing indicate that the engine running at idling, moderate, and high speeds produce CO and HC contents that are already included among the predetermined magnitudes. The motorcycle using fuel gas and gasoline produce relatively similar torque.

Acknowledgement

The authors would like to be obliged to Universitas Negeri Yogyakarta for providing laboratory facilities and financial assistance.

References

- [1] Minyak Bumi (Petroleum), Indonesia Investment Report. Retrieved from <https://www.indonesia-investments.com/id/bisnis/komoditas/minyak-bumi/item267/> [accessed: 23/02/2020].
- [2] Subsidi BBM Apakah Produksi Minyak di Indonesia Cukup, 2014. Retrieved from <http://obengplus.com/articles/4405/1/Subsidi-BBM-apaakah-produksi-minyak-di-Indonesia-cukup.html>. [Accessed 23/02/2020].
- [3] Natural Gas Indonesia, 2016. Retrieved from <https://www.indonesia-investments.com/business/commodities/natural-gas/item184> [Accessed 23/02/2020].
- [4] Dubey, B., Somvanshi, S., and Dhupper, R., "Air Pollutants and Their Environmental Impact: A Review," *International Journal of Advanced Research in Engineering and Applied Sciences* 2(5), 33-42 (2013).
- [5] Sawyer, R.F., "Vehicle Emmissions:Progress and Challenges," *Journal of Exposure Science and Environmental Epidemiology* 20, 86-488 (2010).
- [6] Duruibe, J.O., Ogwuegbu, M.O.C., and Egwurugwu, J.N., "Heavy Metal Pollution and Human Biotoxic Effects," *International Journal of Physical Science* 2, 112-118 (2007).

- [7] Suthisripok, T., Phusakol, N., and Sawetkitput, N., "Bi-fuel System-Gasoline/LPG in A Used 4-Stroke Motorcycle-Fuel Injection Type," 5th Asia Conference on Mechanical and Material Engineering (ACMME) (2017).
- [8] Erkus, B, Surmen, A, Karamangil, MI., Arslan, R., Kaplan, C., "The Effect of Ignition Timing on Performance of LPG Injected SI Engine," Energy Education Science and Technology Part A: Energy and Research 28(2), 889-896 (2012).
- [9] Ashok, B., Ashok, SD., and Kumar, CR., "LPG Diesel Dual Fuel Engine – A Critical Review," Alexandria Engineering Journal 54, 105-126 (2015).
- [10] Bisen, H.B., Suple, Y.R., "Experimental Investigations of Exhaust Emissions of Four Stroke SI Engine by Using Injection of LPG and Its Analysis," Int. J. of Modern Engineering Research (IJMER) 3(5), 2060-2015 (2013).
- [11] Wu, Y.Y., Chen, B.C., Tran, A.T., "Pollutant Emission and Engine Performance Improvement by Using Semi-direct Injection Spark Ignition Engine Fuelled LPG," Aerosol and Air Quality Research 12, 1289-1297 (2012).
- [12] Lawankar, SM., Dhamande, LP., Khandare, SS., "Experimental Study of Effect of Ignition Timing and Compression Ratio on Nox Emission of LPG Fuelled Engine," Int. J. of Scientific and Engineering Research 3(10), (2012).
- [13] Peterson, E.R. Method of Storing and Transporting Light Gases, Justia Patent, US Patent, No. 201100415118.2017.
- [14] Jha, M., Tyagy, A.S.R.K, and Verma, M.K., "Comparative Study of Exhaust Emission of Commonly Used Fuel in an Internal Combustion Engine," Journal of Environmental Science, Computer Science and Engineering and Technology 2(1), 52-56 (2013).
- [15] Saraf, R.R., Thipse, S.S., and Saxena, P.K., "Comparative Emission Analysis of Gasoline/LPG Automotive Bifuel Engine," International Journal of Environment Science and Engineering 1(4), 198-201 (2009).
- [16] SK Menteri Negera Lingkungan Hidup Nomor 35 Tahun 1993 tentang Ambang Batas Emisi Gas Buang Kendaraan Bermotor. Retrieved from <http://www.kelair.bppt.go.id/Hukum/data/kepmen/bml/35-1993.pdf> [Accessed 23/02/2020].
- [17] Limits to improve air quality and Health. Updated December 11, 2017. Retrieved from <https://www.theaa.com/driving-advice/fuels-environment/euro-emissions-standards> [Accessed 23/02/2020].

Effect of Carbon Nanotube-Silane Addition on Mechanical Properties of Chloroprene Rubber-filled Carbon Black

Kok-Tee Lau^{1,*}, Jeefferie Abd Razak², Hairul Effendy Ab Maulod¹, Noraiham Muhamad², Mohamad Hanif Hashim¹, Nurzallia Mohd Saad³

¹Fakulti Teknologi Kejuruteraan Mekanikal dan Pembuatan,

²Fakulti Kejuruteraan Pembuatan,

Universiti Teknikal Malaysia Melaka, 76100 Durian Tunggal, Melaka, Malaysia

*ktlau@utem.edu.my

³Sunrich Integrated Sdn. Bhd., Senawang, Malaysia

ABSTRACT

Chloroprene-filled CNT rubber has been investigated for the electromagnetic shielding application. Nevertheless, there are continuous studies to overcome CNTs agglomeration, materials loss and air contamination issues generated during conventional melt compounding process. Thus, the current study proposes the usage of polar and low molecular weight ethanol solvent as dispersant for CNT fillers and silane-based Si-69 as coupling agent. Si-69 is a widely used fillers' coupling agent because of its reliable performance in the industrial-scaled rubber compounding process. This study is to investigate the effect of carbon nanotube (CNT)-Silane addition as secondary fillers on tensile strength, elastic modulus and cure characteristics of chloroprene rubber (CR)-filled carbon black (CB) compound. The CR-filled CB was prepared by internal mixing, followed by roll-mill process in which CNT-Silane dispersion was added. For comparison, the samples of CR-filled CB without CNTs addition and with as-received CNTs addition were prepared and characterized. The CR composite added with CNT-Silane dispersion displayed tensile strength and elastic modulus (at 300% elongation) of 23 MPa and 18 MPa respectively, which are 4% higher than the CR composite added with as-received CNTs. The findings were supported by the FESEM micrograph of tensile fracture samples that showed the CNT-Silane addition produced better CNTs dispersion in the CR-filled CB compound. Furthermore, the usage of

CNT-Silane improved the CR-filled CB compound processibility by reducing the minimum (ML) and maximum torque (MH) values from 0.34 and 1.11 N.m in as-received CNT samples to 0.32 and 1.04 N.m respectively in CNT-silane samples.

Keywords: *Flexible electronics, electromagnetic interference (EMI), synthetic rubber, carbon nanotube, silane coupling agent*

Introduction

Recent flexible and stretchable electronics applications create high demands for flexible and durable materials [1]. Chloroprene-filled CNT rubber has been investigated for the electromagnetic shielding application [2]. Nevertheless, there are continuous studies to overcome CNTs agglomeration generated by conventional melt compounding technique. Furthermore, CNT powder becomes airborne quite easily during pouring and compounding process in the industrial-scaled internal mixer. This airborne problem contributes to raw materials loss and air contamination issues.

Several studies had reported the latex mixing method, where CNTs is mixed with rubber in latex form [3,4]. Although promising results were reported, the scientific method is not feasible and incurs high manufacturing cost. Solvent dispersion technique is a promising approach to resolve the CNTs mixing problem [4]. However, the studies used hazardous tetrahydrofuran and toluene which require laborious drying process to remove the nonpolar high molecular weight organic solvents from CNTs. It is also reported that uncommon dispersing or coupling agent such as 1-decyl 3-methyl imidazolium chloride was used for CNTs [5], which again requires a cleaning process to remove the corrosive halide species.

Thus, the current study proposes the usage of polar and low molecular weight ethanol solvent as a dispersant for CNT fillers and silane-based Si-69 as a coupling agent. Si-69 is a widely used fillers' coupling agent because of its reliable performance in the industrial-scaled rubber compounding process [6]. The current paper will report the effect of CNT-Silane filler dispersion addition on the tensile strength and elastic modulus of the CR-filled CB+CNT compound. Microstructural tensile fracture sample and cure characteristics of the compound according to ASTM D6204 standard is also presented to support the mechanical findings.

Methodology

CR master batch with the formulation as stated in Table 1 was prepared using an internal mixer (Yi Tzung) operating at 60 °C, rotor speed of 900 rpm and mixing time of 8 mins. Subsequently, the CR match batch was divided into three smaller portions and then was calendered separately with different formulations (refer Table 2) using two-roll mill (model: MT2-2, Yi Tzung) at a rotor speed of 19.3 rpm (front) and 22.5 rpm (back) and mixing time of 5 min. All chemicals used in the formulations are from industrial grade.

Table 1: Formulations of master batch

Chemicals	Loading(phr)
Chloroprene (CR)	100
Zinc oxide (ZnO)	5
Stearic Acid (ST Acid)	0.5
Nocrac AD-F	2
Coumarone Resin (G90)	8
Carbon Black (N550)	40

Table 2 shows 1 phr CNTs was added as second fillers for CNT and CNT-Silane samples. During roll-mill, as-received CNTs was added in dry form for CNT samples, whereas, CNTs was added in dispersion form for CNT-Silane samples. CNT-Silane dispersion was prepared with the ultrasonication of 1.25 g Si-69 silane coupling agent in the 100 mL ethanol solution (95%). Then, as-received CNTs was mixed into the Si-69 solution. Additional 100 mL ethanol solution was then added, followed by further agitation by ultrasonication for 60 min. As a control, CR compound samples without CNTs (which is an established formulation) were also prepared.

Table 2: Second formulations added during roll mill

Chemicals	Loading (phr) for		
	CNT	CNT-Silane [#]	Control
Carbon Nanotubes (CNTs)	1	1 [#]	0
Magnesium Oxide (MGO)	4	4	0
Ethylene Thiourea (ETU-80)	0.7	0.7	0.7
N-Cyclohexyl-2-Benzothiazole Sulphenamide (CBS)	0.75	0.75	0.75

[#]amount of added CNT (in dispersion form) was controlled at 1 phr dry weight of CNTs. Silane and ethanol solutions were not included in phr calculation.

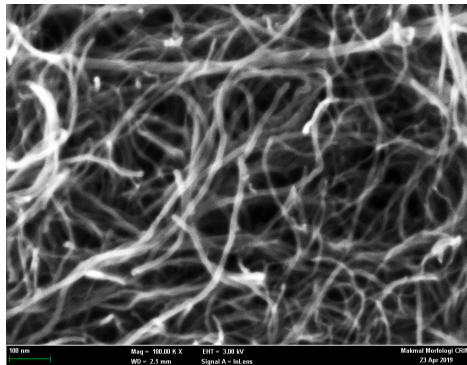
Sheet samples (sample size = 4) for the tensile test were prepared by hot press process of each calendared CR rubber compound in the respective sheet-shaped cavity steel molds, at 160 °C and pressure of 110 kg-force for 10 min. Tensile tests were performed on the samples according to JIS K 6251 standard using Tensometer (model: UR-2060, U-CAN DYNATEX) to obtain the average and standard error of tensile strength and elastic modulus. Surface of tensile fracture samples were observed using Field-emission Scanning Electron Microscope (FESEM, 3 kV accelerating voltage, secondary electron emission mode, Merlin compact-60-25, Carl Zeiss).

Lastly, cure characteristics of the fresh calendared CR compounds were characterized using rheometer (UR-2010, U-CAN DYNATEX) according to ASTM D6204 standard.

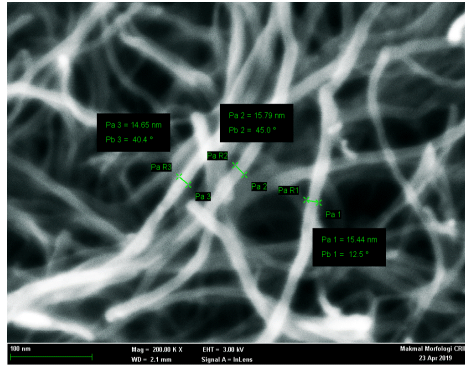
Result and Discussion

Microstructure of CNT

Figure 1 shows the as-received CNTs used as fillers for CNT and CNT-Silane samples had a diameter range between 14 to 16 nm. Physical entanglement between CNTs were clearly shown, which explains the presence of CNTs agglomeration before the CNTs were added during the CR compounding.



(a)



(b)

Figure 1: FESEM micrograph of as-received CNT fillers at magnification of: (a) 100,000 \times , and (b) 200,000 \times

Tensile Test

Tensile strength (TS) with standard error bar plots in Figure 2 show that Si-69 treatment on CNT filler able to negate the deteriorating effect of CNT addition as fillers in the CR-filled carbon black (CB) compound. TS of samples filled with CNT-Silane is comparable to the control samples (with no CNT content) and was 3% higher than the CNT samples (with as-received CNTs). The low TS of the CNT samples were caused by the formation of CNTs agglomerations in the CR-filled CB compound, resulted in an earlier failure. This agglomeration problem was resolved with the usage of CNTs treated with Si-69, in which the latter assisted CNT fillers dispersion through calendaring process with CR-filled CB. It is believed a better dispersion of CNT-Silane provide more uniform tensile stress distribution throughout the CR tensile samples, reducing stress concentration at particular weak regions. Furthermore, the Si-69 addition strengthened the interaction between CNT-Silane fillers and CR matrix. Nevertheless, CNT-Silane fillers did not perform well as reinforcement agent for CR compound, thus the TS did not improve significantly in comparison with control samples. It appears that the presence of silane provided lubrication effect to the CR compound which permitted polymer chain slippage toward tensile fracture.

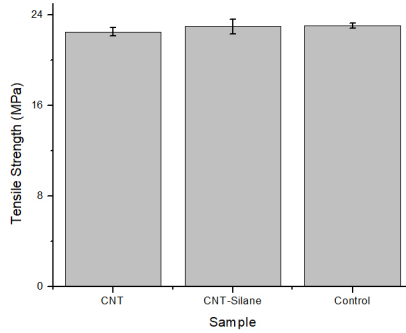


Figure 2: Tensile strength of CR compound samples

It appears that the addition of CNT-Silane fillers improved the stiffness characteristic by enhancing the tensile modulus at 300% of elongation (refer Figure 3). The Si-69 addition strengthened the interaction between CNT-Silane fillers and CR matrix, thus increased the resistance toward the tensile elongation [7]. This can be the reason for the enhanced stiffness value.

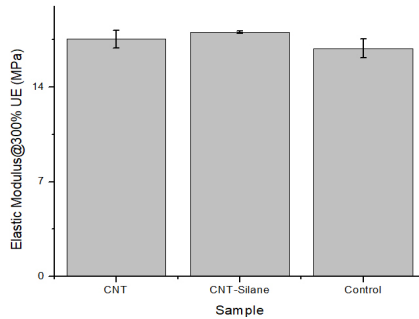


Figure 3: Elastic modulus (at 300% elongation) of CR compound samples

Microstructural Surface of Tensile Fracture

FESEM micrograph in Figure 4 shows the ductile fracture surface due to the observed apparent shear yielding mechanism. The fracture surface appeared rough and many cavities were observed in the rubber matrix with uniform distribution [8]. CNT-Silane exhibited smoother fracture surface, thus verify the argument that silane acted as lubrication which triggered shear slippage fracture.

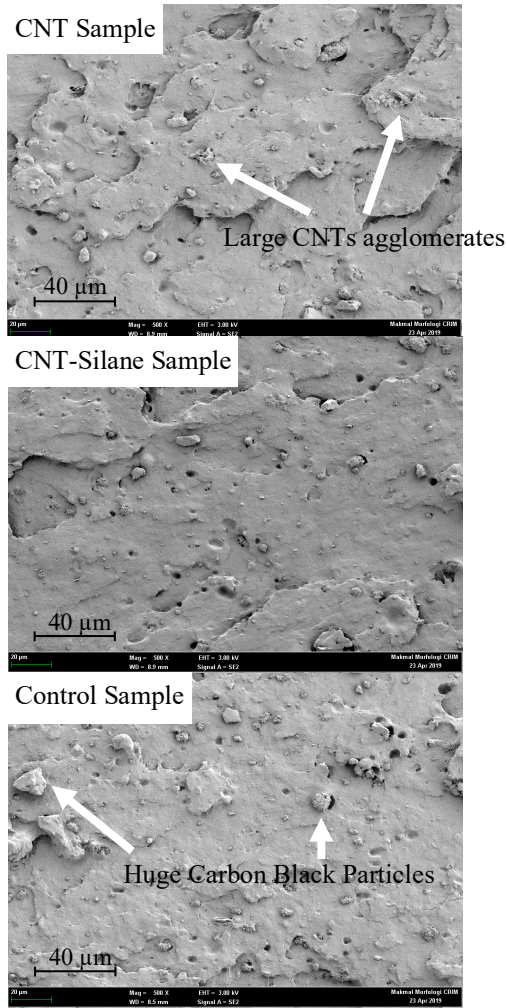


Figure 4: Low magnification FESEM micrographs of the surface of tensile fracture samples

FESEM micrograph in Figure 5 shows large CNT fillers agglomerates were found in the CNT tensile sample. CNT fillers agglomerates appeared in smaller size and dispersed widely in the CNT-Silane sample. The microstructural difference in the CNT fillers agglomerates size and distribution indicates an improved CNT fillers dispersion in the CR-filled CB compound. This microstructural finding verified the current tensile strength and elastic modulus findings.

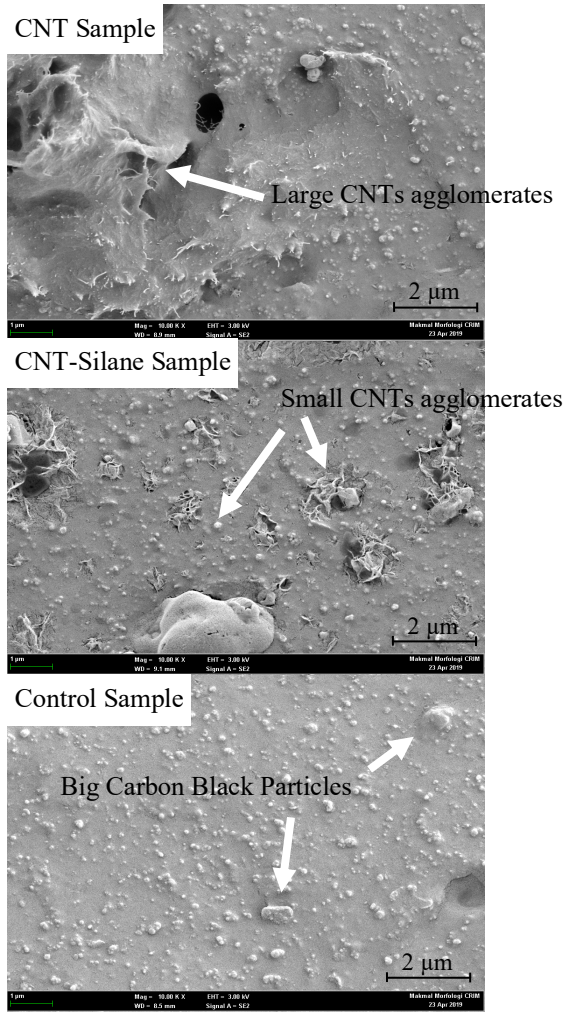


Figure 5: High magnification FESEM micrographs of the surface of tensile fracture samples

Cure Characteristics

Rheological data (refer Table 3) explains the cure characteristics of the as-cast samples, in terms of scorch time (TS₂), cure time (TC₉₀) and maximum torque (MH). The CNT sample experienced a shorter TS₂ as compared to the control sample. However, with the substitution of CNT fillers with CNT-silane fillers, the TS₂ of CNT-Silane sample was extended to 3 min 17 seconds, though 5 seconds shorter than the control sample. It is understood

that during the scorch delay period, the majority of the accelerators' chemical reactions took place [9].

Table 3: Rheological data displayed according to ASTM D6204 terminology

Sample	Time (min: second)		Torque (N.m)			Cure Rate Index (min ⁻¹)
	TS2	TC90	ML	MH	MH – ML	
CNT	3:09	7:35	0.34	1.11	0.77	17.45
CNT-Silane	3:17	7:53	0.32	1.04	0.72	17.93
Control	3:22	7:53	0.32	1.03	0.72	19:26

TC90 is the time required to reach 90% of a complete cure, and this is normally the state of cure at which most of their physical properties reach the optimum levels [9]. Similar to the TS2 data, the CNT sample has a lower TC90 than the control sample. It is believed that the addition of CNTs had increased the thermal conductivity of CNT sample, and improved heat transmission in the blended compounds. The previous study claimed that the improved thermal conductivity due to CNT addition results in an increase in the rate of vulcanization [3]. However, we also believed that the presence of CNT agglomerates (as shown by Figure 5) could have increased the CB fillers connectivity in the CR-filled CB+CNT compound. As a result, the combination of both higher heat transmission and fillers connectivity may contribute to the shorter time for the full cure of CNT sample.

Interestingly, TC90 of CNT-Silane sample reached 7 min 53 seconds, on par with the control sample. The microstructural images (as in Figure 5) showed that the CNT-Silane fillers were dispersed more uniformly in CNT-Silane sample than the untreated CNT fillers in the CNT sample. The CNT-Silane dispersion resulted in a greater distance between fillers (CNT-Silane and carbon black particles). Thus, this factor diminished the efficiency of heat transmission through the inter-fillers network and indirectly extended the TS2 and TC90. This explains the TS2 and TC90 of CNT-Silane sample were longer than the CNT sample.

TS2 and TC90 data were used to calculate the cure rate index (see Equation 1), in which the latter represents the vulcanization rate of the vulcanizates.

$$Cure\ rate\ index\ (CRI) = 100/(TC90-TS2) \tag{1}$$

CRI of the three samples (refer Table 3) arranged from the highest to the lowest as follow: Control, CNT-Silane and CNT samples. The finding shows that CNT-Silane addition improved the vulcanization rate of CR-filled

CB+CNT by ~3%. However, more study is needed to improve the CRI, as it is still 8% lower than the CRI of the control sample.

It is also shown that Si-69 acted as lubricant, causing a decrease of the minimum (ML) and maximum torque (MH) values of the CNT-Silane sample. Its ML and MH were comparatively lower than the CNT sample and on par with the values of the control sample. ML is a measure of the stiffness of the unvulcanised sample taken at the lowest point of the cure curve [9]. Whereas, MH represents the stiffness of the fully vulcanized sample at vulcanization temperature [10]. Hence, the findings suggest the substitution of as-received CNT with the CNT-Silane increase the processability of CR-filled CB+CNT compound.

It is believed longer TS2 and TC90, as well as lower ML and MH of CR-filled CB, added with CNT-Silane enabled a better dispersion of the secondary fillers (CNTs) during the calendaring process of CR-filled CB+CNT. Again, the cure characteristics findings could explain the good CNT-Silane fillers dispersion as observed in the tensile fracture sample (as shown by Figure 5).

Conclusion

Substitution of as-received CNT with the CNT-silane as the secondary fillers improved the tensile strength and elastic modulus of cured of the CR-filled CB samples by 4%. The substitution to CNT-silane increased both mechanical characteristics of the CR-filled CB from 22.5 MPa and 17.6 MPa to 23.0 MPa and 18.1 MPa respectively. The usage of CNT-Silane also increased the cure rate index (CRI) of the CR vulcanizates from 17.45 to 17.93 min⁻¹. CNT-Silane also improved the compound processability, where there were decreases of minimum (ML) and maximum torque (MH) values from 0.34 and 1.11 N.m in as-received CNT samples to 0.32 and 1.04 N.m respectively in CNT-silane samples. Future work study needs to investigate the effect of direct mixing of Si-69 or other types of silane coupling agent into the CR-filled CB+CNT compound. The study could cut-down the number of compound processing steps to increase the feasibility of the rubber nano composite compounding process for industry application.

Acknowledgement

The authors wish to thank Sunrich Integrated (SRIT) for providing raw materials, sample preparation and characterization facilities. Special thanks also to Tony Chew (SRIT) for useful discussions. This manuscript is an extended version of manuscript presented in MERD'19.

References

- [1] R. Dahiya, "E-Skin: From Humanoids to Humans," *Proceedings of the IEEE* 107 (2), 247-252 (2019).
- [2] B. P. Kavgate and C. Das, "Electronic Applications of Chloroprene Rubber and Its Composites," in *Flexible and Stretchable Electronic Composites*, D. Ponnamma, K. K. Sadasivuni, C. Wan, S. Thomas and M. A.-A. AlMa'adeed, Cham, (Springer, Switzerland), 279-304 (2016).
- [3] A. Krainoi, Y. Nakaramontri, S. Wisunthorn, S. Pichaiyut, C. Nakason, C. Kummerlöwe, N. Vennemann and S. Kiatkamjornwong, "Influence of carbon nanotube and ionic liquid on properties of natural rubber nanocomposites," *Express Polymer Letters* 13 (4), 327-348 (2019).
- [4] M. Balasubramanian and P. Jawahar, "Rubber—CNT Nanocomposites," in *Advances in Nanostructured Composites: Volume 1: Carbon Nanotube and Graphene Composites*, M. Aliofkhazraei, (CRC Press, Boca Raton), 295-314 (2019).
- [5] H. H. Le, S. Wießner, A. Das, D. Fischer, M. auf der Landwehr, Q. K. Do, K. W. Stöckelhuber, G. Heinrich and H. J. Radsch, "Selective wetting of carbon nanotubes in rubber compounds – Effect of the ionic liquid as dispersing and coupling agent," *European Polymer Journal* 75, 13-24 (2016).
- [6] P. Sae-Oui, C. Sirisinha, K. Hatthapanit and U. Thepsuwan, "Comparison of reinforcing efficiency between Si-69 and Si-264 in an efficient vulcanization system," *Polymer Testing* 24 (4), 439-446 (2005).
- [7] M. Bhattacharya, "Polymer nanocomposites—a comparison between carbon nanotubes, graphene, and clay as nanofillers," *Materials* 9 (4), 262 (2016).
- [8] Y. Poonpipat, K. Leelachai, R. A. Pearson and P. Dittanet, "Fracture behavior of silica nanoparticles reinforced rubber/epoxy composite," *Journal of Reinforced Plastics and Composites* 36 (16), 1156-1167 (2017).
- [9] J. A. Razak, N. Mohamad, H. E. A. Maulod, K. T. Lau, R. F. Munawar, M. E. A. Manaf, S. Ismail and M. A. Mahamood, "Characterization On Thermal And Mechanical Properties Of Non-Covalent Polyethyleneimine Wrapped On Graphene Nanoplatelets Within Nr/Epdm Rubber Blend Nanocomposites," *Journal of Advanced Manufacturing Technology* 11 (1(1)), 85-100 (2017).
- [10] Standard Test Method for Rubber Property—Vulcanization Using Oscillating Disk Cure Meter, ASTM D2084 – 11 (2016).